OPTIMAL TRAJECTORIES AND ORBIT DESIGN FOR SEPARATED SPACECRAFT INTERFEROMETRY

by

(Edmund) Mun Choong Kong

B.E., Mechanical and Space Engineering (Hons)
University of Queensland, 1995

SUBMITTED TO THE DEPARTMENT OF AERONAUTICS AND ASTRONAUTICS ENGINEERING IN PARTIAL FULFILLMENT OF THE DEGREE OF

MASTER OF SCIENCE

at the

MASSACHUSETTS INSTITUTE OF TECHNOLOGY

February 1999

Signature of Author ....
Department of Aeronautics and Astronautics
November 05, 1998

Certified by ....
David W. Miller
Assistant Professor
Thesis Supervisor

Accepted by ....
Jaime Peraire
Associate Professor
Chairman, Department Graduate Committee

Optimal Trajectories and Orbit Design for Separated Spacecraft Interferometry

by

(Edmund) Mun C. KONG

Submitted to the Department of Aeronautics and Astronautics
on November 05, 1998 in Partial Fulfillment of the
Requirements for the Degree of Master of Science
at the Massachusetts Institute of Technology

ABSTRACT

Imaging of inter-stellar objects at angular resolutions that are beyond the capability of single aperture systems is made possible with the advent of the interferometer. Since the angular resolution of an interferometer is inversely proportional to the separation of its apertures, angularly fine objects can only be detected using a separated spacecraft interferometer (SSI). In order to maximize the return from such a system, this study addresses the optimal trajectories for a SSI operating both outside and within a gravity-well. In the case of imaging from outside the gravity-well, the sequence of physical locations, where measurements are made to best mimic the point spread function of an equivalent filled aperture system, is determined by optimizing an image quality metric, known as the Mean Square Error. Then, the minimum effort trajectory for maneuvering these apertures to these locations is found. While sub-optimal, since the optimization problem is broken into two independent parts, it is shown that substantial efficiencies are realized over other proposed methods. Furthermore, the military and intelligence community is seriously considering the use of a SSI for Earth imaging purposes. Since the size of the apertures contribute towards the total mass of the system, the minimum aperture size required for a Fizeau interferometer which allows instantaneous imaging of a terrestrial target is determined. The orbits in which these spacecraft should be placed, to minimize the propellant required to maintain their positions in the cluster, are then determined. In particular, an innovative orbit design is presented which employs all four conic sections to meet the interferometric requirements while minimizing propellant expenditure.

Thesis Supervisor:
Prof. David W. Miller
Dept. of Aeronautics and Astronautics

ACKNOWLEDGMENTS

At last, two years and two months! That is how long it took me to obtain my S.M. degree from this place. I must say that this would not be possible if not for the support that I have received from the different individuals and this is as good as any other place that I shall begin to acknowledge them.

The first person on the list is no other than my thesis supervisor, Prof. David Miller. Dave has been instrumental in this research in that he has spent a LOT of time critically reviewing this piece of work. He is definitely one of the smartest person that I have met and his ability provide just the right advice and guidance is definitely second to none. But what intrigue me most about Dave is the genuine interest that he has in his students. There may be other more well known professors, but Dave, it is an honor and thank you for giving me the opportunity to learn from you.

If this thesis should have a second advisor, there is no doubt in my mind that this person should be Dr. Raymond Sedwick. At times when I needed quick advice in the early hours of the morning (3 am), there's no question as to who I can depend on. I just cannot thank Ray enough for the numerous hours that we have spent discussing the different issues that arose from this work. Ray, thank you for giving me so much of your time to either discuss problems or proof read this thesis.

I like to thank the new "Dr." Graeme B. Shaw, who should be credited as the "Father of Distributed Satellite Systems", for his never ending technical support and friendship. His ability to understand and rationalize the most abstract concepts and then explain them in the way that only he can, has never ever failed to amaze me. Dr. G Barrington Shaw, you are no doubt the best at what you do.

If ever I needed a big brother, I do not think I would have chosen anyone else other than Cyrus Jilla. His friendship especially in helping me to settle in when I "first got off the boat" is what I will cherish most from knowing him. His advice and words of encouragements have definitely made it easier for me to face my first year at MIT. Cyrus, thank you for your friendship.

The other part of the S.M. degree involves taking classes at MIT. I have to admit that without Gregory "The Lab King" Mallory for helping me with some of the problem sets, things could have turned out quite differently. Greg's understanding of how things fit together has never stopped to amaze me. Greg, thank you for your patience in entertaining the different questions that I have, ranging from research topics to problem sets and of course, the qualifiers.

In conjunction with this thesis, I must also thank Dr. Alan Levine of MIT's Center for Space Research for taking his time to read Chapter 2 to ensure that our understanding of interferometry is indeed correct.

I would also like to thank SharonLeah Brown who is our fiscal officer, Homero Gutierrez for his generosity in Hawaii, and everyone in the laboratory for your friendship and making my stay at MIT so much more enjoyable.

Of course, I cannot forget to thank Amanda Cheng, my girlfriend for being there for me when I needed her most. Amanda, thank you for tolerating with the long hours that I have been putting into my work and more importantly, your love.

I like to thank my parents for giving me the opportunity to be who I am today. I would also like to thank my sister, Munyee, for coming here all the way from Brisbane to keep me company, especially in the last few days of this thesis being written. Mum, dad and sis, thank you for your never ending love and support - I love you all too.

BIOGRAPHICAL NOTES

Edmund Mun Choong Kong was born on October 14th, 1973, to Yoke Thiam Kong and Choon Keun Ng in Kuala Lumpur, Malaysia. His father, a mechanical engineer, is currently the Technical Director of YTL Industries in Malaysia and his mother, a manager with Westpac Banking Corporation in Australia. Edmund attended both primary and secondary schools in Malaysia. His formal education in Malaysia ended when he left his secondary school, Seri Garing Secondary School, to attend Ipswich Grammar School in Australia at the age of 16. In 1991, he graduated as one of the top 1% students in the state of Queensland upon entering the University of Queensland for his tertiary education. There, he received honors as the top student in the Department of Mechanical Engineering and was also named in the inaugural Dean's list in 1995. In that same year, he graduated from the university with Bachelors of Engineering in Mechanical and Space Engineering with Honors Class 1. In conjunction with his degree, he was also awarded a University Medal for his outstanding academic achievements. In September 1996, he joined Massachusetts Institute of Technology under the supervision of Prof. David W. Miller. During his two years with the Space Systems Laboratory, he has published a number of papers based on the work presented in this study. In fact, his work in the development of innovative techniques for u-v plane coverage in support of space-based interferometry won him the 1998 Allan Barrett Prize for excellence in Astrophysics at MIT. He is currently a student member of the American Institute of Aeronautics and Astronautics (AIAA). Following the completion of his S.M. degree from MIT in November of 1998, Edmund will continue his studies in pursuit of his Ph.D. degree at MIT.

Publications:

Kong, E. M., and Miller, D. W., *Optimization of Separated Spacecraft Interferometer Trajectories in the Absence of A Gravity-Well*, SPIE's International Symposium on Astronomical Telescopes and Instrumentations, Paper no. 3350-13, March 1998.

Sedwick, R. J., Kong, E. M. C., and Miller, D. W., *Exploiting Orbital Dynamics and Micropropulsion for Aperture Synthesis using Distributed Satellite Systems: Applications to Techsat21*, AIAA Defense & Civil Space Programs Conference, AIAA-98-5289, October 1998.

TABLE OF CONTENTS

Abstract . . . 3

Acknowledgments . . . 5

Biographical notes . . . 6

Table of Contents . . . 7

List of Figures . . . 11

List of Tables . . . 15

Chapter 1. Introduction . . . 17
- 1.1 Motivation . . . 17
- 1.2 Overview of Interferometry . . . 20
- 1.3 Study Objectives . . . 22
- 1.4 Approach and Outline . . . 23

Chapter 2. Imaging Configurations . . . 25
- 2.1 Proposed Imaging Configurations . . . 27
  - 2.1.1 Golay Arrays . . . 28
  - 2.1.2 Cornwell Points . . . 29
  - 2.1.3 Proposed DS3 Configuration . . . 30
- 2.2 Optimized MSE . . . 31
  - 2.2.1 Image Quality . . . 32
  - 2.2.2 Simulation Grid . . . 36
- 2.3 Optimization Strategy . . . 37
- 2.4 Radio Interferometry . . . 39
  - 2.4.1 Nominal Result (101x101 Pixels) . . . 40
  - 2.4.2 Comparison with other Imaging Configurations . . . 44
  - 2.4.3 Reducing MSE over a Square Partition of the PSF . . . 46
  - 2.4.4 Reducing MSE over a Rectangular Partition of the PSF . . . 49
- 2.5 Visible Interferometry . . . 52
  - 2.5.1 Optimized MSE (High Resolution Mode) . . . 53
  - 2.5.2 Comparison with Other Imaging Configurations . . . 56
- 2.6 Fizeau Interferometer (Snap-Shot Mode) . . . 58
  - 2.6.1 Calculating u-v Coverage for Simple Systems . . . 61
  - 2.6.2 The Fill Factor (FF) Metric . . . 63
  - 2.6.3 Minimum Aperture Size - Single Frequency Results . . . 64

2.6.4 Aperture Size - Visible Spectrum 67
2.7 Summary 70

Chapter 3. Imaging Outside of a Gravity-Well 73
3.1 Trajectory Optimization - 'Stop and Stare' 74
3.1.1 Mass Metric 75
3.1.2 Time Metric 76
3.1.3 Optimization Strategy - Travelling Salesman Algorithm 77
3.1.4 Mission Parameters 78
3.2 Two Collector Interferometer 79
3.2.1 Cornwell Imaging Configurations 81
3.2.2 DS3 Imaging Trajectory 85
3.2.3 Optimized MSE 88
3.2.4 Comparisons 91
3.3 Multiple Collector Interferometer 93
3.3.1 Cornwell Imaging Configuration 94
3.4 Other Considerations 97
3.5 Summary 99

Chapter 4. Earth Imaging from within Earth's Gravity- Well 101
4.1 Hill's Equations and ΔV Derivation 102
4.2 Orbit Perturbations 105
4.2.1 Non-Spherical Effect 105
4.2.2 Third body perturbations 106
4.2.3 Solar Radiation Pressure 107
4.2.4 Atmospheric Drag 107
4.2.5 Comparisons 108
4.3 Circular Trajectories 109
4.3.1 Combiner Spacecraft Maintaining a Fixed Position 109
4.3.2 Zero Zenith-Nadir Motion 110
4.3.3 Change of Line of Sight (LOS) 113
4.4 Paraboloid Orbits 116
4.4.1 Free Elliptical Trajectories 117
4.4.2 Circular Paraboloid 119
4.4.3 Paraboloid Foci - The Hyperbola 125
4.4.4 Change of LOS - Rotating the Configuration 127
4.4.5 Change of LOS - Relocating the Combiner 130
4.5 Case Study: Geosynchronous Orbit 134
4.5.1 Mission Parameters 134
4.5.2 Mass Comparisons 135
4.6 Other Considerations 138
4.7 Summary 143

Chapter 5. Conclusions **147**
5.1 Summary 147
5.1.1 Imaging Configurations 147
5.1.2 Imaging Outside the Gravity-Well 148
5.1.3 Imaging in Earth's Gravity-Well 149
5.2 Conclusion 150
5.3 Future Issues 151
References **153**
Appendix A. Point Spread functions **157**
Appendix B. Optimal Imaging Trajectories **171**

LIST OF FIGURES

1.1 Schematic for a two collector interferometer operating in the visible regime [Jilla, 1998]. . . . 20

2.1 Three-fold symmetry Golay Arrays [Golay, 1971]. . . . 28

2.2 Examples of Cornwell imaging configurations [Cornwell, 1988]. . . . 30

2.3 Proposed DS3 collector spacecraft imaging configuration [Linfield, 1997]. . . . 31

2.4 Two methods of determining the power response of an interferometric system. . . . 33

2.5 Nominal intensity pattern of a point source for an interferometer where science light from more than two apertures can be combined simultaneously. . . . 35

2.6 Illustration of the hexagonal grid used in the optimization. . . . 37

2.7 Simulated annealing flow chart. . . . 39

2.8 Determination of best MSE statistical measure for N = 7 imaging configuration. . . . 41

2.9 Optimized MSE aperture configurations with their corresponding PSF (101x101 pixels) 42

2.10 Decrease in MSE as the number of apertures is increased (101x101 pixels). . . . 42

2.11 Pixel-by-pixel comparison of the Error^2 (101x101 pixels). . . . 43

2.12 Golay imaging locations and their corresponding PSF. . . . 44

2.13 Cornwell imaging locations and their corresponding PSF. . . . 45

2.14 Optimized MSE imaging configurations with their corresponding PSF (75x75 pixels). 47

2.15 Decrease in MSE as the number of apertures is increased (75x75 pixels). . . . 47

2.16 Optimized MSE imaging configurations with their corresponding PSF (51x51 pixels). 48

2.17 Decrease in MSE as the number of apertures is increased (51x51 pixels). . . . 49

2.18 Optimized MSE imaging configurations with their corresponding PSF (101x51 pixels). 50

2.19 Decrease in MSE as the number of apertures is increased (101x51 pixels). . . . 50

2.20 MSE comparisons for the four different optimizations. . . . 51

2.21 Nominal intensity pattern of a point source for a two collector and one combiner spacecraft interferometer. . . . 54

2.22 Optimized MSE imaging configurations for a two collector spacecraft interferometer. . 55

2.23 Decreasing MSE as the number of u-v points is increased. . . . 55

2.24 Discretized DS3 imaging locations and its corresponding PSF. . . . 57

2.25 MSE comparison for the different imaging configurations. . . . 58

2.26 The u-v coverage distribution using the Golay-6 imaging configurations. . . . 60

2.27 The u-v coverage for a single and two aperture systems. . . . 62

2.28 Minimum aperture size required to provide full u-v coverage for the Golay arrays. . . . 65

2.29 Fill factor comparison for the two imaging configurations. . . . 67

2.30 Fill factor comparisons between single frequency and multiple frequency imaing configurations. . . . 69

2.31 Single and multiply frequency u-v coverage comparisons. . . . 69

3.1 Three spacecraft interferometer imaging configuration. 78
3.2 Imaging constraint due to combiner-collector-sun angle. 80
3.3 Collector spacecraft thruster firing at 42.5° due to the difference in the propulsive acceleration produced on the spacecraft. 81
3.4 Examples of optimal propellant trajectories for a two collector interferometer using the equivalent Cornwell imaging locations. 82
3.5 Total propellant mass required for the spacecraft to traverse through the equivalent Cornwell imaging locations. 83
3.6 Examples of optimal time trajectories for a two collector interferometer using the equivalent Cornwell imaging locations. 84
3.7 Imaging time per image for a two collector spacecraft interferometer using the equivalent Cornwell imaging locations. 85
3.8 DS3 imaging trajectory proposed in Linfield, 1997. 86
3.9 Optimal mass trajectory using the DS3 imaging locations. 87
3.10 Optimal time trajectory using the DS3 imaging locations. 87
3.11 Examples of minimum propellant trajectories for a two collector interferometer using the optimized MSE imaging locations. 88
3.12 Total propellant mass required for the spacecraft to traverse through the optimized MSE imaging locations. 89
3.13 Examples of minimum time trajectories for a two collector interferometer using the optimized MSE imaging locations. 90
3.14 Imaging time per image for a two collector spacecraft interferometer using the optimized MSE imaging locations. 90
3.15 Propellant required to obtain the corresponding optimized image MSE. 91
3.16 Minimum imaging time required to obtain the corresponding optimized image MSE. 92
3.17 Propellant required for a two collector and one combiner interferometer to image 498 objects over 15 years. 93
3.18 System mass required to image inter stellar objects using the different Cornwell imaging configurations. 96
3.19 Average propellant to spacecraft mass ratio required to image 498 objects using the different Cornwell imaging configurations. 96
3.20 Image quality versus propellant requirement trade-off. 98
4.1 Hill's coordinate frame shown with respect to Earth. 103
4.2 Collector Spacecraft in forced circular trajectory about a combiner spacecraft 109
4.3 Spacecraft rotating about a circle of radius Ro at an angular velocity of ω. 111
4.4 Varying LOS by rotating array through angles ϕ and ψ. 113
4.5 Variation in $\Delta V/n^2R_0T_{life}$ as array LOS1 vector is varied. 116
4.6 Two possible trajectories for a spacecraft to traverse in free orbits. 118
4.7 Illustration of the intersection between an inclined circular paraboloid and the y-z plane. 122
4.8 Intersection between a circular paraboloid and a plane resulting in an ellipse. 124
4.9 $\Delta V/n^2R_0T_{life}$ required for combiner spacecraft as various paraboloids are fitted onto the free orbit ellipse. 126
4.10 Exploitation of conic section properties in free collector orbits 127

4.11 $\Delta V/n^2R_oT_{life}$ required to maintain a collector spacecraft in the rotated free elliptical orbit due to varying the array's LOS. 128

4.12 Elliptical orbit traversed by a collector spacecraft that results in a maximum $\Delta V/n^2R_oT_{life}$ value in Figure 4.11. 129

4.13 Minimum $\Delta V/n^2R_oT_{life}$ required to maintain the combiner s/c position at the optimum foci at the various array LOS1 vector. 130

4.14 Maximum delay line required to combine light from spacecraft in the elliptical orbit and the $\Delta V/n^2R_oT_{life}$ required to maintain the combiner spacecraft for the different imaging configurations 133

4.15 Comparison of total spacecraft propellant required for nadir pointing Earth imager. . 136

4.16 Comparison of total spacecraft propellant required for off-nadir pointing Earth imager. 136

4.17 Relocating the combiner spacecraft for off-nadir imaging. 137

4.18 Difference angles between the incoming light ray and the reflected light ray at the collector and the angles at which the combiner spacecraft see the collector spacecraft. 140

LIST OF TABLES

2.1 Three-fold symmetry Golay arrays [Golay, 1971]. 29

2.2 Performance measure of the Cornwell Points using equation 2.3 30

2.3 Image quality results for a 101 x 101 pixel PSF. 40

2.4 Comparison of the different imaging configurations using the Cornwell and MSE metrics. 46

2.5 Results for Golay and Cornwell configurations for monochromatic imaging. 66

2.6 Results for Golay and Cornwell configurations for broad band imaging. 68

4.1 Comparisons of the various orbit perturbations. 108

4.2 Extrema LOS1 vector orientations as shown in Figure 4.5. 116

4.3 Extrema LOS orientations as shown in Figure 4.11. 129

Chapter 1

INTRODUCTION

1.1 Motivation

The National Aeronautics and Space Administration (NASA) and the scientific community have recently initiated the Origins Program to roadmap future space astronomy and astrophysics for the next 20 years [Naderi, 1998]. The purpose of the Origins Program is to help answer fundamental questions regarding the origins of life and the universe such as:

- How did the first galaxies form?
- How do stars and planetary systems form?
- Are there any planets outside our solar system that are capable of sustaining life?
- How did life originate on Earth?
- Is there life (however primitive or evolved) outside our solar system?

Even though it is not possible to go back in time to determine how the galaxy was formed, one can observe how new interstellar objects are formed through the use of telescopes. Similarly, the existence of life sustaining planets outside this solar system can also be determined by direct observation. In short, the Origins Program attempts to answer the above fundamental questions through the collection of direct observational evidence.

Even before the initiation of the Origins Program, terrestrial telescopes have been used to look at distant astronomical objects. Unfortunately, due to atmospheric disturbances and physical constraints, there exists a limit at which these astronomical objects can be resolved. To overcome the atmospheric disturbances, the Hubble Space Telescope was then developed, and has been in operation in Low Earth Orbit (LEO) since 1990. This telescope, which operates in the visible to infrared regime, can provide resolutions up to ten times better than any ground-based telescope with its

2.4 m reflecting aperture [STScI, 1998]. There is, however, a limitation to the size that these telescopes can be launched as they have to fit within the shroud of a launch vehicle. Currently, the largest fairing diameter that can be supported by a launch vehicle is 4.57 m flown on the Arianne 5 [Isakowitz, 1991].

The physical limitation, however, is overcome through the use of deployable structures. A filled aperture system, such as the Next Generation Space Telescope [Stockman ed., 1997], requires the precision deployment of an eight meter diameter, thin facesheet primary mirror. The Space Interferometer Mission [Yu et al, 1998], on the other hand, requires the precision deployment of much smaller optics in the form of an interferometer. Since the separation of the apertures can be made much larger than the size of the apertures, more distant objects can be detected with comparable angular resolution. The largest array is the Very-Long-Baseline Array (VLBA), which consists of ten apertures spread across the United States [Thompson et al, 1986]. This array, like many others, operates in the radio regime due to the far more developed imaging technology. The ability to sample the radio signals such that they can be correlated at a later time is the main contributor to this technology advancement.

In general, the capability of an interferometer to produce high quality images is dependent upon the locations of the apertures. Terrestrial arrays can be placed in any pattern conceivable, and in this pattern they will remain. Hence, given a certain number of apertures, only interferometric measurements at the baseline separations defined by the locations of the apertures can be obtained. These terrestrial arrays do not allow additional baseline measurements to be taken as the apertures have very limited maneuverability. However, the array rotates on the sky due to Earth's rotation. This provides additional baselines.

Arrays that are placed in space, however, can be maneuvered through the use of propulsion units. Due to the flexibility in changing the aperture separations in free space, there are in fact two separated spacecraft interferometer missions that are being planned in the Origins Program. The two missions are the Terrestrial Planet Finder (TPF) [Beichman et al, 1996], to detect the existence of other planetary systems and the Planet Imager (PI) [JPL, 1998], to directly image these planets. In fact, for the TPF mission, trade studies between using a separated spacecraft interferometer (SSI) and a structurally connected interferometer (SCI) were conducted by Surka et al, 1996 and Stephenson et al, 1998 which resulted in SSI being strongly considered for the mission.

Given that a certain number of different baseline measurements are made using a specified number of apertures, there exists a trade between adding more apertures into the system or using more propellant to maneuver the fewer number of apertures such that measurements at all the required baseline separations are obtained. This trade can be carried out only if the propellant resources required for the limited number of apertures are determined. In order to maximize the returns, one purpose of this study is to determine the optimal imaging trajectories for a separated spacecraft interferometer operating in free space.

Other than imaging astronomical objects, NASA has also exhibited interest in Earth imaging through its Mission to Planet Earth Enterprise. Besides NASA, the military and intelligence community are also interested in terrestrial imaging for security reasons. Rather than using a large monolithic aperture, systems consisting of a number of smaller apertures have been proposed to improve overall systems reliability [Jilla, 1998]. An example of such system is the proposed Air Force Techsat21 program [AFRL, 1998].

Exploring the use of an interferometer to image terrestrial objects is not new. In fact the Air Force Ultralite system [Powers et al, 1997] proposed a six aperture interferometer located on a single spacecraft to obtain high resolution terrestrial images. However, the separation between the apertures within a spacecraft is limited. A higher resolution system created by placing apertures on different spacecraft has since been proposed. Since these spacecraft are located in Earth's orbit, it only makes sense to take advantage of Earth's gravity to move these spacecraft relative to each other and thereby sweep out an image plane. Therefore, the second purpose of this study is to design the orbits in which these spacecraft should be placed to obtain terrestrial images using the least amount of on-board propellant.

As the cost of launching spacecraft into space is dependent upon the mass of the payload, determining the optimal imaging configuration for an interferometer system which minimizes propellant consumption is therefore critical. The first objective of this study is to determine the minimum resources required for an interferometer located outside the gravity-well to image astronomical objects. For an interferometer located in Earth's orbit, different orbit designs are explored for Earth imaging. Hence, the second objective of this study is to determine the optimal combination of orbital parameters and micro-propulsion for a separated spacecraft interferometer operating in Earth orbit.

1.2 Overview of Interferometry

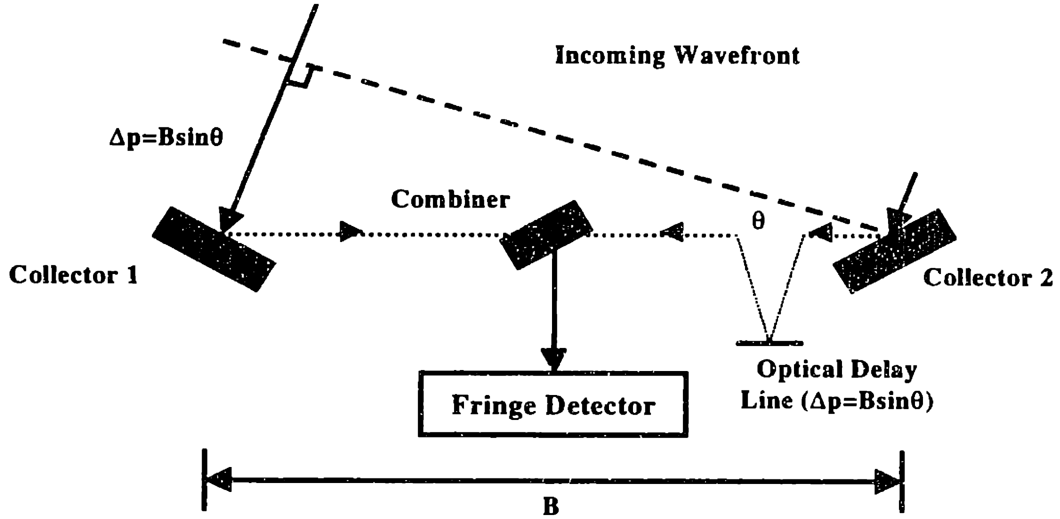

Figure 1.1 Schematic for a two collector interferometer operating in the visible regime [Jilla, 1998].

Due to the improved angular resolution obtainable using an interferometer, many astronomical missions are turning towards the use of multiple aperture systems. The signals received at the interferometer's apertures are combined to provide the angular resolution that is equivalent to that of a single aperture that has a diameter roughly equal to the separation distance between the interferometer's apertures. In this subsection, a brief overview of the two interferometers that are commonly being used to image astronomical objects is presented. These two interferometers are the Michelson and Fizeau interferometers.

The Michelson interferometer is the more commonly used interferometer among the two. Some of the missions that have been proposed to operate in this interferometer mode are the Space Interferometer Mission [Yu et al, 1998]. Irrespective of whether the interferometer is operating in the radio or visible regime, signals collected at the collector apertures must be combined at a single location to provide a single data point. In radio interferometry, signals from the different apertures are normally recorded and correlated at a later time. The output of the correlation is a single complex value, which gives the magnitude and phase of the image's spatial Fourier component associated with the separation between the apertures projected normal to the line-of-sight (LOS) to the target. However, in the visible regime, the science light collected at the apertures must be combined in real time since its phase cannot be recorded. This combined light is then focused onto a single-pixel, photon counting detector to detect its intensity. Shown in Figure 1.1 is the schematic of an interferometer operating in the visible regime. The optical delay line is required to allow the combiner to combine the same wavefront originating from the target and thereby create a coherent fringe.

The interferometric measurement described in the previous paragraph is only for one baseline separation. In Fourier space, this baseline separation is normally known as the u-v point, given by:

$$\begin{aligned} u &= \pm\frac{x_2 - x_1}{\lambda} \\ v &= \pm\frac{y_2 - y_1}{\lambda} \end{aligned} \tag{1.1}$$

where (x_i, y_i) are the coordinates of the i-th aperture. The variables u and v correspond to spatial wave numbers (frequencies) of intensity variations across the image.

In order to obtain good interferometric images, more measurements must be taken at different u-v points to obtain other Fourier terms in the image. This can be done by either moving the collector spacecraft or for ground-based apertures, the u-v coverage of the system can be swept out through the Earth's rotation [Thompson et al, 1986]. Once all the necessary measurements are made, the visibility map, which consists of all the interferometric measurements at the different baseline separations, is inverted to give the brightness image of the source. This inversion is performed by taking the inverse Fourier transform of the visibility map.

The angular extent of an object which an interferometer can resolve from its neighbor is known as the angular resolution. For a Michelson interferometer, the angular resolution is given by:

$$\theta' = \frac{\lambda}{B\cos\theta} \tag{1.2}$$

where $B\cos\theta$ is separation between the apertures the projected normal to the LOS and λ is the target's wavelength of interest, also measured in units of length. Since angular resolution improves with the separation of the apertures, most of the astronomical missions have proposed to adopt the Michelson interferometer. In general, the separation between the apertures is much larger than the size of the apertures themselves.

An underlying assumption that is made in using an interferometer that makes sequential baseline measurements is that the states of the target remain constant throughout the imaging process. This is usually a reasonable assumption for imaging astronomical objects. However, in order to image a rapidly changing target, such as a terrestrial target, instantaneous imaging is required. Instantaneous imaging of a target is possible if a Fizeau interferometer is used.

Designed to operate in the visible spectrum, the Fizeau interferometer is essentially like a conventional telescope where small segments of apertures make up parts of a virtual primary mirror such that they have u-v coverage that is equivalent to that of a filled aperture. As in the Michelson interferometer, the science light path lengths from the target to the combiner through the collector apertures must remain the same. However, the combined light is brought to focus onto a multichannel detector to obtain the image [JPL, 1998]. The Fizeau interferometer is used for wide field astrometry as it offers a very much wider field-of-view than a Michelson interferometer [Loiseau et al, 1996]. For Earth imaging purposes, this interferometer can be designed to give full instantaneous u-v coverage. In general, the separation between the apertures is comparable to the size of the apertures.

1.3 Study Objectives

The primary objective of this study is to determine the optimal amount of resources required for a separated spacecraft interferometer to successfully carry out a synthetic imaging mission. This objective can be achieved by determining the optimal spacecraft imaging trajectories, where the sequence of maneuvers or orbital parameters which allow a given number of apertures to sequentially move to all of the locations defined in the imaging configuration and thereby synthesize an image is determined. However, in order to determine the optimal trajectories, the optimal imaging configurations for these spacecraft must first be determined. In the case of imaging an astronomical object with a Michelson interferometer, the optimal configuration is in fact the optimal imaging locations for the spacecraft. The term ‘imaging locations’ is defined as the ensemble of aperture locations which allow the interferometric measurements to be made in order to synthesize an image. From these imaging locations, the optimal trajectories can then be determined.

In the case where a rapidly changing target is being imaged, the u-v coverage of the system depends upon both the separation and the size of the apertures. In order to obtain the optimal imaging configuration, not only the locations of the spacecraft must be determined, but the size of the apertures must also be determined. Hence, in this case, the optimal imaging configuration includes determining both the aperture locations as well as the individual aperture dimensions. Since such a system can be used for Earth imaging, the optimal imaging trajectories for this system will then be in terms of the orbits in which the spacecraft should be placed.

Hence, there are two primary objectives of this study. The first objective is to determine the optimal imaging configurations for an interferometer. These results serve as the input to achieve the second objective, where the optimal trajectories of the spacecraft are determined. In summary, the primary objectives of this study are:

- to determine the optimal imaging locations for a separated spacecraft interferometer operating outside the gravity-well for imaging of astronomical objects,
- to use these optimal locations to determine the optimal imaging trajectories for the spacecraft such that the returns from the limited resources are maximized,
- to determine the imaging configurations for a separated spacecraft interferometer designed for Earth imaging,
- to design the orbits at which the spacecraft should be placed and calculate the propellant expenditure to allow images of terrestrial targets to be taken.

1.4 Approach and Outline

From the list of the primary objectives, this study can be broken down into three major sections, the determination of the optimal imaging configurations, the optimal trajectories for an interferometer operating outside a gravity-well and finally the orbits and propulsion needs for an Earth imaging interferometer. Each of these major sections are treated separately and presented in the three major chapters in this study.

In Chapter 2, the optimal imaging configurations for an interferometer operating either in the radio or visible regime are determined. Even though there exist imaging configurations that were optimized based upon their u-v coverages, these configurations do not necessarily give the best interferometer response. A metric based upon the point source response of a Michelson interferometer is determined. This metric, known as the Mean Square Error (MSE), is a measure of how well the interferometer mimics a nominal point spread function (PSF). Using this metric, the optimal aperture locations for a radio interferometer, such as that proposed for the Techsat21 program, are determined. Similarly in the visible regime, the optimal imaging locations for a Deep Space 3 (DS3) like mission are determined.

The determination of the optimal imaging locations for a Michelson interferometer assumes that the object remains unchanged throughout the imaging sequence. In the case where the target is changing rapidly, an assumption usually made for terrestrial targets, images can be obtained using a Fizeau interferometer. Such an interferometer, however, requires full instantaneous u-v coverage which can only be obtained by considering both the aperture locations and their size. Rather than determining the aperture locations for such an interferometer, two configurations that are optimized for instantaneous u-v coverage are used to determine the optimum aperture size that can provide full instantaneous u-v coverage. This optimum aperture size is determined based on the total collecting area of the interferometer and the extent of its u-v coverage. Since the u-v coverage of the interferometer is also dependent upon the operating central frequency and bandwidth, the optimum aperture size is also determined for an interferometer operating over the entire visible regime.

Using the optimal imaging locations for the two collector and one combiner spacecraft determined in Chapter 2, the optimal trajectories for these spacecraft operating outside a gravity-well are determined in Chapter 3. These imaging trajectories are obtained based upon the two metrics that are presented. The first metric is the mass metric, specifically, the propellant required to maneuver these spacecraft through their imaging locations. The second metric is the time required to maneuver through these imaging locations. In the second optimization, it is assumed that the propellant mass required to maneuver the spacecraft is very small compared to the mass of the spacecraft. The chapter is concluded by comparing the different configurations using both the image quality metric and the trajectory metrics.

Since the optimal imaging trajectories for an interferometer outside the gravity-well are determined in Chapter 3, the orbits for an interferometer operating within the gravity-well are determined in Chapter 4. Primarily, three different orbit designs are presented, of which one is an innovative use of the four basic conic sections to allow the system to image a terrestrial target. Comparison of the different designs for an Earth imager operating in a geosynchronous orbit is presented to conclude the chapter. Even though these orbits are developed for an Earth imager operating in the visible wavelength, the results can easily be adapted to image inter-stellar objects or extended to Earth surveillance in the radio regime.

Finally, the key results obtained in the three different chapters are summarized in Chapter 5. The issues that arise as a result of this study are also presented in this chapter. In the end, the objective is to present the different ways in which a separated spacecraft interferometer can be most efficiently utilized.

Chapter 2

IMAGING CONFIGURATIONS

Designing an efficient methodology for synthesizing an image from a sequence of coherent measurements acquired by a sparse aperture array requires a careful balance between quality of the image acquired and the effort consumed to achieve this quality. This work strikes this balance by dividing the design into two steps. First, the sequence of physical locations to which the apertures must be maneuvered (imaging locations) to make these measurements is found by optimizing an image quality metric (Chapter 2). Then, the minimum effort trajectory for maneuvering these apertures to these locations is found (Chapter 3). While sub-optimal, since the optimization problem is broken into two independent parts, it is shown that substantial efficiencies are realized over other proposed methods.

Due to the advantage of using interferometers in astronomy, a number of authors have proposed optimal instantaneous u-v coverage imaging configurations for stationary interferometer arrays [Cornwell, 1988, Golay, 1971]. This is extremely useful for Earth based arrays, as most apertures are either stationary or have very limited maneuvering space. This limitation, however, does not apply to a separated spacecraft interferometer (SSI), as the objective of designing such a system is to allow better u-v coverage by relocating the collector spacecraft to take interferometric measurements at various aperture baselines.

Previous work in determining the optimal imaging configurations is based upon the u-v coverage of the interferometer. The underlying assumption made by these authors is that the response of the interferometer is related by its u-v coverage. No doubt this is true. The method developed in this study determines the optimal aperture locations for the interferometer by looking at its point response directly, and thus eliminating the need to look at its u-v coverage. Though computationally intensive, this method takes full advantage of the superior computing power which has only became available in the last few years.

Imaging in the radio regime allows recorded time domain data from the different apertures to be correlated at a later time. As an example, the recorded data from the different telescopes that form the Very Long Baseline Array (VLBA), are simultaneously correlated at the Haystack Observatory in Massachusetts. In the visible regime, however, light rays from the different collector apertures must be interfered in real-time since it is not possible to digitize these signals and thereby retain their phase information. This, together with the interferometric requirement that the same wavefront from the target must be interfered, requires that a combiner spacecraft must be included in the interferometer design and placed at the equal optical pathlength location.

In a Michelson interferometer, the separation between the apertures is much larger than the dimensions of the apertures themselves. In what is known as the interferometer's u-v coverage, the coverage of the Michelson interferometer is dominated only by the separation of the apertures. Because of this, the optimal imaging configurations for a Michelson interferometer are found by determining the optimal imaging locations. The Michelson interferometer operating in the visible regime is very much like its radio counter-part, with the additional constraint that light rays from the different collectors must be interfered in real-time.

There exists, however, another type of visible interferometer where rapidly changing targets, such as terrestrial targets, are allowed to be imaged. Such an interferometer is known as the Fizeau interferometer. The Fizeau interferometer, however, requires full instantaneous u-v coverage to be provided before images of terrestrial targets can be obtained. This full instantaneous coverage can only be provided if both the baselines between apertures and the size of the apertures contribute towards the interferometer's u-v coverage. As such, the optimal imaging configurations for a Fizeau interferometer are found by determining both the imaging locations and the size of the apertures. Fortunately, the optimal imaging locations for instantaneous imaging have been determined [Golay, 1971, Cornwell, 1988]. Hence, using these imaging locations, the determination of the optimal imaging configurations for a Fizeau interferometer is then reduced to just finding the smallest aperture that can provide the required full instantaneous u-v coverage.

Therefore, the method for finding the optimal imaging configurations for a SSI is slightly different depending on whether it is operating as a Michelson (Section 2.2) or a Fizeau (Section 2.6) interferometer. In Section 2.2, the notion of the Point Spread Function (PSF) and the metric by which the optimal aperture locations are determined for a SSI operating as a Michelson interferometer are developed. The results for the Michelson interferometer operating in the radio regime are presented in Section 2.4. To demonstrate the capability of applying the technique developed in this study to the Air Force Techsat21 program, the mission parameters for this particular program are used. Following this, the results for a visible interferometer are presented and compared to the results with other designs. NASA's Deep Space 3 (DS3) design parameters are used. The DS3 mission is a two collector and one combiner spacecraft interferometer proposed in NASA's New Millennium Program [Blackwood et al, 1998]. The optimal aperture sizes for a separated spacecraft Earth imager operating as a Fizeau interferometer are determined in Section 2.6. However, to begin this chapter, several imaging configurations that have already been proposed are presented to provide a basis for comparison.

2.1 Proposed Imaging Configurations

Imaging of astronomical objects using an interferometer requires that the separation between the apertures be known exactly. This separation, normalized by the electromagnetic wavelength of interest, is known as a u-v point. Since it is generally believed that a good u-v coverage (a set of u-v points) will allow one to obtain good interferometric images, previous work in determining the optimal aperture imaging locations has been focused toward maximizing the interferometer's u-v coverage. The relationships between the absolute positions of the apertures and their corresponding components in the u-v domain are given by:

$$\begin{aligned} u &= \pm\frac{x_2 - x_1}{\lambda} \\ v &= \pm\frac{y_2 - y_1}{\lambda} \end{aligned} \tag{2.1}$$

where (x_i, y_i) are the coordinates of the i-th aperture and λ is the wavelength of interest [Thompson et al, 1986]. In the optical regime, the u-v coverage is also known as the auto-correlation function of the interferometer [Golay, 1971].

In this section, the imaging configurations that have been proposed are presented. The metrics that were used to arrive at these published results are also presented to give the reader an insight as to how these results are determined.

2.1.1 Golay Arrays

An optimal imaging configuration designed for small stationary arrays was first proposed by Golay [Golay, 1971]. These arrays are all non-redundant and optimized for compactness in the arrays' auto-correlation function.

The imaging configurations that are of interest are the threefold symmetry arrays that were presented in Golay, 1971. These imaging configurations, with their respective auto-correlation functions are shown in Figure 2.1. Golay defined a hexagonal grid in which the apertures can be placed. The apertures are then rotated by 120^o and 240^o to give the threefold symmetry imaging configuration. For each of the imaging configurations, the most compact auto-correlation function (u-v points) array is determined. This is done by first assigning a maximum core number, N_c, defined as the number of points within a circle completely filled with auto-correlation points and passing through the unoccupied points of the field closest to the center. The circles in which these points lie are shown in Figure 2.1.

The metric that determines the most compact imaging configuration is given by the core factor number, defined as:

$$C = \frac{N_c}{N(N-1)} \tag{2.2}$$

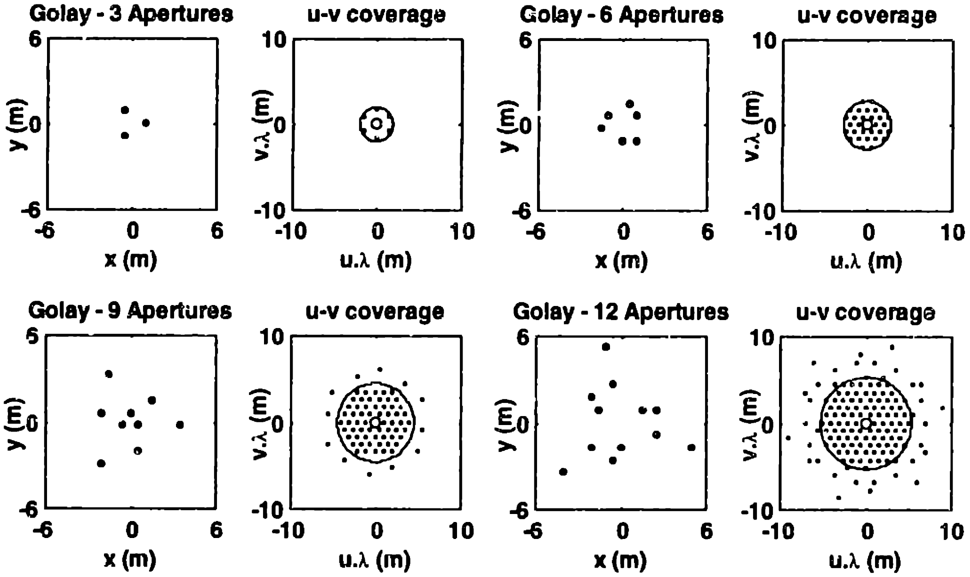

Figure 2.1 Three-fold symmetry Golay Arrays [Golay, 1971].

TABLE 2.1 Three-fold symmetry Golay arrays [Golay, 1971].

No. of apertures (N)	Core Number (N_c)	Core factor (C)
3	6	1.00
6	30	1.00
9	60	0.83
12	96	0.73

where N is the number of apertures in the array. The closer the core factor is to unity, the more compact is the imaging configuration. The core numbers and the core factor numbers for different numbers of imaging locations (N) are presented in Table 2.1.

The advantage of having compact arrays is that apertures of the smallest size can be used to obtain full u-v coverage when the array is used in a snap-shot or Fizeau interferometric mode. This application will be further discussed in Section 2.6. The Golay-6 imaging configuration has been proposed by the US Air Force Research Laboratory for its UltraLite program [Powers et al, 1997].

2.1.2 Cornwell Points

The Cornwell points were originally developed for instantaneous snap-shot imaging of a target in the radio regime [Cornwell, 1988]. The imaging locations were determined based on the separation of the imaging points in the Fourier plane (u-v points). Imaging configurations with evenly distributed u-v points were preferred and were chosen by maximizing the uniformity of the u-v point distribution given by:

$$m(r_1, r_2, \ldots, r_N) = \sum_{i,j,k,l} \log(|u_{i,j} - u_{k,l}|) \tag{2.3}$$

where N is the number of points in the physical domain (x-y plane), $u_{i,j}$ is the separation vector between the points i and j in the physical domain and the self-terms in the summation are ignored. Rather than taking the square of the distances in the Fourier plane, the logarithm of the distance is taken so that points that are farther apart are weighted less heavily. Examples of the Cornwell imaging configurations are shown in Figure 2.2, while their performance measures are listed in Table 2.2.

Note that the Cornwell points were all constrained to lie on a circle in the physical plane (x-y plane) as the imaging elements were found to migrate to the boundary of the optimization space.

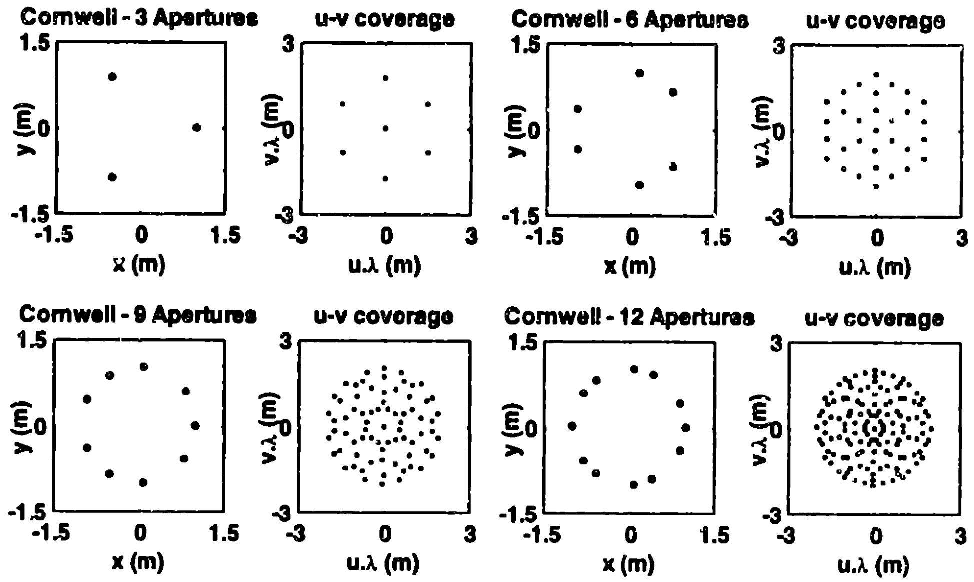

Figure 2.2 Examples of Cornwell imaging configurations [Cornwell, 1988].

TABLE 2.2 Performance measure of the Cornwell Points using equation 2.3

Number of Apertures (*N*)	Performance measure (*m*)
3	26.8
6	127
9	301
12	544

Hence in his optimization, Cornwell only considered imaging elements that were placed on the circle to reduce the time required to carry out the optimization. Incidentally, the pathlengths between all these imaging elements and a combiner element located at the center are the same, which is advantageous for imaging in the visible regime.

2.1.3 Proposed DS3 Configuration

Recently, NASA announced a new program called the New Millennium Program. The objective of this program is to demonstrate advanced technology, in a mission setting, for reducing cost and risk. The third mission in the series, called Deep Space 3 (DS3), is a three spacecraft interferometer system. The currently proposed imaging configuration for the two collector and one combiner spacecraft interferometer is given in Linfield, 1997. Two types of imaging modes were considered for these three spacecraft: the 'Stop and Stare' mode; and the 'Observe on the Fly' mode. The dif-

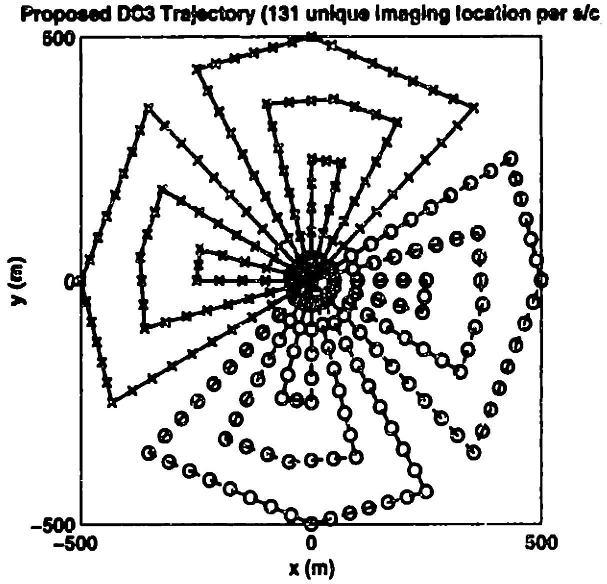

Figure 2.3 Proposed DS3 collector spacecraft imaging configuration [Linfield, 1997].

ference between these imaging modes has direct impact on both the propellant requirement and imaging time, but not on the quality of the interferometric image obtained. These imaging modes are further discussed in Chapter 3.

The DS3 trajectory proposed in Linfield, 1997 is shown in Figure 2.3. The two different symbols (x and o) in the figure correspond to the imaging locations for the two collector spacecraft. The lines joining these locations are the trajectories of the two collector spacecraft. Since equal science light pathlength from the target to the combiner spacecraft via the collector spacecraft must be preserved, the two collector spacecraft must then travel in opposing directions from the origin of the imaging plane. By counting the symbols in Figure 2.3, the total number of unique x-y imaging locations for each collector spacecraft is found to be 131. This corresponds to 261 unique u-v points.

2.2 Optimized MSE

Except for the DS3 imaging configuration, the configurations in the previous section were mainly optimized for snap-shot imaging based upon their u-v coverages. These u-v coverages, however, give little indication as to what the response of the interferometer. Hence, in this study, rather than optimizing in terms of u-v coverage, the optimal aperture locations are found based upon the response of the interferometer. The metric by which these locations are determined is presented in this section.

2.2.1 Image Quality

In order to determine the optimal aperture locations for a Michelson interferometer, one possible solution is to look at the point source response of the interferometer. Ideally, the point source response of the interferometer should approach that of an ideal filled aperture. When a point source is imaged, this ideal filled aperture should produce an intensity map with a single intensity peak, indicating the point source, and zero intensity level elsewhere. However, due to diffraction, the central peak is spread and a number of low intensity rings are observed in the intensity map, hence the term point spread function (PSF). When this intensity map is produced from a circular aperture, it is known as the Airy disk [Hecht, 1987]. The point source response of a uniformly illuminated circular aperture, obtained by applying Huygen's superposition integral [Staelin et al, 1994], is given by:

$$D' = \left[\left(\frac{\pi(1+\cos\theta)D}{\lambda}\right)\left(\frac{J_1\left(\frac{\pi D\sin\theta}{\lambda}\right)}{\frac{\pi D\sin\theta}{\lambda}}\right)\right]^2 \tag{2.4}$$

where D' is the response of the antenna, θ corresponds to the angle from the bore-sight of the antenna, D is the diameter of the aperture, $J_l(.)$ is the Bessel Function of the first kind and λ is the wavelength of the science light.

In the case of an interferometer, with each aperture having the same antenna, the directivity of the interferometer is obtained by convolving the directivity of a single aperture with impulse functions corresponding to the aperture positions in the physical domain. In the image domain, which is the inverse Fourier transform of the system, the contribution to the directivity of the interferometer due to the separation of the apertures is known as the array factor. The array factor of the interferometer is given by:

$$AF(\psi_i, \psi_j) = \left|\sum_{n=1}^{N} \exp\left(-\frac{2\pi i}{\lambda}(\psi_i x_n + \psi_j y_n)\right)\right| \tag{2.5}$$

where ψ_i, ψ_j are the image angular coordinates and x_n, y_n are the coordinates of the n-th aperture in the array. The intensity map of a point source, or the directivity of an N element interferometer, is then obtained by multiplying the directivity of a single aperture with the square of the array factor given in equation 2.5. The intensity map of an interferometer is therefore:

$$I(\psi_i, \psi_j) = \left[\left(\frac{\pi(1+\cos\theta)D}{\lambda}\right)\left(\frac{J_1\left(\frac{\pi D\sin\theta}{\lambda}\right)}{\frac{\pi D\sin\theta}{\lambda}}\right)\left|\sum_{n=1}^{N}\exp\left(-\frac{2\pi i}{\lambda}(\psi_i x_n + \psi_j y_n)\right)\right|\right]^2 \tag{2.6}$$

Rather than squaring the inverse Fourier transform of the antennas in the physical domain to obtain the intensity response of the interferometer, equation 2.6 can also be derived by first taking the auto-correlation of the antennas in the physical domain, and inverse Fourier transforming the resulting auto-correlation function. These two methods for obtaining equation 2.6 are made possible by the fact that convolution in the physical domain is equivalent to multiplication in the Fourier domain, and auto-correlating a system is in effect convolving the system with itself. The two methods of determining the response of an interferometer are shown in Figure 2.4. Starting from the top left box in Figure 2.4, the result of the inverse Fourier transform of the antennas is given by the top right box. Squaring the antenna response then gives the response of the interferometer

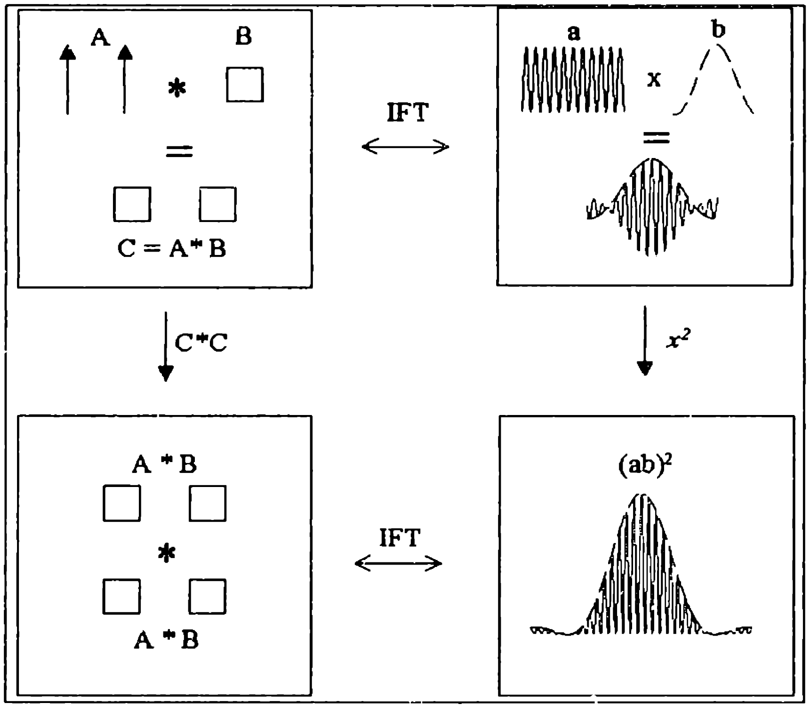

Figure 2.4 Two methods of determining the power response of an interferometric system.

shown in the bottom right box. The path through the bottom left box shows the alternate method to obtain the response of the interferometer.

For observing a source that is located in the far-field, such as observing a distant star, equation 2.6 can be simplified by approximating θ as zero. This approximation can be made since the contributions from the individual apertures to the point source response remain constant for small values of θ. The contribution from the array factor, however, changes rapidly with ψ_i and ψ_j, and therefore cannot be simplified. Hence, equation 2.6 is reduced to the form:

$$I(\psi_i, \psi_j) \approx \left[\left(\frac{2\pi D}{\lambda}\right)\left|\sum_{n=1}^{N} \exp\left(-\frac{2\pi i}{\lambda}(\psi_i x_n + \psi_j y_n)\right)\right|\right]^2 \tag{2.7}$$

For a two-element interferometer, where the apertures are located at x, y and $-x$, $-y$, equation 2.7 reduces to the form shown by equation (3) in Kong et al, 1998 and is given as:

$$I(\psi_i, \psi_j) \approx \left[\left(\frac{2\pi D}{\lambda}\right)\left(2\cos\frac{2\pi}{\lambda}(\psi_i x + \psi_j y)\right)\right]^2 \tag{2.8}$$

However, when it is not possible to approximate θ as zero, the relationship between θ, ψ_x and ψ_y is given by:

$$\theta = \sqrt{\psi_x^2 + \psi_y^2} \tag{2.9}$$

Equation 2.6 gives the intensity map of the target as seen by the N apertures at one instant in time. In order to obtain a high resolution intensity map of the sky, the images of the apertures obtained at different instants in time and at different sets of aperture baselines are added together. Therefore, the built-up intensity map is given by:

$$I'(\psi_i, \psi_j) = \left(\frac{2\pi D}{\lambda}\right)^2 \sum_{k=1}^{M}\left[\left|\sum_{n=1}^{N} \exp\left(-\frac{2\pi i}{\lambda}(\psi_i x_{nk} + \psi_j y_{nk})\right)\right|\right]^2 \tag{2.10}$$

where x_{nk} and y_{nk} are the n-th aperture coordinates at the k-th measurement and M is the total number of observation sets (i.e., the number of imaging locations divided by the number of apertures which equals the number of array re-configurations). In order to make the appropriate comparison between interferometers with different numbers of apertures and different sets of baselines, the

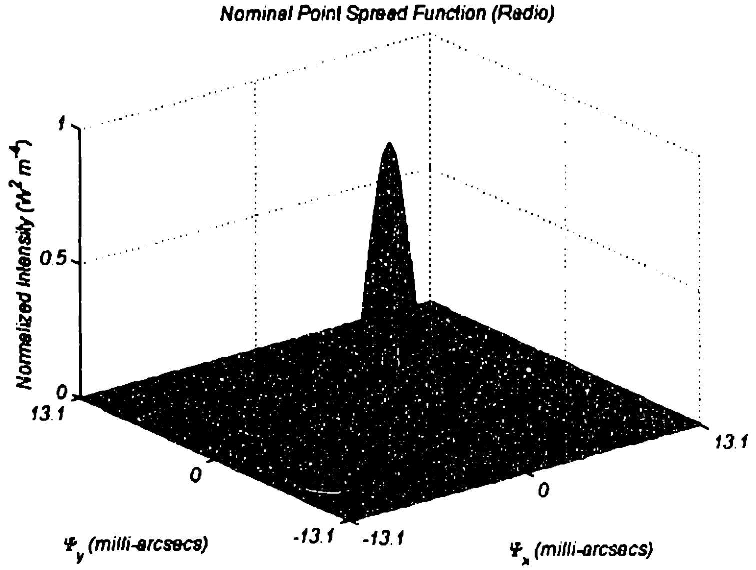

Figure 2.5 Nominal intensity pattern of a point source for an interferometer where science light from more than two apertures can be combined simultaneously.

intensity measure in equation 2.10 is normalized by N^2, where the square is due to the power measurement of the array factor, and M. The normalized intensity is therefore:

$$\overline{I}_N(\psi_i, \psi_j) = \frac{I'(\psi_i, \psi_j)}{MN^2} \tag{2.11}$$

The metric to compare the different intensity maps is given in terms of the Mean-Square-Error (MSE) of the maps relative to the nominal intensity shown in Figure 2.5. The nominal PSF shown in Figure 2.5 is specifically for interferometers operating in the radio regime, where data from all apertures can be simultaneously combined. The MSE of a particular map is given by:

$$MSE = \frac{\sum_{i=1}^{m} \sum_{j=1}^{m} (\overline{I}_N(\psi_i, \psi_j) - \overline{I}_o(\psi_i, \psi_j))^2}{m^2} \tag{2.12}$$

where $\overline{I}_o$ is the nominal intensity map and m^2 is the total number of pixels in the image.

In the following discussion, both the instantaneous (equation 2.6) and the high resolution intensity (equation 2.10) responses of a Michelson interferometer are optimized. In order to determine the optimal aperture locations, these responses are compared to some nominal PSFs using the MSE metric given by equation 2.12. However, to determine these aperture locations, a grid containing all the possible aperture locations must first be defined. This simulation grid is discussed in the next subsection.

2.2.2 Simulation Grid

In simulating the performance of an interferometer, the candidate aperture locations are often discretized. This is because the Inverse Fast Fourier Transform (IFFT) algorithms that have been used to obtain interferometric images require measurements to be taken at equally spaced points. Hence, one can define grids which are regularly coordinatized, such as cartesian or polar.

However, the disadvantage in using both these grids is that the grid points generated are not evenly distributed on a circular disk. The reason that these points should be distributed on a circular disk is to ensure that equal angular resolution in any direction can be achieved since the resolution in a particular direction is directly related to the largest baseline separation in that same direction. Even though a circular grid distributes the possible aperture locations in both the angular and radial directions, the separations between neighboring imaging locations near the origin are much smaller than near the boundary of the grid.

Therefore, in this study, a hexagonal grid is chosen as the points are more evenly distributed within a circular imaging area. In the radio regime, the entire hexagonal grid is bounded with a circle of size 100 m, which is about the size of the clusters in the Techsat21 program, and the points are separated by a distance of $a = 2.5$ m. This corresponds to 367 unique x-y imaging locations in the hexagonal grid. In the optical regime, however, the grid is bounded by a 500 m circle with a minimum separation of $a = 20$ such that comparisons with the DS3 imaging configuration can be made. The minimum separation, a, between possible aperture locations in a hexagonal grid is depicted in Figure 2.6.

There exists, however, another grid that needs to be defined, namely the PSF intensity map. To allow comparison between the different intensity maps, the maps produced by the interferometric measurements are usually discretized depending upon the number of baseline measurements that were obtained. For example, the proposed New Millennium interferometric mission, DS3, is likely to produce images of 10 x 10 pixels with minimum baseline separations of 100 m [Linfield, 1997]. However, to compare the images obtained using different numbers of baseline measurements, and to ensure that the PSF against which different array geometries are judged does not

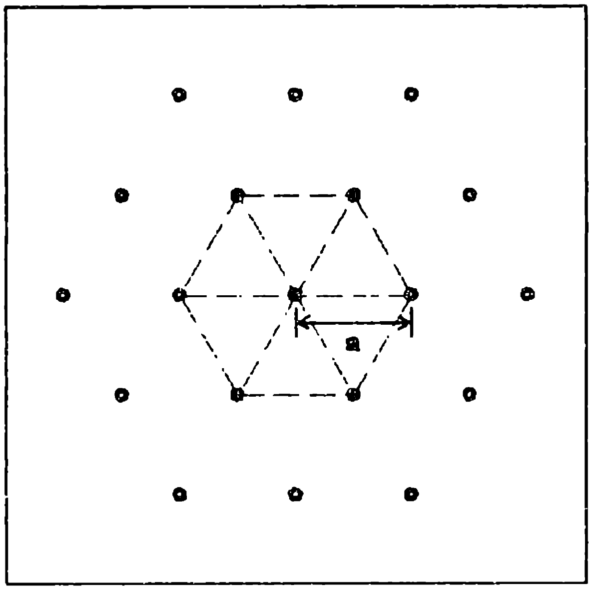

Figure 2.6 Illustration of the hexagonal grid used in the optimization.

introduce discretization errors, the intensity map is discretized to a 101x101 pixel image. Figure 2.5 is in fact plotted on such a grid.

Using either equation 2.6 or 2.10, the intensity maps generated by an N aperture interferometer chosen from the defined grid, can be compared using the MSE metric given in equation 2.12. In order to determine the optimal imaging configurations, one has to consider all the possible configurations. This, however, is not possible due to the large optimization space and one must resort to a heuristic optimization strategy. The optimization strategy used in this study is the subject of discussion in the next section.

2.3 Optimization Strategy

In an optimization problem, the global minimum can only be determined if all the possible solutions are considered, or if the optimization space is proven to be convex. Working in the radio, we see that there are 367 possible locations at which an aperture can be placed. Hence, for a given number of apertures, N, the number of possible combinations to place these apertures is $\frac{367!}{(367-N)!}$, which can be approximated as 367^N. Assuming that it takes approximately 1 ms of computational time to consider each possible configuration, the time required to consider all the possible combinations for $N = 4$ is 210 days! Hence, it is impossible to obtain optimal configurations for an array with four or more apertures.

There exist, however, heuristic optimization methods to obtain the optimal imaging configurations in very short periods of time. The results obtained using these methods, however, are not guaranteed to be the global optimum of the problem. Because of this, the optimization was carried out at least three times for each individual case. More often than not, these heuristic methods gave solutions that are very close to the global optimum in a relatively short period of time. As will be shown later, plots of MSE versus the number of apertures, give rather smooth curves indicating that the random optimization errors are probably small.

In this study, the minimization of the MSE metric in equation 2.12 is found through the use of the simulated annealing optimization technique [Kirkpatrick et al, 1983], which was also used to determine the Cornwell Points [Cornwell, 1988]. The optimization method uses a statistical approach by starting with a randomly selected configuration of aperture locations. A new configuration is then chosen randomly by swapping a point that is already in the set of imaging points with a new point chosen randomly from the total available x-y imaging locations. This configuration is then compared with the current best configuration and is accepted as the new current best configuration if its MSE is the lower of the two. However, the current best configuration can still be replaced by a higher MSE configuration if this configuration has an exp(-MSE/T) value that is greater than a number drawn randomly between 0 and 1. This exponential is in fact similar to the potential energy of an atom given by the Boltzmann law [Feynman et al, 1989]. The variable T is called the "temperature" of the system and is decreased each time a new configuration is accepted. This ensures that for a system that is at a low temperature, the probability of accepting a configuration with a higher MSE is low. The key feature in this optimization technique is that it reduces the chance of the system arriving at a local minimum solution.

The starting temperature chosen in this optimization is T = 10 and is decreased by a factor of g = 0.99 each time a new configuration is accepted. The temperature multiplication factor must be set such that the temperature is reduced in small steps, else a non-optimal or "quenched" solution is obtained instead.

The solution to the optimization is achieved when the system is considered "frozen" and no further changes can occur. This is analogous to the atoms in a material being in a frozen state at extremely low temperature. In this optimization, the temperature of the system is also reduced after a certain number of trials, if no new solution is accepted. The optimization is then stopped after three successive system temperature reductions are made with no new solution accepted. The maximum

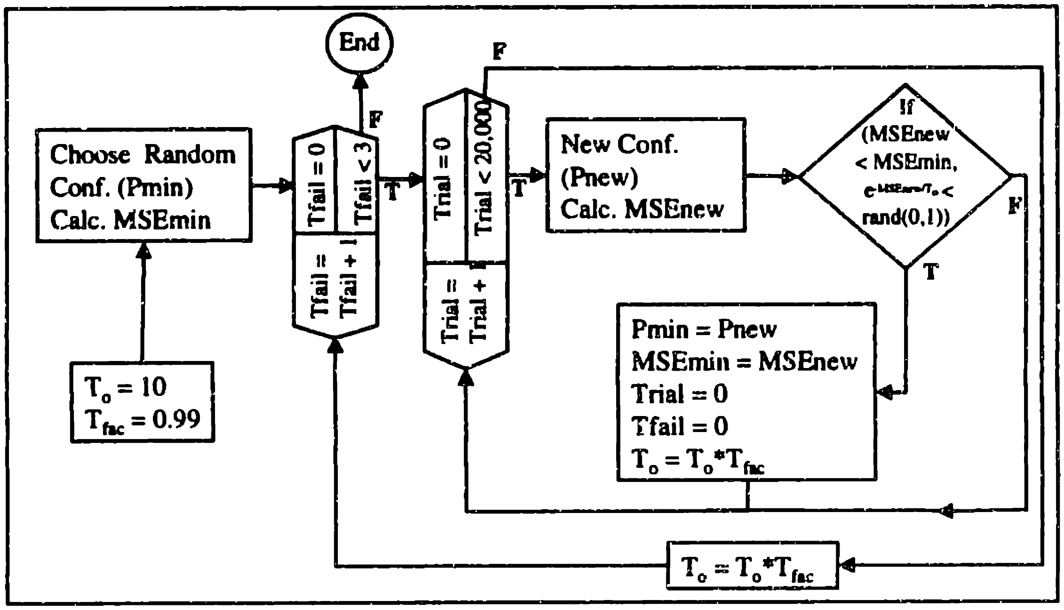

Figure 2.7 Simulated annealing flow chart.

number of trials at each temperature used in this optimization is limited to 20,000 trials. A flow chart out-lining this optimization strategy is shown in Figure 2.7.

In this section, the simulated annealing optimization strategy used in this study to find the optimal aperture locations has been presented. Together with the MSE metric derivation from the previous section, we are now ready to determine these optimal locations. The results for the *N* aperture interferometer operating in the radio regime are given in the next section, while the results for an interferometer operating in the visible regime are given in Section 2.5.

2.4 Radio Interferometry

In this section, the optimal imaging locations for an interferometer operating in the radio regime are presented. To demonstrate the capability of applying the technique developed in this study to a program like the Air Force Techsat21, the mission parameters for this program are used. Therefore, the aperture size is set at 1 m diameter while an operating radio frequency of 4 GHz is used [Shaw, 1998]. The nominal PSF for this analysis, generated by simultaneously combining the signals from all 367 unique imaging locations in the hexagonal grid, is shown in Figure 2.5.

2.4.1 Nominal Result (101x101 Pixels)

In this subsection, the results for the optimal aperture locations optimized over the entire PSF intensity map are presented. The mean, standard deviation and the best MSE performance obtained for various numbers of apertures, as a result of performing the optimization several times, are calculated and presented in Table 2.3. Also shown in Table 2.3 is a statistical measure of the best MSE performance. This statistical measure is a metric by which one can quantify the confidence level that the best MSE configuration is in fact the global minimum. This measure assumes a normal distribution for the MSE obtained for the different optimization runs. Adopting this assumption, the statistical measure of the best MSE obtained is therefore the area under the probability density function. The area under the curve integrated from the best MSE performance obtained to + ∞ can be calculated by:

$$Conf = \frac{1}{\sqrt{2\pi}\sigma}\int_{MSE}^{\infty} \exp\{-(1/2)[(x-\mu)/\sigma]^2\}dx \tag{2.13}$$

where μ is the mean and σ is the standard deviation of the MSEs obtained for the different optimization runs. This statistical measure for $N = 7$ apertures is shown in Figure 2.8.

TABLE 2.3 Image quality results for a 101 x 101 pixel PSF.

No. of Apertures	Mean (W^2 m^{-4}) (x 10^{-3})	Std. Dev. (W^2 m^{-4}) (x 10^{-4})	Best MSE (W^2 m^{-4}) (x 10^{-3})	% Conf. (MSE)
3	98.4	0.00	98.4	96
4	53.3	3.10	53.1	66
5	31.8	1.80	31.7	74
6	20.6	1.95	20.3	92
7	14.3	2.45	14.0	93
8	10.1	1.96	9.84	87
9	7.42	2.31	7.05	95
10	5.46	2.21	5.06	97
11	4.23	1.51	4.09	82
12	3.17	0.91	3.08	86
13	2.59	0.82	2.49	89
14	2.01	051	1.97	78
15	1.61	0.54	1.55	85

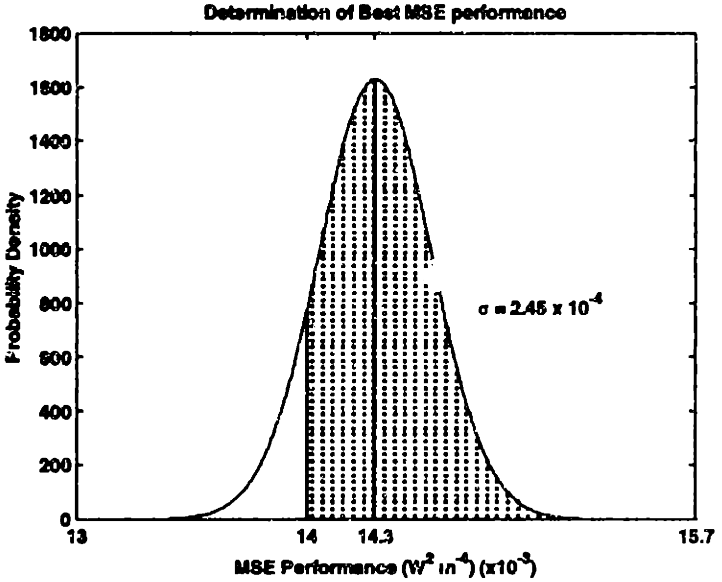

Figure 2.8 Determination of best MSE statistical measure for $N = 7$ imaging configuration.

Examples of aperture locations on the hexagonal grid and their corresponding PSFs are shown in Figure 2.9. For each case, the apertures are shown as black dots superimposed onto the hexagonal grid. Note that it is the relative distance between the apertures that should be considered and not their absolute locations on the grid. This is because the construction of the PSFs of these configurations is dependent upon the baseline combinations that exist between these apertures and not on the absolute position of a fixed geometry array. Since there are more baseline combinations for higher numbers of apertures, the minimum MSE obtained decreases (improves) with the number of apertures. This increase in performance is also evident from the fact that the sidelobes of the system decrease and the mainlobe narrows as more apertures are used in the imaging configuration.

A plot of the best MSE obtained against the number of apertures in the system is shown in Figure 2.10. The MSE in the figure is seen to be inversely proportional with the number of apertures. This suggests that it is more advantageous to increase the number of apertures for low numbers of N compared to configurations that already have high numbers of apertures (diminishing return). A second order inversely proportional curve can be fitted to the data using the least square method and is given by:

$$MSE = 0 - \frac{0.049}{N} + \frac{1.035}{N^2} \tag{2.14}$$

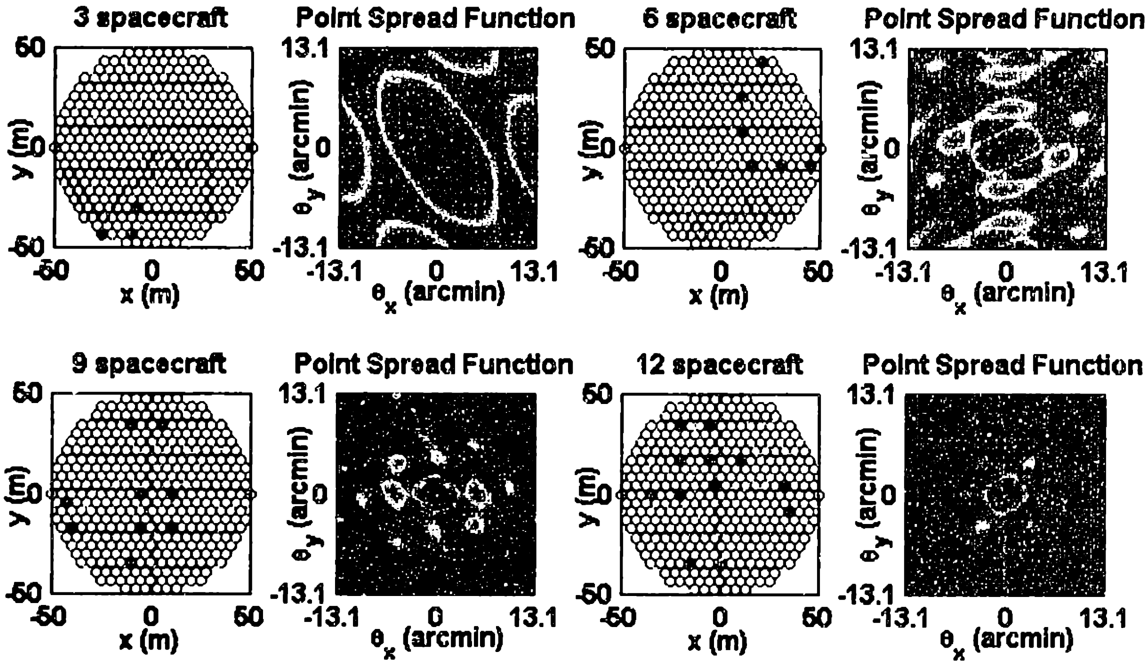

Figure 2.9 Optimized MSE aperture configurations with their corresponding PSF (101x101 pixels).

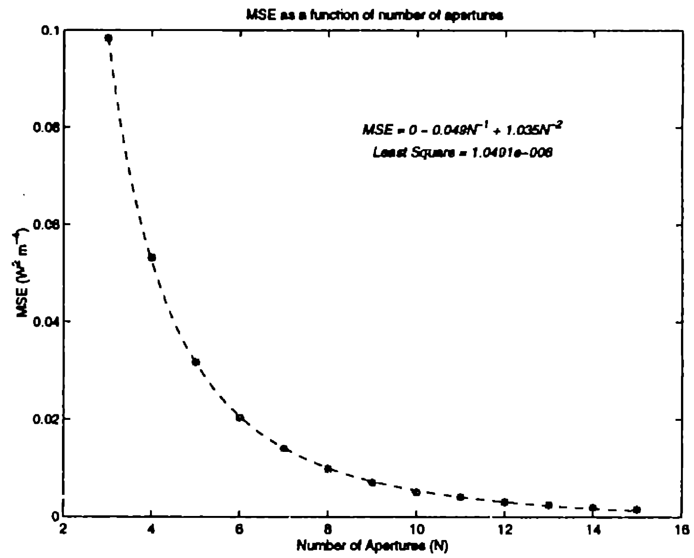

Figure 2.10 Decrease in MSE as the number of apertures is increased (101x101 pixels).

This curve fitting has a least square error of 1.05 x 10^{-6} W^4 m^{-8}.

The MSE metric is in fact a measure of the average square-error over all the pixels in the PSF intensity map. The variation of the pixels that give this MSE value can also be compared. One

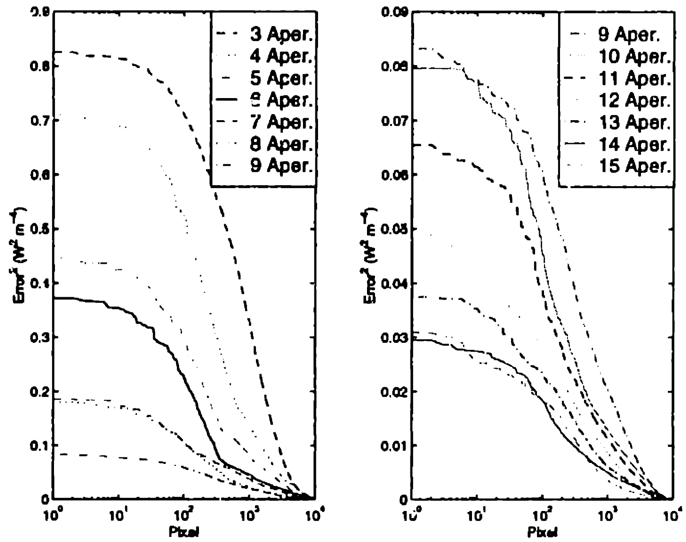

Figure 2.11 Pixel-by-pixel comparison of the Error^2 (101x101 pixels).

method to do this is to plot the pixel square-errors, in descending order, for the different imaging configurations as shown in Figure 2.11. Due to the large difference in the square-error range, the plot is divided into two with the figure on the left showing the comparisons for apertures ranging from $N = 3$ to 9 while the right figure corresponds to $N = 9$ to 15. Notice that in the right figure, there are a number of locations where the curves for different numbers of apertures cross each other. For example, there are approximately 200 pixels in the $N = 15$ apertures that have higher square error when compared with the $N = 14$ apertures. However, there are many more pixels in the $N = 15$ aperture case that have lower square-error. This is the reason why the $N = 15$ configuration has a lower MSE when compared to the $N = 14$ configuration. Using such a plot, one can therefore conclude that a particular N aperture configuration does in fact mimic the nominal PSF better when both its MSE and pixel-by-pixel comparison are lower than another imaging configuration. This is because the MSE measure provides the average while the pixel-by-pixel reveals worst case. However, one can only conclude that a particular imaging configuration has a better PSF on average when only its MSE is lower than another configuration.

It is clear that as the number of apertures is increased in an imaging system, better MSE performance can be obtained. However, the benefits in increasing the number of apertures decreases as more apertures are added to the system.

2.4.2 Comparison with other Imaging Configurations

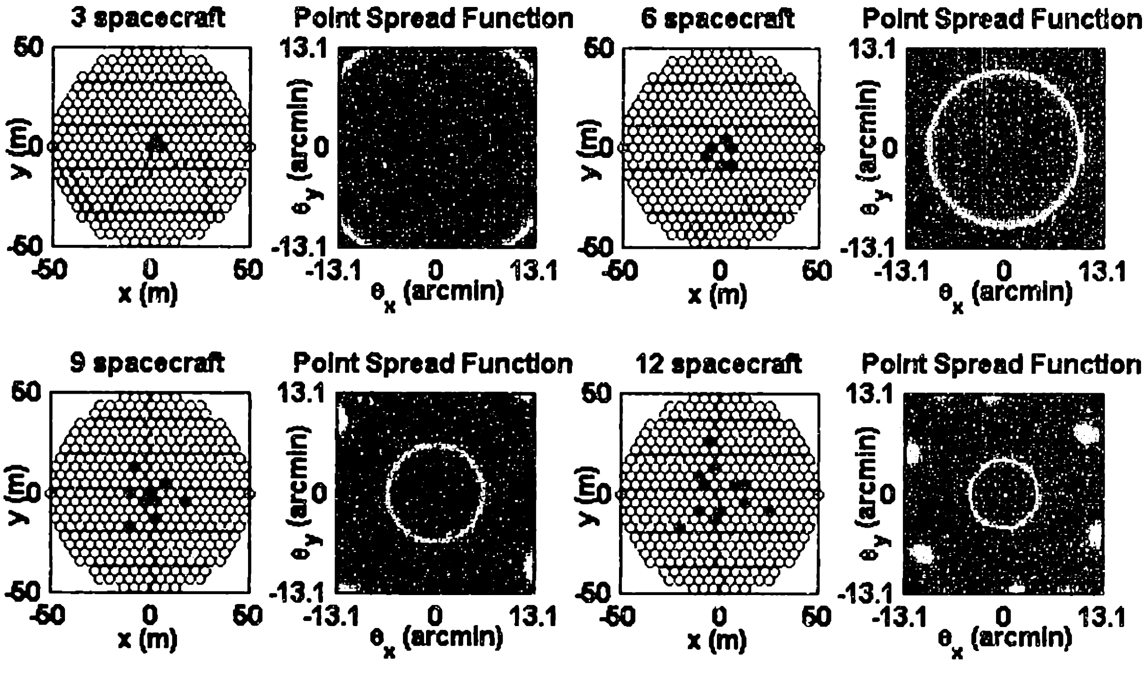

Figure 2.12 Golay imaging locations and their corresponding PSF.

In this subsection, the nominal results obtained using the optimized MSE metric are compared with the configurations that were discussed in Section 2.1. This comparison is made to ensure that the optimized MSE results make sense when other metrics are used instead. Since the results are obtained for a radio interferometer, the optimized MSE configurations are compared with both the Golay and Cornwell imaging configurations.

Examples of the PSFs generated using the Golay imaging locations are shown in Figure 2.12. Since the width of the mainlobe is inversely proportional to the maximum baseline in the configuration, the large mainlobes observed in the PSF maps are due to the compactness of the Golay imaging configurations.

The PSFs generated using the Cornwell imaging configurations are shown in Figure 2.13. Comparing these PSFs with the ones generated using the Golay imaging configurations, tighter mainlobes are observed. There also exist higher and more sidelobes in these PSF images. Hence, even though the Cornwell imaging configurations produce narrower mainlobe PSFs, higher sidelobe levels are also clearly evident.

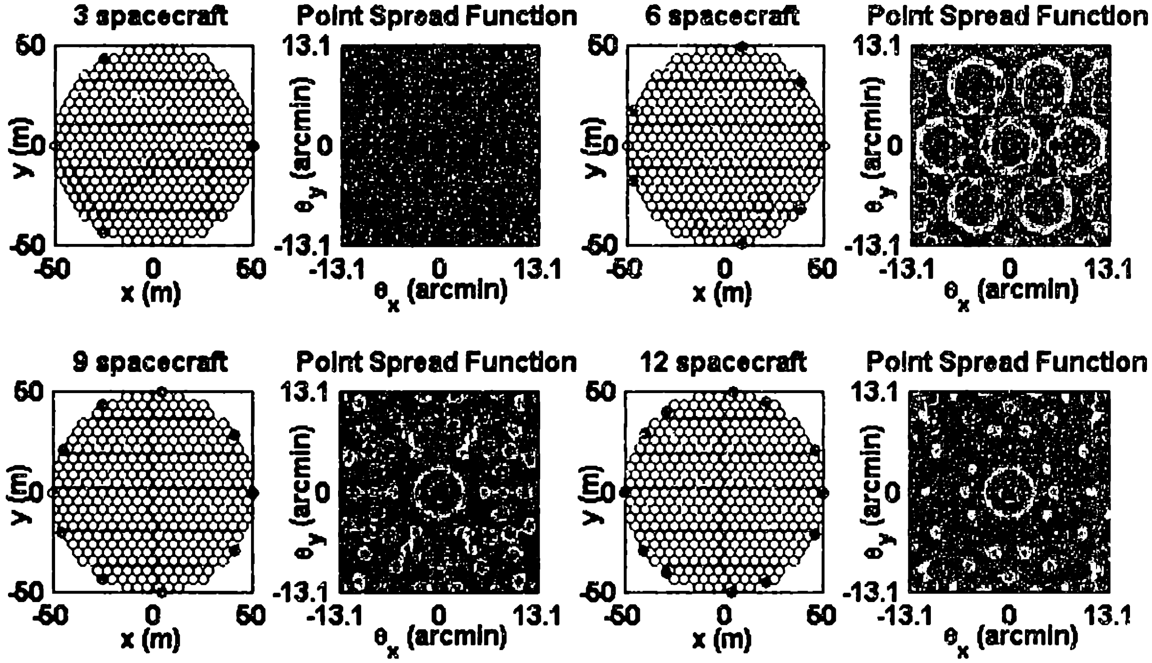

Figure 2.13 Cornwell imaging locations and their corresponding PSF.

These two imaging configurations are compared with the optimized MSE results using both the Cornwell and the PSF MSE metrics. These are tabulated in Table 2.4. Note that lower values of MSE indicate better MSE performance whereas larger Cornwell metric values indicate better performance. The metric used to determine the Golay imaging configurations was not used because the emphasis in the Golay imaging configurations is compactness of the u-v points. However, the u-v points generated using the Cornwell and PSF optimized imaging configurations are not closely packed and hence will not provide any meaningful result using the Golay metric. In Table 2.4, using the Cornwell metric, which favors large u-v values, we see that the optimized MSE aperture locations perform better than the Golay locations. This suggests that the u-v points generated by optimized MSE imaging configurations are more distributed compared to the Golay imaging configurations. This makes sense as the Golay imaging configurations are optimized for compactness of the u-v sampling.

Comparison of the PSF generated by the different imaging configurations indicates that the Cornwell imaging configurations can better mimic the nominal PSF when compared with the Golay imaging locations. This is attributed to the fact that the aperture locations in the Golay configurations are more closely packed compared to the Cornwell imaging configurations.

TABLE 2.4 Comparison of the different imaging configurations using the Cornwell and MSE metrics.

No. of Points	Cornwell Metric			PSF Comparison ($W^2\ m^{-4}$) ($x10^{-3}$)		
	Golay	Cornwell	MSE	Golay	Cornwell	MSE
3	9.66	26.8	16.7	542	172	98.4
4	-	52.1	37.4	-	105	53.1
5	-	86.3	65.4	-	64.8	31.7
6	67.4	127	102	129	44.2	20.3
7	-	178	145	-	34.7	14.0
8	-	235	191	-	27.0	9.84
9	194	301	258	41.4	19.9	7.05
10	-	374	300	-	16.9	5.06
11	-	456	391	-	13.4	4.09
12	396	544	455	19.0	11.1	3.08

Using either of these metrics, as the number of apertures in each of the imaging configurations is increased, better performance is achieved. This is very promising and is a good indication that the optimized MSE technique developed in this study should seriously be considered as an alternative method to determine the optimal aperture locations. Remember that both the Cornwell and Golay imaging configurations were optimized by considering only the distribution of the u-v points over the entire array. There are, however, applications in which the target is known to exist only within a small region of the PSF. In these cases, the optimized MSE technique can be used to determine the optimal aperture locations for mimicking the PSF region in only a portion of its region. This possibility is explored further in the next subsection.

2.4.3 Reducing MSE over a Square Partition of the PSF

Rather than penalizing the MSE over the entire 101x101 pixel PSF, one can penalize the MSE over only a portion of the field-of-view. Certain applications may require that sidelobes be suppressed more in a particular region of the PSF. For example, if the objective is extra-solar planet detection, sidelobes adjacent to the mainlobe can overpower the faint signature of a planet within the habitable region of its parent star. Therefore, it may be desirable to suppress sidelobes adjacent to the mainlobe more than at the outer edges of the PSF. It is important to remember, however, that the total amount of ambiguity in the PSF is fixed. Therefore, requiring a narrow central lobe and low adjacent sidelobes will cause sidelobes near the outer edges of the PSF to rise higher than normal. Running the same optimization procedure, the results for minimizing the MSE over a square 75x75 pixel and 51x51 pixel region centered about the central lobe of the PSF are presented.

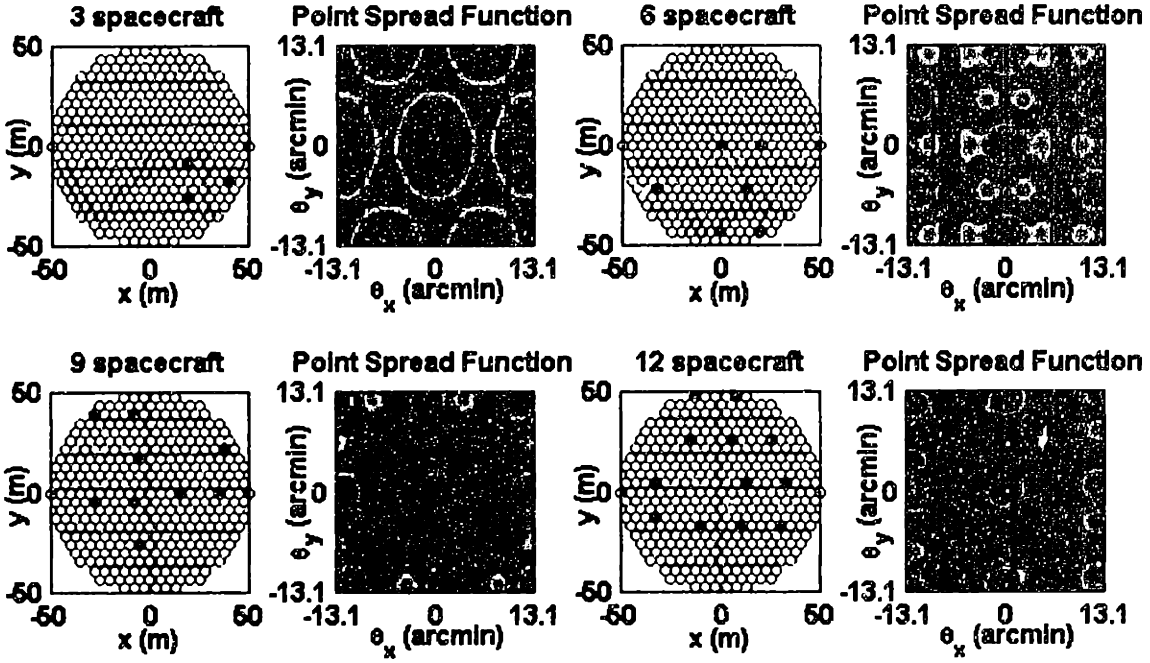

Figure 2.14 Optimized MSE imaging configurations with their corresponding PSF (75x75 pixels).

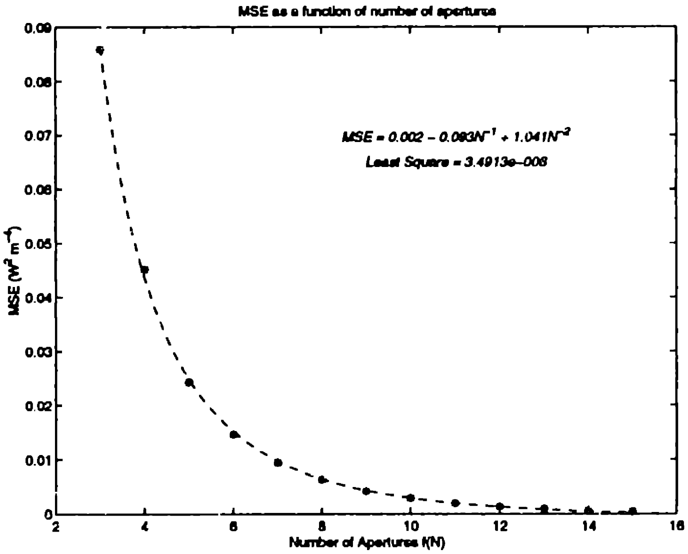

Figure 2.15 Decrease in MSE as the number of apertures is increased (75x75 pixels).

Examples of the aperture locations with their corresponding PSFs, optimized for the 75x75 pixel region, are shown in Figure 2.14. The black square boxes shown in the PSF maps are the regions in which the MSE was penalized. In each of the PSF plots, the amount that the sidelobes within the penalized region are being suppressed becomes more obvious as the number of apertures is increased. However, the sidelobes that exist outside the penalized region are not suppressed and are clearly seen in the plots. Again, the plots for various numbers of apertures are shown in Appendix A.

The relationship between the number of apertures in the interferometer and the corresponding MSE is shown in Figure 2.15. Similar to the results determined for the 101x101 pixel PSF, the MSE produced by these apertures as a function of the number of apertures can be fitted with a second order inversely proportional curve.

Similarly, the PSF plots optimized over a 51x51 pixel region is shown in Figure 2.16. When compared to minimizing the MSE over the entire 101x101 pixel region, optimization over the 51x51 pixel region resulted in higher sidelobes. However, these sidelobes exist outside of the region that is being penalized. The plot of MSE as a function of the number of apertures in the system is shown in Figure 2.17. Again, the decreasing relationship between MSE and the number of apertures is evident from the figure.

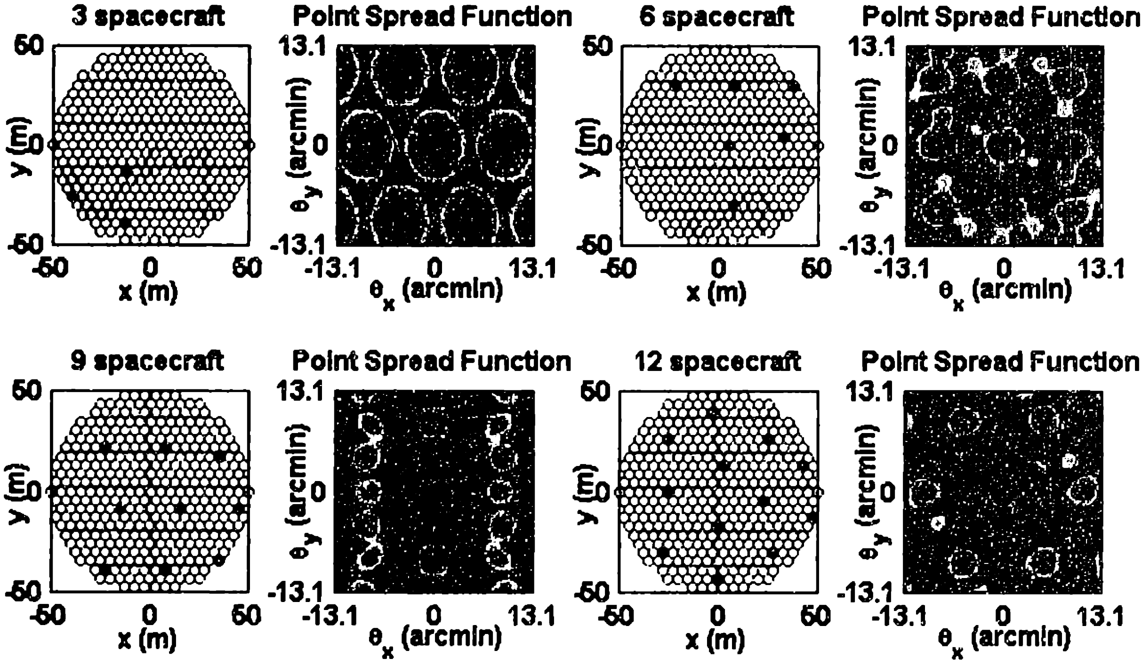

Figure 2.16 Optimized MSE imaging configurations with their corresponding PSF (51x51 pixels).

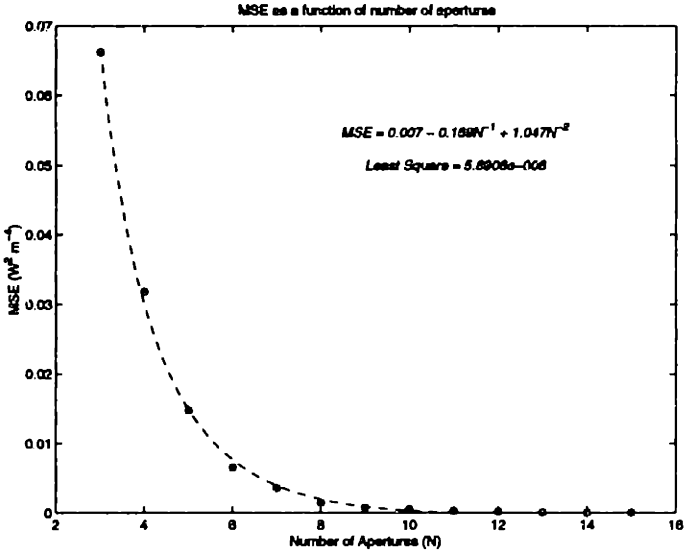

Figure 2.17 Decrease in MSE as the number of apertures is increased (51x51 pixels).

From these results, the optimal aperture locations tailored for suppressing MSE over a reduced PSF map can be determined using the optimized MSE technique developed in this study. There exist, however, applications in which optimization over a differently shaped region of the PSF map is more desirable. In the next subsection, the aperture locations optimized for a rectangular region in the image plane are determined. The results obtained in this subsection and in Section 2.4.1 will be compared with configurations obtained in the next section. Though not considered in this study, non-uniform weightings across the 101x101 pixel grid can also be assigned. In fact, the pixels in the examples shown in this study have a weighting of one when they are penalized in the MSE calculation, and zero when they are not. In some applications, it may be more important to reduce the sidelobes in a particular direction more than in other directions.

2.4.4 Reducing MSE over a Rectangular Partition of the PSF

In this subsection, the capability of the optimized MSE technique to determine the optimal aperture locations for a program such as the Techsat21 space based radar system is demonstrated. A multi-static radar system created by a cluster of spacecraft at an altitude of 800 km will have a 7 km/sec velocity relative to the ground. This will cause the radar returns from ground clutter forward and aft of the cluster to exhibit doppler shifts which could be miss-interpreted as moving targets. Therefore, there is a desire to suppress sidelobes fore and aft of the cluster. In the side-looking direction, this doppler spread is not of concern. Sidelobes in this direction can therefore

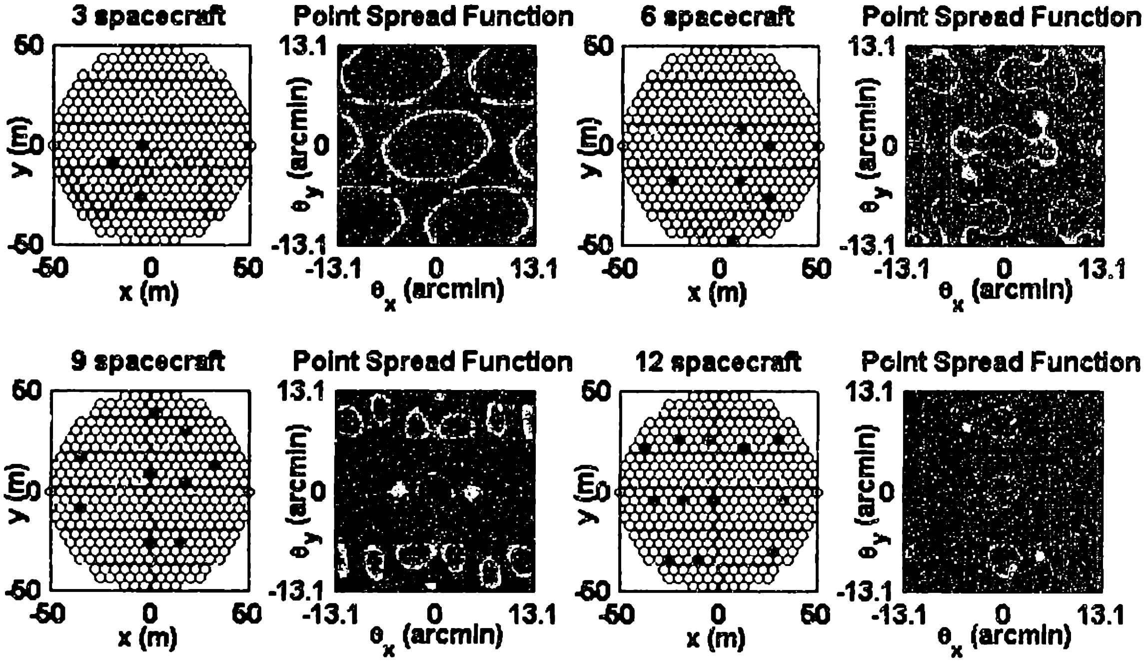

Figure 2.18 Optimized MSE imaging configurations with their corresponding PSF (101x51 pixels).

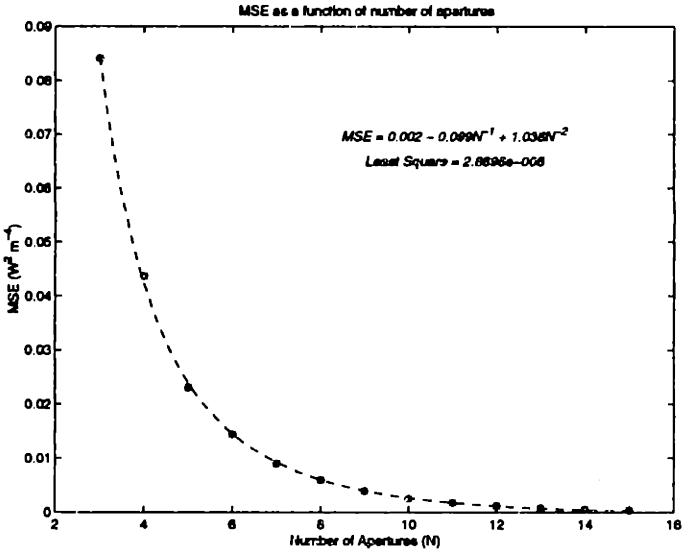

Figure 2.19 Decrease in MSE as the number of apertures is increased (101x51 pixels).

be higher. To avoid false detections from these sidelobes, range-binning is exploited. Hence, it makes more sense to penalize MSE over a rectangular region as opposed to the square regions studied in the previous subsections. In doing so, the emphasis of the optimization is shifted from weighting all the pixels equally to suppressing the sidelobes in one direction more than the other.

Examples of different numbers of apertures and their respective PSFs optimized over a 101x51 rectangular region are shown in Figure 2.18. The region in which the MSE was penalized is bounded by a rectangular box. In all these cases, the sidelobes in the PSF can be clearly seen located beyond the penalized rectangular region. The complete set of PSF images are shown in Appendix A.

A plot of the MSE as a function of the number of apertures is shown in Figure 2.19. As expected, the MSE measure improves with the number of apertures.

A comparison of the MSE as a function of the number of apertures for all the cases studied is shown in Figure 2.20. The figure shows that the 101x51 pixel imaging configuration has a MSE curve approximately the same as the 75x75 pixel configuration. This probably occurs since the number of pixels penalized in the MSE calculation are approximately the same. The figure also suggests that by reducing the number of pixels considered in the optimization, configurations with better MSE performance can be obtained. This suggests that the nominal PSF can best be replicated when smaller regions in the PSF image are used. Unfortunately, reducing the optimization region is equivalent to reducing the field-of-view (FOV) of the interferometer system. For a sys-

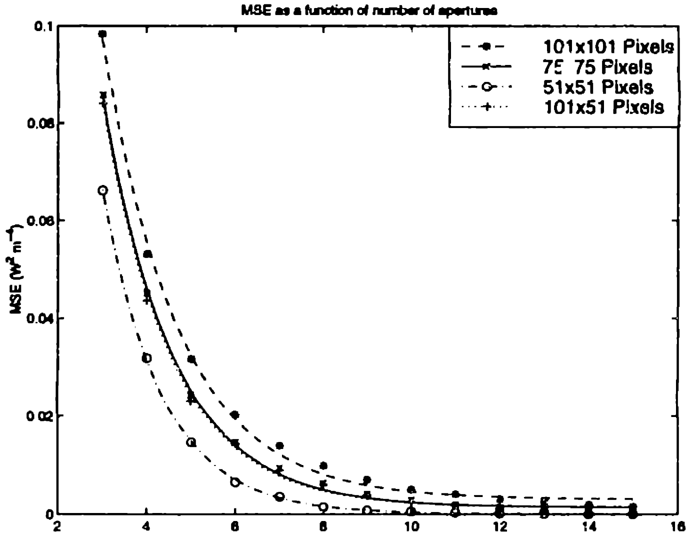

Figure 2.20 MSE comparisons for the four different optimizations.

tem like Techsat21, the reduced FOV will extend the time it takes for the array to scan the entire area of interest.

Hence, in this section, the optimal aperture locations for a Michelson interferometer operating in the radio regime are determined. Comparisons with other imaging configurations show that the optimized MSE technique developed in this study should seriously be considered as a viable alternative to determining the optimal aperture locations. The flexibility with which this technique can accommodate different applications and PSF weightings is also demonstrated.

2.5 Visible Interferometry

As mentioned earlier in the chapter, the difference between imaging in the visible regime as opposed to the radio regime lies in the fact that it is not possible to record the visible science light. Since it cannot be recorded, the science light reflected off the collector apertures must be correlated in real time. This can only be achieved by ensuring that the science light pathlengths from the target to the combiner via the two collector spacecraft are equal. At the combiner, the combined light is focused to a single-pixel, photon counting detector [Blackwood et al, 1998] as it would be for a Michelson interferometer.

In this section, the optimal imaging locations using the MSE metric are determined for a two collector and one combiner interferometer. This two collector interferometer is presumed to operate as an adding interferometer system where interferometric images obtained at each baseline separation are added progressively to produce the final image. To determine how the PSF is affected by the number of interferometric measurements, the number of imaging locations in the optimization is varied. The comparison of these imaging configurations with others is presented in Section 2.5.1.

In this section, the optimal imaging locations for a two collector and one combiner spacecraft interferometer are determined using the optimized MSE technique. Since the interferometric measurements at different baselines are obtained at different times, the final image is obtained by adding images obtained at the different baseline separations. To allow comparison with other imaging configurations the DS3 mission parameters are assumed [Linfield, 1997].

2.5.1 Optimized MSE (High Resolution Mode)

Since the interferometer is assumed to operate as a Michelson interferometer, the u-v coverage of the interferometer is dominated only by the separation of the apertures, as the apertures are very much smaller than their separation. In DS3, the collector mirrors are currently set at 12 cm diameter, while interferometric measurements are made at a minimum separation of 100 m apart [Blackwood et al, 1998]. The frequency chosen in this optimization is 5 x 10^{14} Hz (0.6 micron).

Since the science light must be interfered in real-time, the distance between the combiner and each of the two collectors must be kept the same. This can be accomplished by placing a collector spacecraft at (x,y), and another at (-x,-y), and thus requiring the combiner spacecraft to be placed anywhere along the z-axis (line-of-sight). The three spacecraft located at these points will form the vertices of an isosceles triangle. In DS3, however, the three spacecraft are designed to form the vertices of an equilateral triangle, which is a special case of an isosceles triangle.

The hexagonal grid specified for this optimization is bounded by a 500 m radius circle with a minimum separation of 20 m between the grid points. Since the collector spacecraft are located directly opposite to each other, the number of imaging locations available to choose from is 1157 points. Using equation 2.10, where the array factor expression is replaced with equation 2.8, the nominal PSF for this optimization using these 1157 points is shown in Figure 2.21. However, to reduce the computation time required to determine the optimal imaging locations, the number of locations available to choose from can be further reduced. Since the results obtained here are to be compared with other imaging configurations, namely the DS3 configuration, the optimal imaging locations for the two collector spacecraft interferometer can be found by determining the optimal imaging locations for one of the two collector spacecraft within a quadrant of the imaging plane. This reduction can be made because it has been identified that a collector spacecraft in the DS3 interferometer can only image within a quadrant at a time due to the sun-source angle limitation which will be discussed in Chapter 3. To allow imaging of the source from the other two quadrants, the optimal imaging locations found in one particular quadrant are mirrored onto the others. Hence, the number of imaging locations available to choose from for the collector spacecraft within a quadrant is now 586. This number is slightly more than half the number of points quoted above since all the points that are located on the boundary between the two quadrants are included.

Note that an intensity floor of 0.5 is seen in Figure 2.21 as opposed to zero as seen in Figure 2.5. This is because in the radio regime, both the phase and magnitude of the received signal can be recorded and therefore a multiplying interferometer can be used to interfere the signal. However,

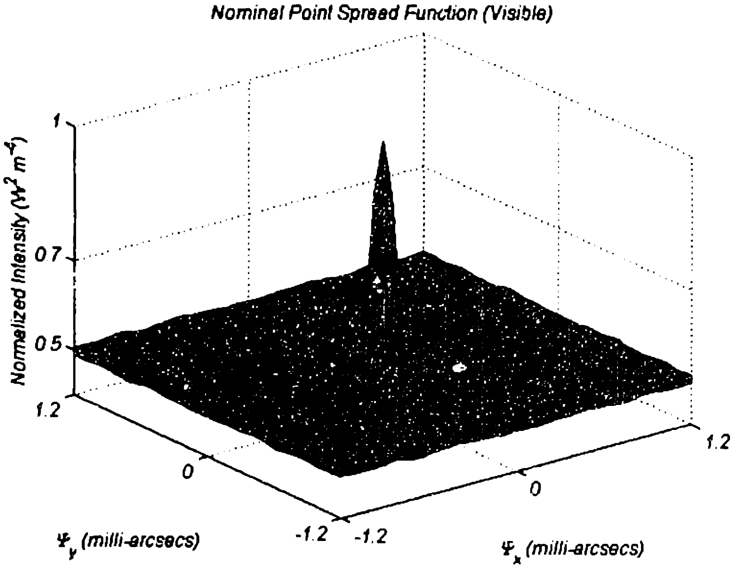

Figure 2.21 Nominal intensity pattern of a point source for a two collector and one combiner spacecraft interferometer.

in the visible regime, an adding interferometer is used as it is not possible to record the waveform of the science light. This 0.5 intensity floor is also seen in Kong et al, 1998.

The image size chosen to compare the different PSF images is 75x75 pixels. This is chosen over the 101x101 pixel grid mainly because of the lack of computer memory available to perform the optimization. However, to demonstrate the capability of the optimization technique, it is sufficient to use only a 75x75 pixel image. Also, rather than penalizing over the entire square image, the MSE is calculated over a circular sub-region. In doing so, the effect of penalizing more along the diagonals of a square region due to the higher number of pixels is reduced. Hence, by penalizing over circular region, there should be no preferential direction in which the imaging locations should be placed. The circular boundary within which the MSE is calculated, is shown in the respective PSF images.

In this optimization, the number of u-v points for a collector spacecraft is varied from 5 to 321. The reason for this wide variation is that these results will be compared with the PSFs generated using the Golay, Cornwell and DS3 imaging configurations. Comparisons between the different imaging configurations can only be made when these imaging configurations have similar numbers of imaging locations or equivalently, the numbers of u-v points. Since the results for the Golay and Cornwell configurations are quoted in terms of the number of apertures, N, the number of unique u-v points for each particular case is then (N (N-1) + 1). Hence, the first 10 optimal

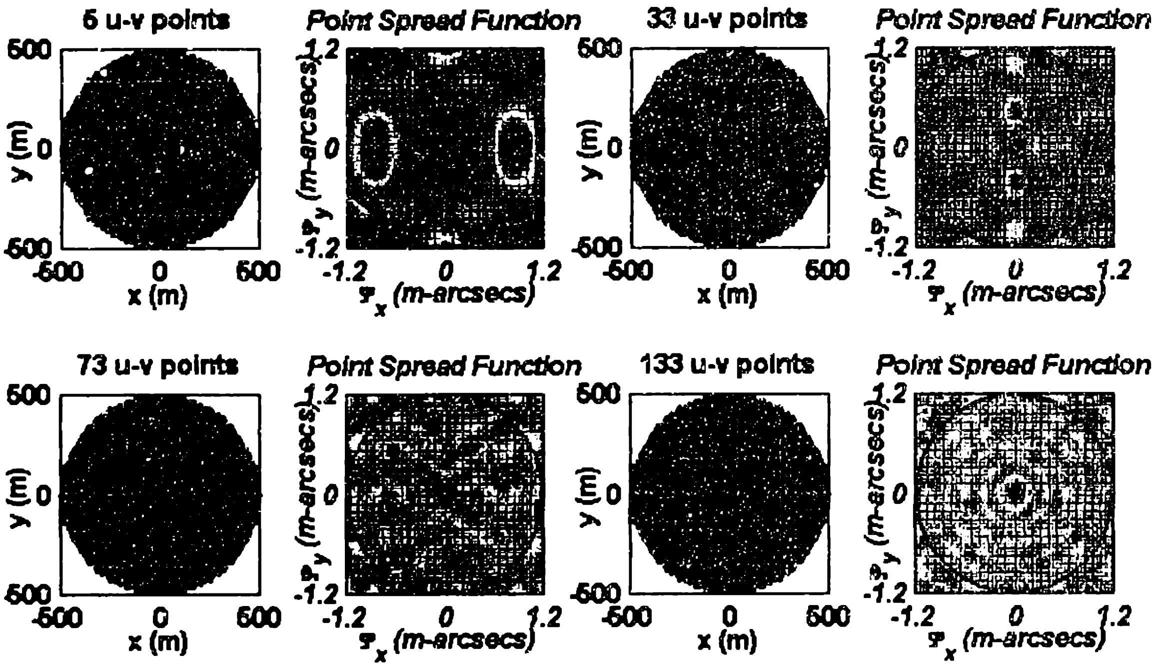

Figure 2.22 Optimized MSE imaging configurations for a two collector spacecraft interferometer.

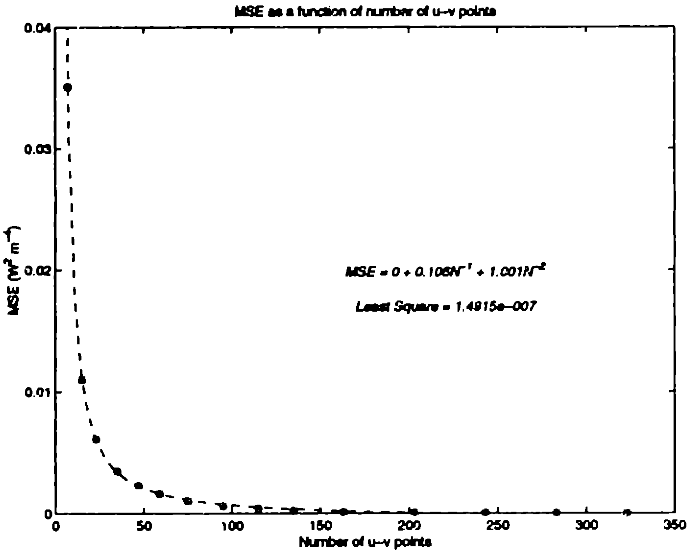

Figure 2.23 Decreasing MSE as the number of u-v points is increased.

imaging configurations determined using the optimized MSE technique correspond to the $N = 3$ to 12 Golay or Cornwell configurations.

Examples of the optimal imaging locations for a two collector spacecraft interferometer and their corresponding PSFs are shown in Figure 2.22. The number of u-v points shown in the figure are comparable to the number of unique u-v points generated by the 3, 6, 9 and 12 aperture Cornwell imaging configurations. Note the higher sidelobes in these PSF images when compared to the PSF generated in a multiplicative interferometer as shown in Figure 2.9. Hence, to produce good interferometric images, more u-v points must be used such that the sidelobes in the PSF images are further reduced. The PSF images for numbers of u-v points that are greater than 133 are shown in Appendix A.

The effect on the MSE as the number of u-v points is increased is shown in Figure 2.23. As was seen in the radio interferometer section, the obtainable MSE decreases as the number of imaging locations is increased.

Similar to the results shown in the radio interferometry section, as the number of imaging locations is increased, the interferometer can better mimic the nominal PSF. The PSFs generated from using these imaging locations are compared with those generated from the imaging configurations that have been discussed earlier.

2.5.2 Comparison with Other Imaging Configurations

In this subsection, the optimized MSE results for the two collector and one combiner spacecraft interferometer are compared with those generated using the Golay, Cornwell and the proposed DS3 imaging configurations. The Golay and Cornwell configurations will be discussed first.

Since the Golay and Cornwell configurations are specified in terms of the aperture locations, the equivalent aperture locations for the two collector spacecraft must be determined. Using these configurations, we first scale the size of the interferometer such that the distance between the center of configurations and the farthest imaging locations is 500 m. The u-v points generated by these scaled configurations are then used to determine the equivalent x-y imaging locations given by:

$$\begin{aligned} u &= \pm\frac{2x_2}{\lambda} \\ v &= \pm\frac{2y_2}{\lambda} \end{aligned} \tag{2.15}$$

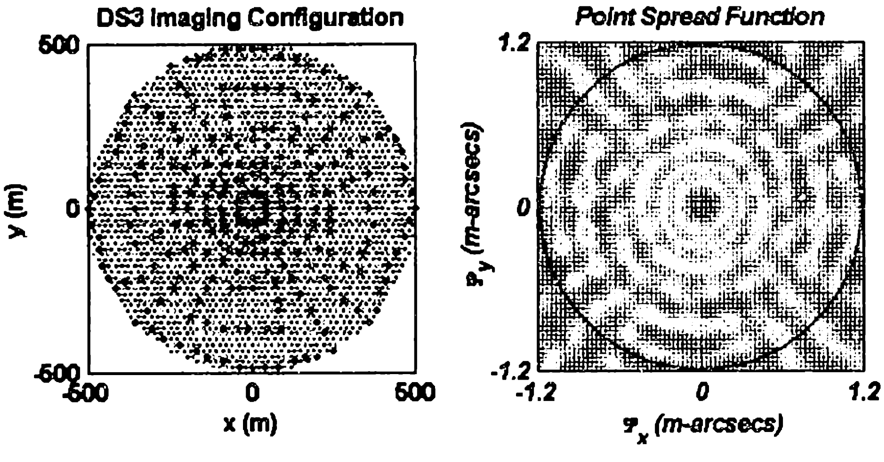

Figure 2.24 Discrctized DS3 imaging locations and its corresponding PSF.

where x_2 and y_2 are equal to $-x_1$ and $-y_1$ since the two collector spacecraft are located diagonally opposite to each other. Since the resulting imaging locations do not lie exactly on the pre-defined hexagonal grid, the closest grid point is used instead. The PSFs generated using these imaging configurations are shown in Appendix A.

Shown in Figure 2.24 are the discretized DS3 imaging locations and the corresponding PSF generated using these locations. Note that the imaging locations in the left figure tend to lie on straight lines, which is desirable if the collector spacecraft are allowed to 'Observe on the Fly'. This will be further discussed in Chapter 3. In the PSF map, a relatively narrow mainlobe is generated using these imaging locations. There exist, however, sidelobes across the PSF map.

Comparisons between the PSFs generated using the different imaging configurations are shown in Figure 2.25. The figure on the left shows the comparisons between the Golay, Cornwell and the optimized MSE imaging configurations while the figure on right compares the results from the optimized MSE and the DS3 configurations. Clearly indicated in the figure is the better performance of the optimized MSE imaging configurations. As the number of u-v points is increased, the configurations obtained using the optimized MSE continues to mimic the nominal PSF better than others. Hence, it is clear from Figure 2.25 that the optimized MSE imaging configurations are better at mimicking the nominal PSF when compared with the PSFs generated by the other imaging configurations.

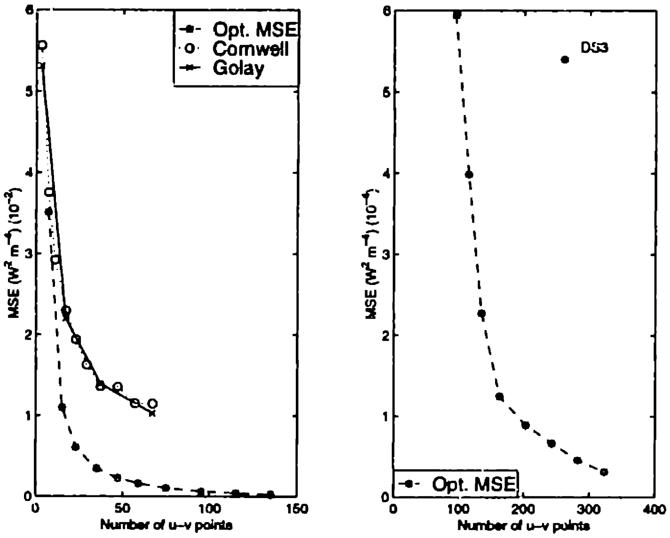

Figure 2.25 MSE comparison for the different imaging configurations.

The results obtained thus far assume that the collector apertures are much smaller than the baseline separation between apertures. The technique used to interfere the science light is based upon the Michelson interferometer. An interferometer operating in this mode usually assumes that the target remains the same throughout the imaging process, which is true for most astronomical sources. Terrestrial targets, however, tend to vary on short time scales. This then makes imaging terrestrial targets using a Michelson interferometer impossible. There exists, however, another type of interferometer, where imaging of these rapidly changing targets is made possible. Such an interferometer is known as the Fizeau interferometer and is discussed in the next section.

2.6 Fizeau Interferometer (Snap-Shot Mode)

In the Michelson interferometer, an image is obtained by taking measurements from only a subset of u-v points generated by a single monolithic aperture. In most circumstances, measurements at these u-v points are obtained over a period of time. It is assumed that the target remains unchanged during this period. There exist, however, targets that change rapidly over time. These targets can only be imaged with an interferometer that can provide full instantaneous u-v coverage. Such coverage can be obtained through the use of a single monolithic aperture or alternatively, a number of smaller apertures. Providing full instantaneous u-v coverage using multiple apertures is made possible through the use of a Fizeau interferometer.

As opposed to the Michelson interferometer, the Fizeau interferometer takes the combined science light from all the apertures and focuses it onto a multi-element detector, such as a multi-pixel Charge Coupled Device (CCD). Rather than just counting the number of photons hitting the detector, spatial information across the combined light beam is extracted through the multi-pixel detector. The Fizeau interferometer requires that all u-v measurements be made simultaneously and that there exist no gaps across the spectrum of the u-v measurements: full instantaneous u-v coverage.

A separated spacecraft Fizeau interferometer is currently being considered as a design option to image terrestrial targets for the NASA's New Millennium Program: DS3. Since the mass of a spacecraft is dependent upon the size of the apertures, among other components, the objective of this section is determine the minimum aperture size required for the collector spacecraft such that full instantaneous u-v coverage is still obtained. This minimum is determined based on the fill factor, which defines the ratio between the total collecting area of the interferometer and the area of a filled aperture of equivalent full u-v coverage. Full u-v coverage is defined as a radius in the u-v plane within which the imaging system acquires at least one measurement for all possible values of u and v. This is shown by the white circles in Figure 2.28 where the black regions indicate u-v points at which at least one measurement is taken. A filled aperture with equivalent u-v coverage corresponds to a filled circular aperture whose coverage in the u-v plane has this same radius.

In Fourier optics, the u-v distribution of an interferometer can be determined by correlating the apertures in the interferometer with themselves [Gorham, 1998]. This auto-correlation can easily be determined using a digital computer if the apertures are initially discretized into sub-elements. An example of the u-v point distribution using the Golay-6 imaging configuration is shown in Figure 2.26. The left plot shows the six discretized apertures while the plot on the right shows the distribution of the u-v points generated by these apertures. Since there are more short sub-element separations within these apertures, redundant u-v measurements are made for small values of u and v. This is clearly seen in the right plot as high occurrences of the small u-v components when compared to the large u-v components. The occurrence in this context refers to the number of times that a particular u-v separation exists in the system. Hence, by taking the auto-correlation function of the interferometer, not only the u-v coverage of the interferometer can be determined but the level of redundancy in the measurements acquired at different u-v points is also found.

In this application, however, we are only interested in finding the minimum sized apertures for which at least one measurement is made for all values u and v throughout the range of u-v cover-

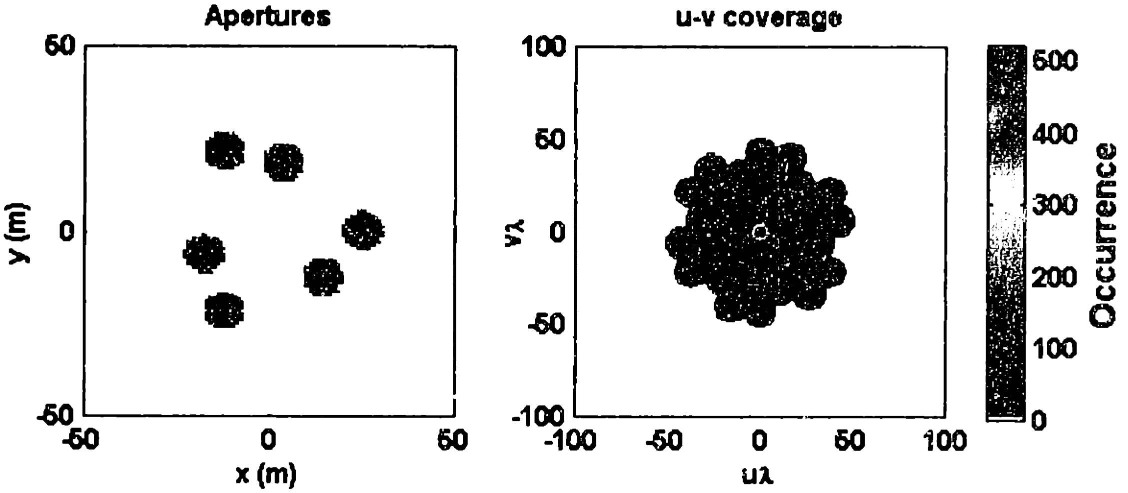

Figure 2.26 The u-v coverage distribution using the Golay-6 imaging configurations.

age. Even though the auto-correlation technique can be used, a bounding technique is developed instead. The advantage in using this bounding technique is due to its simpler computation in determining the interferometer's u-v coverage, especially when operates over a range of electromagnetic frequencies. This bounding method, however, does not give any indication about the redundancy in u-v point measurements. If this redundancy is needed, for signal-to-noise purposes, we will have to resort to the auto-correlation function method discussed in the above paragraph.

Hence, in this section, a bounding technique to determine the u-v coverage for a Fizeau interferometer is developed. This is done by first determining the coverage of a single and a two aperture system. In order to determine the performance for different numbers of apertures interferometers, a fill factor metric is introduced in Section 2.6.2. Then, using the Golay and Cornwell imaging configurations, which are optimized for snap-shot imaging, the minimum aperture size (minimum fill factor) required to provide a full instantaneous u-v coverage is determined. Even though there does not exist a single location for the combiner which is equidistant from all the collectors in the Golay configurations, it is assumed that optical delay lines can be implemented to ensure that the same wavefront from the target can be interfered. Finally, in Section 2.6.4, the aperture size required to obtain full instantaneous u-v coverage when a range of electromagnetic frequencies are interfered is determined.

2.6.1 Calculating u-v Coverage for Simple Systems

In the Michelson interferometer, the u-v coverage of the interferometer is dependent solely on the separation of the apertures. In the Fizeau interferometer, however, it is dependent on both the separation and the size of the apertures in order to provide the required full instantaneous u-v coverage. This couples minimum baseline to aperture diameter since measurements made at smaller u-v values than allowed by aperture separation must be made within individual apertures in order to ensure full u-v coverage. As a result, the size of the apertures is of the same order as the minimum separation between the apertures.

Since aperture diameter and minimum baseline separation are coupled, and the apertures are assumed to be equal, this analysis can be simplified by considering only the boundary which the aperture covers in the u-v plane since all smaller u-v values will be provided. Any circular aperture can be thought of as a compilation of contiguous sub-apertures. Each possible pairing of sub-apertures results in a measurement at a particular u-v value. The pairing of sub-apertures that are diametrically opposed provides a measurement at the largest u-v value. All other pairings provide measurements at smaller u-v separations. Therefore, to account for all u-v point measurements enabled by a single circular aperture, only the diametrically opposed sub-aperture pairings (boundary) need to be considered since all smaller u-v values are provided. As will be discussed, this simplification also applies to the u-v coverage of a multi-aperture system. First, determine the locus of all u-v points provided by pairing (within and between apertures) sub-apertures that lie on each aperture's boundary. Then, the regions within this closed locus will also be filled.

The determination of the u-v coverage due to a single aperture can be explained with reference to the single aperture plot in Figure 2.27. The single aperture is shown as a dashed circle with radius r centered about the origin. To determine the u-v coverage of this single circular aperture, the aperture must be auto-correlated with itself. Furthermore, since we are only concerned with the boundary of the aperture's u-v coverage, the u-v coverage of the single aperture can be determined by centering this same aperture of radius r, on the boundary of the original aperture and sliding its center around the circumference. As these imaginary apertures, shown as dotted circles in the figure, sweep out a region of full u-v coverage, one can clearly see that a circle of radius $2r$ centered about the origin will encompass this region. If this $2r$ radius circle is normalized by the wavelength of interest, then this circle will be the u-v coverage boundary of the single aperture. Hence, one can then conclude that a circular aperture of radius r has a u-v coverage of $2r/\lambda$ which corre-

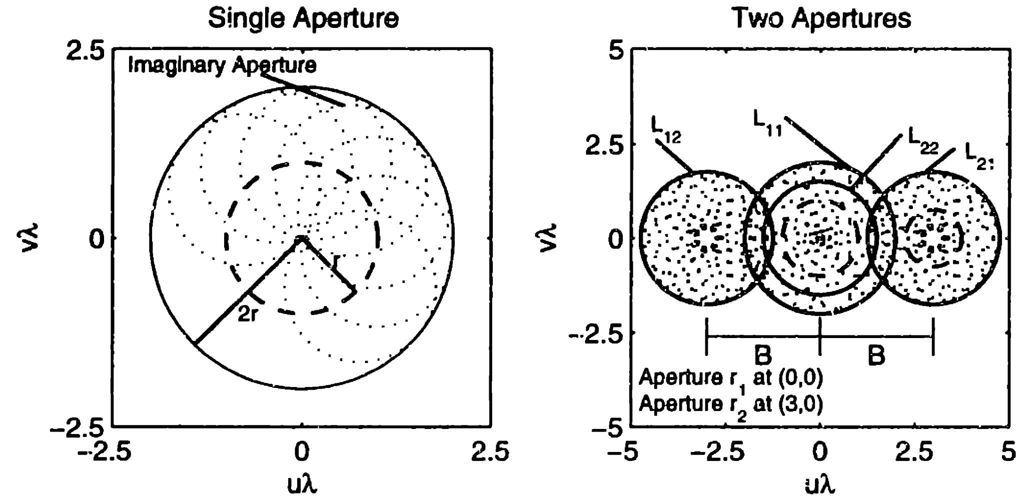

Figure 2.27 The u-v coverage for a single and two aperture systems.

sponds to the value of u and v that results from the pairing of sub-apertures on the aperture's boundary that are diametrically opposed across the apertures.

Applying this bounding technique to a two aperture system, the u-v coverage of an interferometer with two different apertures of radii r_1 and r_2 centered about (x_1,y_1) and (x_2,y_2) is also shown in Figure 2.27. Clearly seen in the figure is the u-v coverage of the interferometer bounded by three distinct circles. The first circle, denoted by L_{11} is the u-v coverage of the larger aperture. The second and the third circles, denoted by L_{12} and L_{21}, are the u-v coverage provided by the intra-aperture separations. These boundaries have a radius of $(r_1 + r_2)/\lambda$ centered about $\left(\frac{x_2 - x_1}{\lambda}, \frac{y_2 - y_1}{\lambda}\right)$ and $\left(\frac{x_1 - x_2}{\lambda}, \frac{y_1 - y_2}{\lambda}\right)$. Notice that these centers correspond to the u-v values associated with the aperture baseline, denoted by B in the figure. Even though only three circles in the u-v plane are seen in Figure 2.27, the u-v coverage is actually bounded by four circles with two located at the origin. However, due to the greater u-v coverage obtained from the larger of the two apertures, the u-v coverage from the smaller aperture, denoted by L_{22} in the figure, is located within the larger coverage. Since we are only interested in the boundary of the u-v coverage, the corresponding interferometer's coverage centered about the origin is given by $\frac{2}{\lambda}max(r_1, r_2)$. The regions denoted as L_{11} and L_{22} result from the auto-correlations of the two apertures and L_{12} and L_{21} result from cross-correlation. Even though an interferometer with two different aperture diameters is considered here, in the subsequent analysis, we will only consider apertures of the same size.

Extending this analysis further, we can now determine the u-v coverage for an N aperture interferometer. However, looking at Figure 2.27, how do we decide which of the two systems is better? In the next subsection, a metric based upon the total collecting area of the system and its u-v coverage is presented. This metric is known as the fill factor (FF) metric.

2.6.2 The Fill Factor (FF) Metric

In this section, we want to determine the minimum aperture size for a Fizeau interferometer such that its full instantaneous u-v coverage is equivalent to that of a filled aperture telescope with the same angular resolution. In this case, interferometers with small apertures are desirable since they require less mass and cost. In addition, high angular resolution (small values) in two directions is also desirable. Since we are only considering circular apertures in this study, the metric to be minimized can be given as a product of the two-axis angular resolution of the interferometer and its total collecting area subject to the constraint that full instantaneous u-v coverage is achieved. This is given by:

$$\begin{aligned} \theta_x \theta_y A_T &= \left(\frac{\lambda}{2R_{eff}}\right)\left(\frac{\lambda}{2R_{eff}}\right) A_T \\ &= \frac{\pi\lambda^2}{4}\left(\frac{A_T}{\pi R_{eff}^2}\right) \end{aligned} \tag{2.16}$$

where θ_x and θ_y are the angular resolutions in the x- and y- directions, A_T is the total collecting area, λ is the operating wavelength and R_{eff} is the radius of the equivalent filled aperture that provides the same u-v coverage and therefore angular resolution. In the equation, θ_x and θ_y are set to be equal because we are only considering circular apertures. Since the size of the apertures can be changed, which in turn affects the size of the equivalent aperture, and the operating wavelength is fixed, the only variables that exist in the equation are the ones grouped together within the parenthesis. Denoting n as the total number of apertures, each with radius r, the terms in the parenthesis can be rewritten as:

$$FF = n\left(\frac{r}{R_{eff}}\right)^2 \tag{2.17}$$

This relationship is known as the fill factor (FF) of the interferometer. This FF is a measure of the interferometer's total collecting area over the area of a filled aperture that can provide the same u-v coverage. This means that an interferometer with a small FF requires a small fraction of the collecting area of a filled aperture, of equivalent angular resolution, in order to provide full instantaneous u-v coverage. This is desirable since such a system would also have a small fraction of the filled aperture's mass and therefore cost.

As an example, we compare the two systems shown in Figure 2.27. The single aperture system shown in the figure has a *FF* of 1 since r is equal to R_{eff}. Assuming r_1 is the larger of the two apertures, the *FF* of the two aperture system is $1 + (r_2/r_1)^2$, where R_{eff} is again equal to r_1. Using the *FF* metric, we see that the addition of a second aperture did not increase R_{eff}, which therefore resulted in a higher *FF*. While measurements are made at additional u-v points, these points do not increase the circular area within which u-v coverage is full. From this, we can then conclude that it does not make any sense to include only a second aperture to reduce the *FF* of the interferometer.

Even though we saw that the *FF* performance of a single aperture is better than a two aperture system, there is no indication that an interferometer with more apertures will perform worse. As we will see in the next subsection, when more apertures are added to the interferometer, better *FF* performance is achieved.

2.6.3 Minimum Aperture Size - Single Frequency Results

As was mentioned before, in order to obtain full instantaneous u-v coverage, we must consider both the separation and the size of the apertures. However, rather than trying to determine the optimal aperture separations, the Golay and Cornwell imaging locations (Section 2.1.1 and Section 2.1.2), which are optimized for snap-shot imaging, are used instead. Using these imaging locations, the problem can then be reduced to just determining the minimum aperture size that gives the minimum *FF* performance.

The apertures that give the minimum *FF* for four Golay imaging configurations are shown in Figure 2.28. The size of the apertures (r), given in terms of the radius of the array (R), are shown in the left figures. The radius of the array, R, is defined as the distance from the center of the array to the center of the farthest aperture. The corresponding u-v coverages provided by these arrays are also shown in the figure. In each of these figures, the largest circle in which no u-v 'holes' exist, is shown in white. The non-dimensional radii of these circles, R_{uv}, are determined by visual inspection. Notice that for a fixed array dimension (R), increasing the number of apertures dramatically reduced physical aperture area. However, it also reduces the extent of full u-v coverage

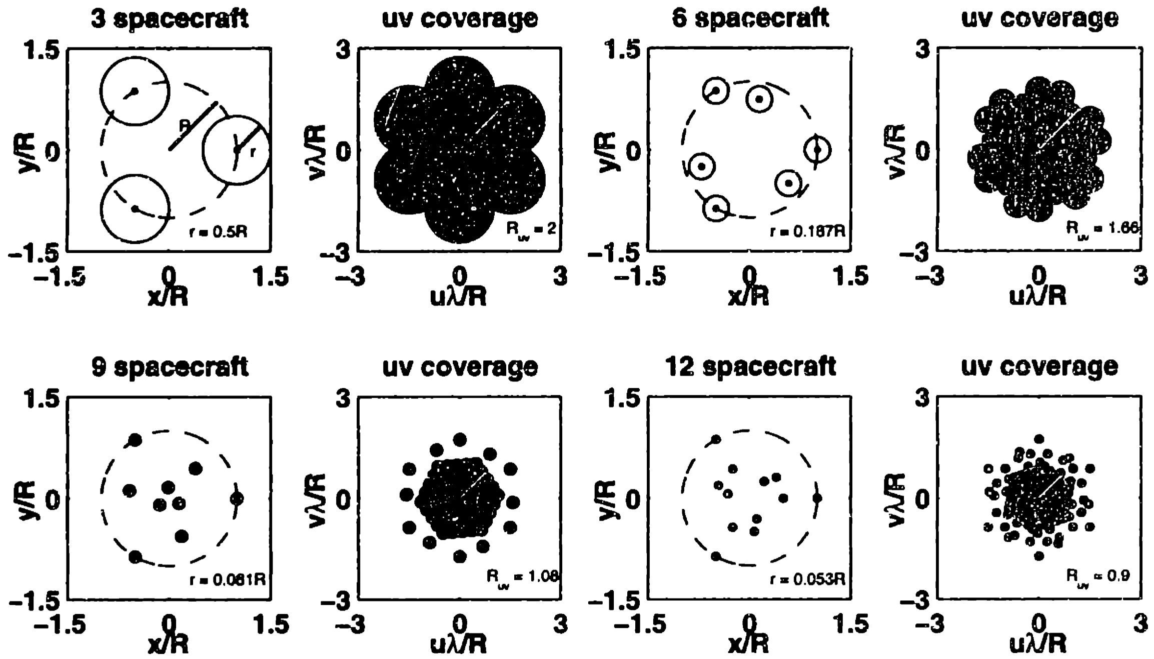

Figure 2.28 Minimum aperture size required to provide full u-v coverage for the Golay arrays.

(R_{uv}). Nonetheless, fill factor decreases as the number of apertures increases because the rate at which aperture area decrease outpaces reductions in u-v performance.

Also seen in the figure is the smallest separation between two apertures in the array is no more than two aperture diameters apart. Since both the intra- and inter- sub-aperture element separations contribute towards the u-v coverage of the interferometer, separations of greater than twice the diameter of apertures must be provided by the intra-aperture elements. To ensure a full instantaneous u-v coverage, the minimum separation between the elements on the two apertures must not exceed the diameter of the apertures, which means that the separation between the apertures must be at most two aperture diameters apart. Hence, in order to obtain a full instantaneous u-v coverage, the minimum separation between two apertures in the array must not exceed twice the diameter of the apertures.

The results using both the Golay and Cornwell imaging configurations are tabulated in Table 2.5. In terms of the non-dimensionalized parameters given in the table, the fill factor (equation 2.17) of the n aperture Fizeau interferometer can re-written as:

TABLE 2.5 Results for Golay and Cornwell configurations for monochromatic imaging.

No. of Points (n)	Golay Configurations			Cornwell Configurations		
	Aperture:Array (r/R)	u-v radius (R_{uv}/R)	F.F (%)	Aperture:Array (r/R)	u-v radius (R_{uv}/R)	F.F (%)
3	0.50	2.00	75	0.50	2.00	75
4	-	-	-	0.40	1.95	67
5	-	-	-	0.31	2.02	47
6	0.19	1.66	31	0.32	2.27	48
7	-	-	-	0.26	2.03	46
8	-	-	-	0.24	2.21	38
9	0.08	1.08	20	0.21	2.12	35
10	-	-	-	0.21 (0.18)	2.24 (1.14)	35 (100)
11	-	-	-	0.18	2.07	33
12	0.05	0.90	15	0.18 (0.15)	2.23 (1.27)	31 (67)

$$FF = n\left(\frac{r}{R_{eff}}\right)^2 = n\left[\frac{(r/R)}{(1/2)(R_{uv}/R)}\right]^2 \tag{2.18}$$

since R_{eff} is equal to half of R_{uv} for a single filled aperture. The general trend seen in the table indicates that FF decreases as the number of apertures is increased. For the Cornwell-10 and Cornwell-12 configurations, the minimum aperture size required to provide a full u-v coverage causes the apertures to overlap. Since this is physically impossible, the maximum aperture size is determined based upon the minimum separation between the spacecraft (values in parenthesis).

The FF results in Table 2.5 are also plotted in Figure 2.29. Comparison between the two indicates that smaller apertures can be used in the Golay imaging configurations. This is due to the compactness of the u-v points optimized using the Golay metric. On other hand, the Cornwell configurations are optimized for distributing the u-v points evenly and, therefore are not as compact and therefore efficient at providing full instantaneous u-v coverage. Even though the Cornwell configurations generate larger u-v coverages, larger apertures are required, which in turn increases the FF.

Operating a Fizeau interferometer using the Golay configurations requires smaller apertures when compared to an interferometer using the Cornwell locations. In the Golay configuration, however,

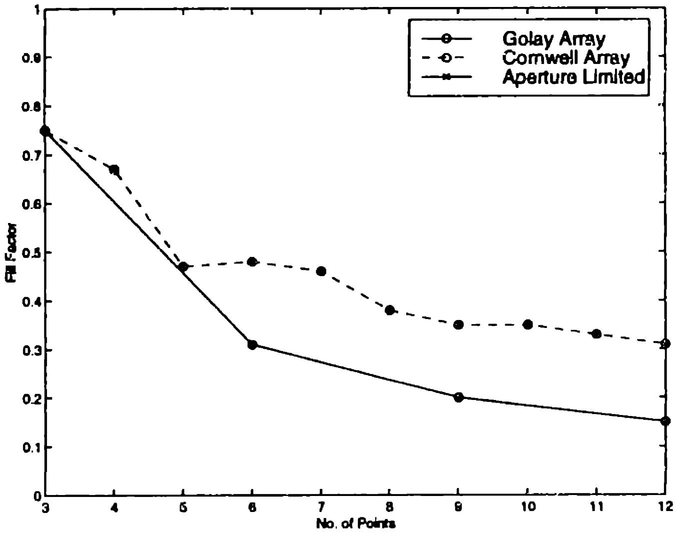

Figure 2.29 Fill factor comparison for the two imaging configurations.

there does not exist a location at which a combiner can be placed such that the same wavefront from the target can be combined. To overcome this problem, we can either introduce optical delay lines, or place the inner collectors farther away from the target, while the entire array still projects the same configuration as before. This, however, is not an issue if the Cornwell configurations are used since all the apertures are located on a circle. Therefore, selecting the best array configuration depends upon the efficiency with which differential pathlength is accommodated in the Golay configuration.

In this subsection, the interferometers were assumed to be operating at a single frequency. Hence, the u-v coverage of these interferometers varied with the size of the apertures only. From the definition of u and v in equation 2.1, the interferometer's coverage can also be varied by changing the operating frequency of the interferometer. This possibility is examined in the next subsection.

2.6.4 Aperture Size - Visible Spectrum

From equation 2.1, we see that the u-v coverage of a Fizeau interferometer can be affected by the separation and size of the apertures and also its operating frequency. In the previous subsection, the former is considered with the frequency being held constant. In this section, however, we will determine the aperture diameter that correspond to the minimum *FF* for an interferometer operating over a spectrum of frequencies.

TABLE 2.6 Results for Golay and Cornwell configurations for broad band imaging.

No. of Points (n)	Golay Configurations			Cornwell Configurations		
	Aperture:Array (r/R)	u-v radius (R_{uv}/R)	F.F (%)	Aperture:Array (r/R)	u-v radius (R_{uv}/R)	F.F (%)
3	0.50	2.00	75	0.50	2.00	75
4	-	-	-	0.38	1.89	65
5	-	-	-	0.29	1.90	47
6	0.16	1.52	27	0.20	1.98	24
7	-	-	-	0.18	1.80	28
8	-	-	-	0.15	1.91	20
9	0.07	1.09	15	0.15	1.97	21
10	-	-	-	0.12	1.85	17
11	-	-	-	0.11	1.78	17
12	0.04	0.85	11	0.10	1.98	12

In the previous section, the u-v coverage of the interferometer is normalized by its operating wavelength. Assuming that the Fizeau interferometer is operating over the entire visible spectrum, we can normalize the wavelengths of interest such that the normalized wavelength is bounded by 1 and 1.75. Separating these normalized wavelengths into ten distinct wavelengths, the total u-v coverage of the interferometer can then be determined by overlaying the individual u-v coverages. Note that changing the wavelength does not change the size of the aperture that corresponds to the minimum *FF*. This is because changing the wavelength only scales the size of the u-v coverage by the ratio that the wavelength is changed.

The results using both the Golay and Cornwell configurations are tabulated in Table 2.6. The fill factor in the table is calculated with respect to the single monolithic aperture required to provide the equivalent u-v coverage at the normalized wavelength of 1.0. In doing so, the size (R_{eff}) of the single filled aperture required to provide the equivalent full instantaneous coverage is the smallest since larger apertures are required only if longer wavelengths are used. As expected, the trend in the table indicates that as the number of apertures is increased, smaller apertures can be used to obtain full instantaneous u-v coverage.

Overlaying these results with those from the previous subsection, the two configurations can be compared (Figure 2.30). Clearly, the *FF* performance obtained with broadband light is better, particularly for the Cornwell configuration. This is to be expected as coverage of the interferometer is due to the contributions from a range of single frequency coverages. Also seen in the figure is the

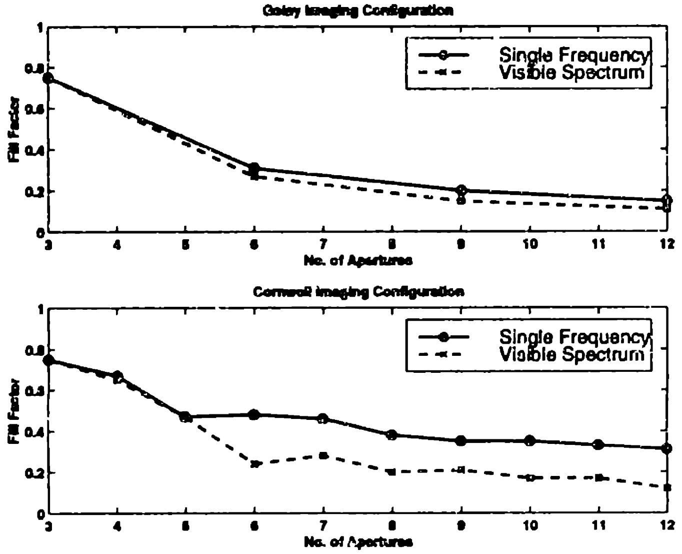

Figure 2.30 Fill factor comparisons between single frequency and multiple frequency imaging configurations.

significant improvement in *FF* for the Cornwell configurations. Since the u-v coverage of the Golay configurations are optimized to be as compact as possible, superimposing the coverages from different frequencies does not significantly improve the performance. With the Cornwell configurations, where the u-v points are more distributed, superimposing the coverages allows the low frequency coverages to cover the 'holes' that exist in the high frequency u-v coverages. The combination of these high and low frequency coverages therefore allows larger u-v coverage which reduces the fill factor of the system. To illustrate this, the u-v coverage of the Cornwell-10 configuration for both the single frequency and multiple frequency system are shown in Figure 2.31. Using the aperture size determined in the multiple frequency coverage, 'holes' in the

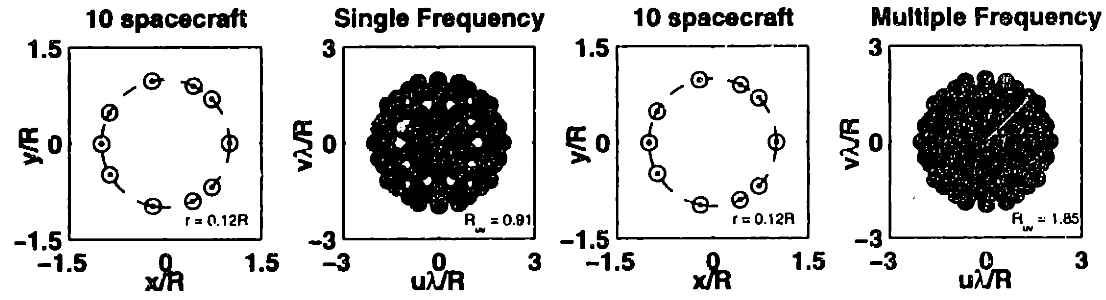

Figure 2.31 Single and multiply frequency u-v coverage comparisons.

u-v coverage of a single frequency system are observed. In the multiple frequency coverage, these holes are filled in by superimposing the coverage from different frequencies.

From equation 2.17, we see that the *FF* of a given number of aperture can be decreased by either decreasing the size of the apertures (r) or increasing the size of the u-v coverage ($R_{uv} = 2R_{eff}$). It was observed that it is more advantageous to try to reduce the size of the apertures than to enlarge the outer boundary of the u-v coverage in order to get a lower *FF*. This is especially true for configurations with higher numbers of apertures. In these high number of aperture configurations, the increase in the total aperture area is more significant than the u-v coverage increase when the size of the apertures is increased. The more significant increase is due to the fact that the total aperture area is the sum of all the aperture areas. Hence, in these circumstances, it is better not to increase the size of the apertures.

For simplification, the apertures in this analysis are constrained to have the same size. Careful inspection of the aperture locations with respect to each other will reveal that the smallest separation between two apertures in the physical plane is no more than two aperture diameters apart, especially for the single frequency analysis case. These small aperture separations are required to provide the small u-v components in the u-v coverage. Since it is not safe to formation fly these apertures at such close proximities, the analysis may have to be performed such that varying aperture sizes is allowed. For example, rather than formation flying two small apertures close to each other, it may be better to replace these two small apertures with a larger aperture to provide the small u-v components of the coverage while smaller apertures are used to provide the larger u-v components. Another possible solution is to structurally connect these apertures while the large u-v components are provided by apertures on different platforms. This hybrid design, using structurally connected and separated spacecraft in the same system, is proposed as a design alternative to the DS3 Earth Imager by the Space Systems Laboratory at MIT [Miller et al, 1998].

2.7 Summary

In this chapter, the optimal apertures locations for a separated spacecraft interferometer were determined. Imaging configurations that have been proposed for both radio and optical interferometry were discussed and used to compare with the results obtained. The Golay and DS3 imaging configurations were developed for visible interferometry while the Cornwell points were initially developed for instantaneous imaging in the radio regime.

The notion of Point Spread Function (PSF) was introduced and a metric based on how well the interferometer can mimic a nominal PSF was developed. This metric is known as the image Mean Square Error (MSE) metric.

Using the simulated annealing optimization technique, the optimal MSE aperture locations, given a limited number of aperture locations, for both radio and optical interferometers were determined. As the number of aperture locations is increased, better MSE performance is obtained. In fact, the relationship between the MSE metric and the number of imaging locations can best be described by a second order inversely proportional curve. Comparing the results with the already proposed configurations, the optimized MSE configurations are much better at mimicking the nominal PSF. Rather than trying to mimic the entire nominal PSF image, the analysis developed in this chapter also allows one to penalize within a selected region of the PSF. This optimization is one the advantages that the methodology developed in this study has over other methods.

The optimal imaging locations for a two collector and one combiner spacecraft operating in the visible regime were also determined. The results obtained were found to perform much better than proposed configurations such as the DS3 configuration.

Array characteristics for a Fizeau interferometer were also determined in this chapter. Using the Golay and Cornwell configurations, the aperture size required to provide full instantaneous u-v coverage is determined for an interferometer operating in the visible regime. A metric to compare the coverage from the different configurations is defined. This metric, the fill factor ratio, is defined as the ratio of the total aperture area of the interferometer to the largest single aperture area that can provide the same u-v coverage. The lower this number, the better the interferometer's mass efficiency in providing u-v coverage.

The results for single frequency coverage favor the Golay configurations. However, when the entire visible spectrum is considered in the interferometer's u-v coverage, significant reductions in fill factor occur for the Cornwell configurations. This is attributed mainly to the fact that the 'holes' in the high frequency coverage are filled by the low frequency coverage of the interferometer. This improvement is not evident in the Golay imaging configurations since these points are optimized for compactness.

Hence, in this chapter, the optimal imaging locations for interferometer operating as a Michelson interferometer are determined. These imaging locations are used in the next chapter to determine the optimal spacecraft trajectories to image the target. Also in this chapter, the minimum aperture size for a Fizeau interferometer required for imaging rapidly changing targets is also determined. These results can be used to design an Earth Imager system, which is a design option for the New Millennium DS3 program.

Chapter 3

IMAGING OUTSIDE OF A GRAVITY-WELL

In Chapter 2, the optimal imaging locations for a two collector and one combiner spacecraft operating in the visible regime were determined using the Mean Square Error (MSE) metric. In that optimization, we constrained the imaging locations to lie on the plane that is perpendicular to the interferometer's line of sight (LOS). If the interferometer is placed outside of a gravity-well, the it is assumed that the motion of the spacecraft depends only on the firing of their thrusters. In this chapter, the optimal trajectories for an interferometer located outside of a gravity-well are determined. The spacecraft trajectories within the Earth's gravity-well are examined in Chapter 4.

Solving optimal trajectory problems is not new. An excellent text by Kirk entitled 'Optimal Control Theory' presents solutions to time and fuel optimal problems. However, due to the large and discrete nature of the optimization space presented to us, a different method is used. This large trajectory optimization problem is also known as the Travelling Salesman Problem (TSP). The optimal trajectories determined in this study were found using some of the algorithms [Lin, 1965] developed to solve the TSP.

Since the Earth's atmosphere usually attenuates or scatters electromagnetic waves, the performance of a ground-based imaging system is usually degraded. This is especially true for a system operating in the visible regime. By going to space, the performance of the system can be much improved. In fact, the Hubble Space Telescope is reported to an have angular resolution which is ten times better any ground-based telescopes. Hence, to improve the performance of a visible telescope, one obvious choice is to place it in space. The ultimate choice, however, is to use a space-based multiple aperture interferometer, such as a separated spacecraft interferometer (SSI).

Outside of a gravity-well, a SSI interferometer can operate in two modes: the 'Stop and Stare' mode; and the 'Observe on the Fly' mode. Imaging in the 'Stop and Stare' mode requires the spacecraft to be held stationary relative to each other when interferometric measurements are made. This mode, though easier to implement, usually requires more resources. The second mode, however, allows the spacecraft to move relative to each other during the entire imaging sequence. Since the relative locations of the spacecraft must be known precisely, this presents a major technological challenge to ensure the same wavefront from the target is interfered at the combiner spacecraft. Even though this second method requires less resources, we only consider the 'Stop and Stare' imaging mode in this study.

In the next section, we develop the two metrics that are used to determine the spacecraft's optimal trajectories. To compare the different imaging trajectories, the mass estimates for the NASA's DS3 mission are used in this study. The travelling salesman algorithm, an heuristic algorithm used to determine these optimal trajectories, is presented in Section 3.1.3. In Section 3.2, we determine the optimal trajectories for a two collector and one combiner spacecraft visible interferometer. The interferometer is assumed to be operating in the 'Stop and Stare' imaging mode. Allowing the number of collectors in the interferometer to be a free variable, the optimum interferometer architecture is determined in Section 3.3. The issues that were not considered in this analysis are discussed in Section 3.4. Finally, the findings in this chapter are summarized in Section 3.5.

3.1 Trajectory Optimization - 'Stop and Stare'

In this section, we present two different performance measures by which the optimal trajectories for a two collector and one combiner interferometer are determined. The two performance measures are propellant mass and imaging time. In the case of a three spacecraft interferometer, the total mass of the interferometer consists of its dry and propellant masses. Since the dry mass of the interferometer is fixed, the total system mass can be minimized by determining the propellant required to move these spacecraft to their pre-determined imaging locations.

Due to the emergence of highly efficient space propulsive units, the propellant requirement for spacecraft to carry out a mission can be significantly reduced. In cases where the total propellant requirement is very small compared to the spacecraft dry mass, it does not make sense to determine the interferometer's optimal propellant trajectories. Rather, the time in which the interferometer can acquire an image is used.

Throughout this analysis, two important assumptions are made. The first is the acceleration of the spacecraft is assumed constant throughout the entire mission. This is not entirely true since the mass of the spacecraft changes as propellant is consumed throughout the maneuvering sequence. However, it does seem more reasonable to assume that the acceleration is constant during a single image sequence.

The second assumption made is that the total imaging time is only affected by the time required to maneuver these spacecraft. Integration time for the collector spacecraft at each imaging location is assumed to be in the order of minutes while the spacecraft maneuvering time between two consecutive imaging locations is in the order of hours [Linfield, 1997].

In the following subsections, we present the two metrics that are used to determine the optimal trajectories for a DS3 like interferometer. The travelling salesman algorithm used to determine these trajectories is also presented. Before presenting the results in the next section, the DS3 mission parameters are also presented.

3.1.1 Mass Metric

The objective in this optimization is to determine the trajectory that the spacecraft should take such that minimum propellant is expended. Given the locations that spacecraft must traverse to, the minimum propellant trajectory is obtained by determining the minimum time that the spacecraft should fire its thrusters between x-y imaging locations throughout the imaging sequence or alternatively, the spacecraft coasting time should be maximized. Such a trajectory can be achieved by using a trapezoidal velocity profile where the spacecraft accelerates and decelerates with an acceleration of a, for a period of time t_a in each case, and coasts for a time of t_b. Therefore, the coasting time for a spacecraft traversing the distance s_i between two consecutive imaging locations, i and i+1, is determined to be:

$$t_{bi} = \frac{s_i - at_{ai}^2}{at_{ai}} \tag{3.1}$$

However, if the spacecraft are allowed to take an infinite amount of time to carry out the imaging sequence, the propellant expended will be infinitesimally small. Hence, to obtain the minimum mass trajectory, a maximum imaging time must be specified. The total imaging time constraint equation is then given by:

$$\sum_{i=1}^{N} (2t_{ai} + t_{bi}) = T_{\text{image}} \tag{3.2}$$

Substituting equation 3.1 into equation 3.2, and making the assumption that t_{ai} is the same for all i to simplify the problem, the total firing time, T_{acc} (= Nt_a) is therefore:

$$T_{acc} = \frac{T_{\text{image}} \pm \sqrt{T_{\text{image}}^2 - 4\frac{N}{a}\sum_{i=1}^{N} s_i}}{2} \tag{3.3}$$

where the acceleration of the spacecraft is simply the thrust produced by the propulsion system divided by the mass of the spacecraft and, the summation of s_i is a function of the spacecraft trajectory. Even though there are two possible solutions, only the solution with a smaller T_{acc} value is accepted since the solution with the larger T_{acc} gives a negative coasting time. The smaller T_{acc} value corresponds to the solution with the minus (-) sign in equation 3.3 as the value in the square-root is always less than T_{image}, if a feasible solution does indeed exist.

Finally, given the specific impulse of the propulsion unit, I_{sp}, and the acceleration of the spacecraft, a, the propellant to spacecraft mass ratio required by a collector spacecraft to traverse through the x-y imaging trajectory is:

$$\frac{m_{prop}}{m_{sc}} = \exp\left(\frac{\Delta V}{I_{sp}g}\right) - 1 \tag{3.4}$$

where g is Earth's gravity and ΔV is equal to aT_{acc}.

3.1.2 Time Metric

In cases where the propellant requirement is very small compared to the spacecraft mass, rather than considering the propellant mass, the minimum time required for the spacecraft to complete the imaging process is more desirable. This is especially true when high specific impulse thrusters such as Pulse Plasma Thrusters (PPTs) are used. PPTs have a specific impulse in the order of 1000 s with a maximum thrust of only 5 mN when operated at full power [Linfield, 1997]. The amount of teflon required for the PPTs is small compared to the total spacecraft mass, hence a better metric is to compare the time required to obtain an image. The thrust produced by PPTs is dependent upon the power available to the propulsion unit. Generally, a linear relationship between spacecraft power and the PPT thrust is assumed and hence, the limitation in the time optimized trajectory lies in the spacecraft power.

As opposed to the mass metric described in the previous subsection, this second form of trajectory optimization calls for the minimization of the total spacecraft maneuvering time required to complete the trajectory given a fixed acceleration. In this case, the coasting time is set to zero such that the thruster firing time is maximized. The shortest time required for a spacecraft to travel between imaging locations, given that the spacecraft velocities at those locations are zero, is to follow a triangular velocity profile. That is, the spacecraft accelerates to the mid-point of the two imaging locations and decelerates until the spacecraft comes to a stop at the destination. Therefore, the time required for the spacecraft to traverse a given trajectory is:

$$T = \frac{2}{\sqrt{a}} \sum_{i=1}^{N} \sqrt{s_i} \tag{3.5}$$

Hence, optimizing the time trajectory involves minimizing the sum of the square-rooted distance between all the imaging locations.

3.1.3 Optimization Strategy - Travelling Salesman Algorithm

The two optimization problems discussed above are equivalent to the more commonly known problem, the Traveling Salesman Problem (TSP) [Lin, 1965]. There is a considerable amount of literature published regarding methods to solve the TSP. Due to the large optimization space, it is impossible to determine the global minimum to these problems within a reasonable computation time. In these problems, the number of states that must be considered grows prohibitively large with the number of locations. However, highly efficient heuristic algorithms are available to solve the TSP with large numbers of states. Even though the solution obtained cannot be guaranteed to be the global minimum, a solution close to the global minimum is achieved within a short computation time.

A simple TSP algorithm is adopted for the two trajectory optimizations. The algorithm allows a randomly chosen point on the trajectory to be either swapped with another randomly chosen point on the trajectory or inserted at a randomly chosen location on the trajectory. The cost of the tour is then calculated and accepted only if the cost achieved with the new trajectory is less than the currently accepted trajectory. This algorithm is found to be quite efficient and the solution to the optimization is determined when no new solution is accepted for more than 15000 consecutive trials. Similar to the optimization procedure in Chapter 2, the optimization was carried out three times in each case with only the best result being presented.

3.1.4 Mission Parameters

To allow comparison of the different imaging configurations, estimates for the spacecraft mass and propulsion characteristics must be made. The spacecraft masses adopted in this study are consistent with those proposed for the DS3 mission [Blackwood et al, 1998], where the collector spacecraft mass is set at 150 kg and the combiner is set at 250 kg.

To ensure that light from the target reflected from each of the collector spacecraft to the combiner spacecraft is combined at the same wavefront, the distances from the collector spacecraft to the combiner spacecraft must be kept the same. For a two collector and one combiner spacecraft interferometer system, this can be achieved by placing the spacecraft at the vertices of an isosceles triangle. Even though the equal path length requirement is met with an isosceles triangle configuration, the angle that the reflected light makes with the collector spacecraft plane is fixed at 60°. This angle is fixed because it is assumed that the combiner spacecraft design does not allow

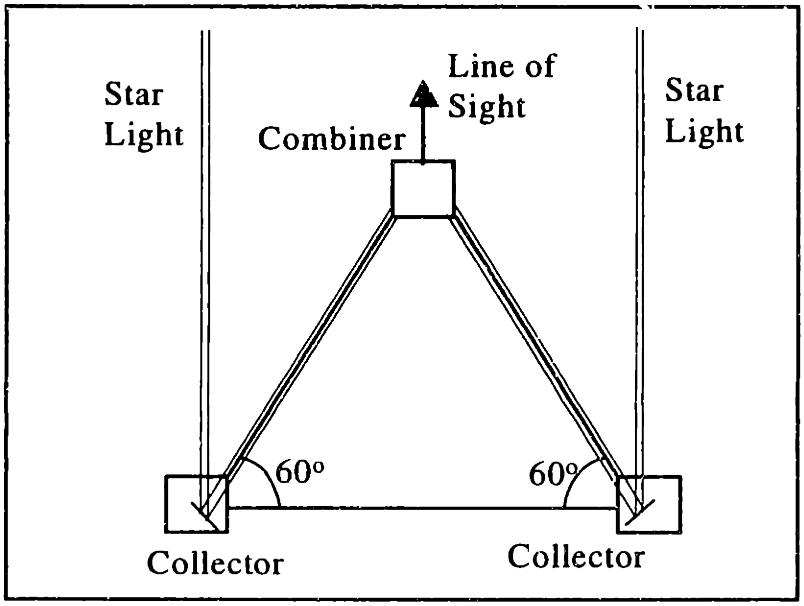

Figure 3.1 Three spacecraft interferometer imaging configuration.

reflected light to be received at varying angles. Hence, the three spacecraft will form an equilateral triangle as shown in Figure 3.1.

In this analysis, we consider two types of propulsion systems. The first one is a cold gas, GN_2, propulsion system, which produces 4.5 mN of thrust with I_{sp} between 50 s and 75 s [Larson et al, 1992]. Each of the spacecraft is assumed to be equipped with 12 such thrusters with 2 thrusters available in any one direction. Hence, the total thrust available for each spacecraft is 9 mN in any one direction. In this analysis, an I_{sp} of 62.5 s is assumed for the propulsion system.

Work by Linfield suggests that the DS3 system requires approximately 264 hours to image a source [Linfield, 1997]. Due to the rather low levels of thrust produced by the cold gas propulsion system, the 264 hours imaging time is chosen as the time constraint to ensure that the spacecraft can complete the imaging sequence within the specified time. Using this value, the number of targets that the interferometer can image in 6 months is approximately 16. From equation 3.4, the propellant to spacecraft mass ratio required to obtain N_{image} images is therefore:

$$\frac{m_{prop}}{m_{sc}} = \exp\left(\frac{N_{\text{image}}\Delta V}{I_{sp}g}\right) - 1 \tag{3.6}$$

The second propulsion system that is considered in this work are PPTs. PPTs are highly efficient propulsion systems with high specific impulse (1000 s). PPTs, however, produce very low levels of thrust. A system with 40 W of power allocated to the PPTs will have only a maximum thrust of 0.7 mN [Linfield, 1997]. Due to the low levels of thrust and the high specific impulse, the required propellant mass is very small compared to the overall spacecraft mass. Hence, it makes more sense to compare the total imaging time between the different imaging configurations when PPTs are used. Both the cold gas and the PPTs are currently being considered for the DS3 mission [Gallagher et al, 1998].

3.2 Two Collector Interferometer

Using the metrics, the optimization strategy and the mission parameters presented in the previous section, we are now ready to determine the optimal trajectories for the two collector and one combiner spacecraft interferometer. We assume that the interferometer operates in the 'Stop and Stare' imaging mode.

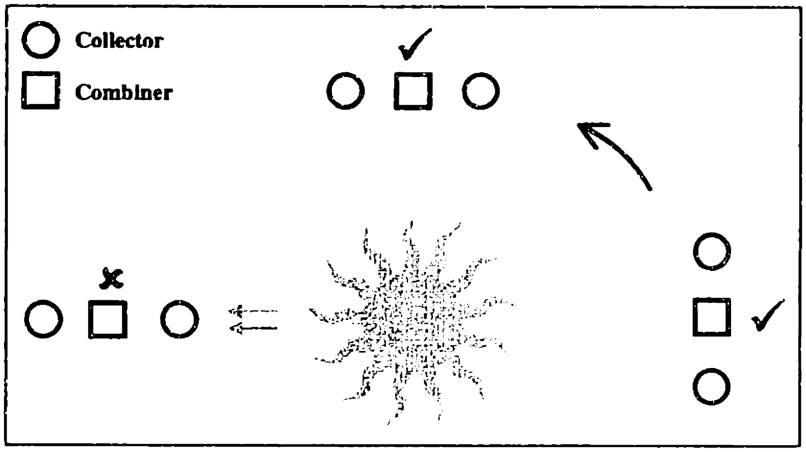

Figure 3.2 Imaging constraint due to combiner-collector-sun angle.

Since we are considering only a two collector interferometer, the origin of the interferometer can be set at the mid-point between the two collector spacecraft. In doing so, when we place the first collector at (*x*,*y*), the second is then automatically located at (-*x*,-*y*). Due to this constraint, we can then reduce the optimization to just determining the optimal trajectories for one of the two collector spacecraft.

In DS3, the proposed imaging configuration is divided into four quadrants with each spacecraft traversing through the locations in two of the four quadrants. To image a target, it was determined that each spacecraft will take interferometric measurements in their first quadrant and then traverse their second quadrant three months later. The reason for this is due to angle at which the three spacecraft are oriented with respect to the Sun. Assuming that the interferometer is imaging a target that is located normal to the ecliptic, depending upon the location of the interferometer in its orbit around the Sun, it is only possible to image the target by placing the collector spacecraft in two of the four quadrants. Since the science light is reflected off the collector to the combiner, the orientation of the collector spacecraft to the combiner in one of the quadrants will allow the combiner to see the light from the Sun as well, which would overwhelm if not damage the system. However, by placing the two collectors in the two allowable quadrants to image the target, the resolution in the orthogonal direction can therefore be obtained three months later by moving the spacecraft to the other two quadrants. Both the allowable and not allowable spacecraft locations as viewed from the above the ecliptic are shown in Figure 3.2.

In the DS3 mission, establishing metrology lock between spacecraft separated by at least 100 m is not a trivial exercise. Rather than expending resources to re-establish the metrology lock after a maneuver, the three spacecraft are to remain in an equilateral triangle even when they are moving

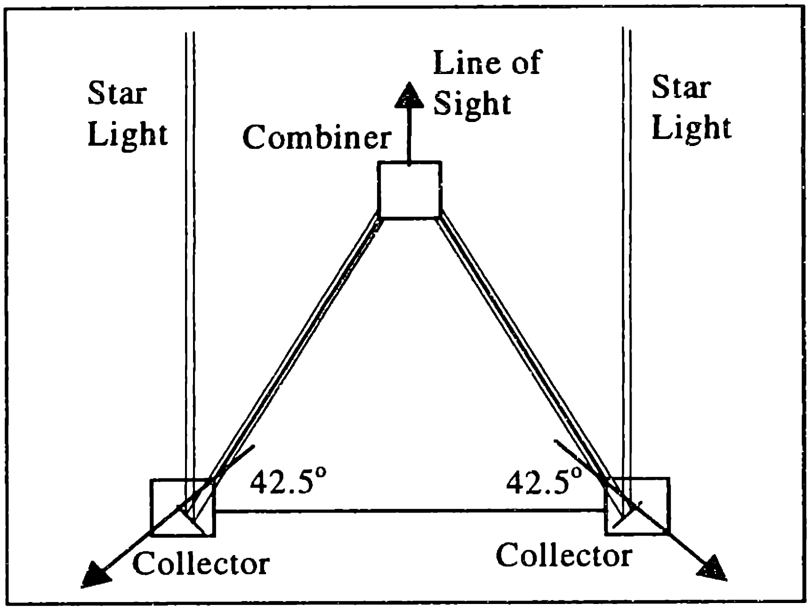

Figure 3.3 Collector spacecraft thruster firing at 42.5° due to the difference in the propulsive acceleration produced on the spacecraft.

relative to each other. In order to do so, the collector spacecraft must be thrusted at 42.5° to the imaging plane if the combiner spacecraft is restricted to be along the interferometer's line of sight (LOS) [Linfield, 1997]. Thrusting the collector spacecraft at this angle is required because the collector and combiner spacecraft have different mass but use the same propulsive system. To simplify the analysis, the z component of the collector's location is determined by multiplying the distance from the center in the x-y plane by the tangent of 42.5°. Hence, at the location (x,y), a collector spacecraft will be at the coordinates $(x,y,-z)$ with the second collector at $(-x,-y,-z)$. The combiner spacecraft is then located on the z-axis forming the third vertex of the equilateral triangle. Figure 3.3 illustrates the above discussion.

In this section, the results for the minimum propellant and the minimum time trajectories are presented. Comparisons of the results obtained using the different imaging configurations are made in Section 3.2.4. Following this section, we discuss the impact that a multiple spacecraft interferometer has on the total interferometer mass. We begin by determining the optimal trajectories using the equivalent Cornwell imaging locations.

3.2.1 Cornwell Imaging Configurations

In Chapter 2, the PSF for a visible interferometer using the Cornwell configuration was obtained using the equivalent collector spacecraft locations that provide the same u-v separations. Using

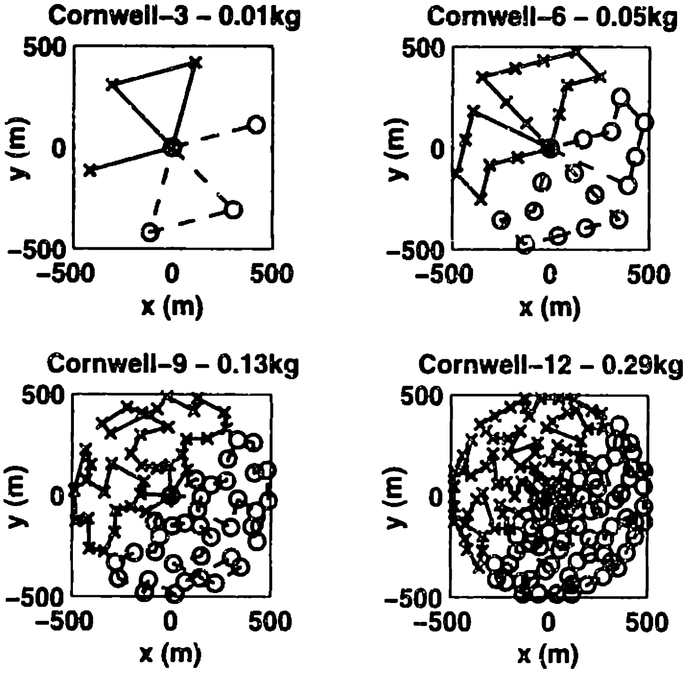

Figure 3.4 Examples of optimal propellant trajectories for a two collector interferometer using the equivalent Cornwell imaging locations.

these same imaging locations, the trajectories optimized using both the mass and time metrics are determined in this subsection.

Mass Metric

A sample of the optimal propellant trajectories obtained for a two collector interferometer using the equivalent Cornwell imaging locations are shown in Figure 3.4. Since the combiner spacecraft is required to form an equilateral triangle with the two collector spacecraft, one can see that the optimization tends to connect locations that are on same radial distance from the center. This can be attributed to the fact that propellant is required to move the combiner spacecraft when the collector spacecraft are moved in the radial direction. However, when the collector spacecraft traverses in the angular direction, the combiner spacecraft is not required to move at all. This is the reason why the collector spacecraft tend to sequentially take measurements at imaging locations that are at the same radial distance. The optimal collector spacecraft trajectories for all the equivalent Cornwell imaging configurations considered here can be found in Appendix B.

Comparison of the propellant usage using the different numbers of the equivalent Cornwell imaging locations is shown in Figure 3.5. In the plot, the y-axis is the total propellant mass required for

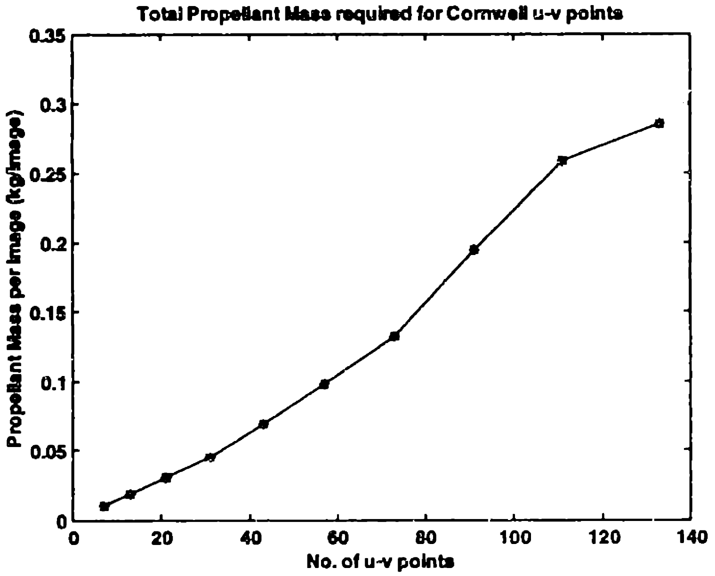

Figure 3.5 Total propellant mass required for the spacecraft to traverse through the equivalent Cornwell imaging locations.

the three spacecraft to obtain an image while maintaining the equilateral triangle configuration as required. Plotted on the x-axis is the equivalent number of unique u-v points generated using the Cornwell imaging locations. The results show that as the number of u-v points is increased, more propellant is required to maneuver these spacecraft. This makes sense because as the number of imaging locations is increased, the distance that the spacecraft travels must also increase, which in turn requires more propellant for the spacecraft to complete their trajectories. Also as the number of imaging locations is increased, the spacecraft need to stop and start more often.

In determining the propellant required to maneuver the spacecraft, the Cornwell imaging locations are divided into four quadrants due to the limitation imposed by the Sun (Section 3.2). The division of the imaging locations into quadrants is done arbitrarily without resorting to any optimization in order to obtain lower propellant mass results. Since the equivalent Cornwell imaging locations are quite evenly distributed, assigning an imaging location in one quadrant and not the other does not affect the results in a major way. The savings of spacecraft propellant in one quadrant will result in expenditure of propellant in the other quadrant and on average, will result in the same amount of propellant usage. Also, since more total propellant is expended when the collector spacecraft traverses in the radial direction as opposed to the angular direction, dividing the imaging locations in four quadrants radially from the center has little effect on the results. Hence, based on these two arguments, the optimal division of the imaging locations was not performed.

Time Metric

Using the same equivalent Cornwell imaging locations, the minimum time imaging trajectories for a two collector spacecraft interferometer are also determined. Examples of these optimal trajectories are shown in Figure 3.6. From equation 3.5, the minimum time trajectory can be determined by finding the trajectory with the smallest total square-root distance between imaging locations on the trajectory. In Figure 3.6, we see that the optimization tends to join imaging locations that are close to each other rather than locations that are located on the same radial distance from the center as seen in the optimal propellant trajectory case. Again, it is possible to obtain more optimal trajectories if the imaging locations are optimally divided into the appropriate quadrants.

The imaging time required for the two collector interferometer to obtain an interferometric image as a function of the equivalent number of Cornwell u-v points is plotted in Figure 3.7. The plot indicates that as more interferometric measurements are made, the time required to move the spacecraft through the trajectory is increased. This relationship is expected as the number of locations is increased, the distance that the spacecraft have to traverse increases as well. This then increases the total time required for the spacecraft to complete the trajectory.

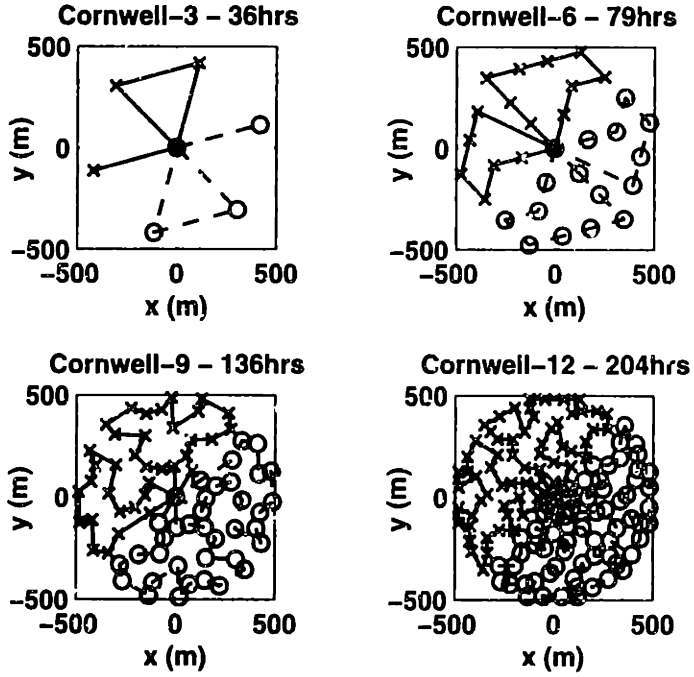

Figure 3.6 Examples of optimal time trajectories for a two collector interferometer using the equivalent Cornwell imaging locations.

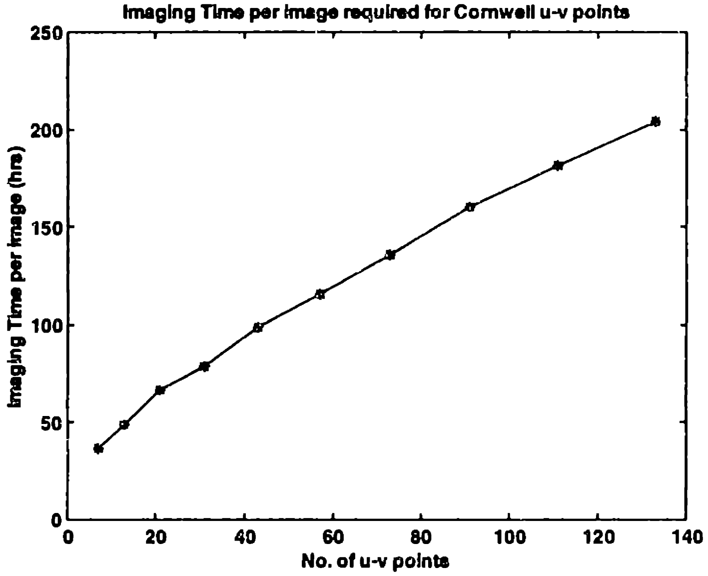

Figure 3.7 Imaging time per image for a two collector spacecraft interferometer using the equivalent Cornwell imaging locations.

Hence, in this subsection, we have determined both the optimal propellant and time trajectories for a two collector and one combiner interferometer using the equivalent Cornwell imaging locations. In the next subsection, we present the proposed DS3 imaging trajectory, which is neither propellant or time optimized. The optimal trajectories using the DS3 imaging locations are therefore determined.

3.2.2 DS3 Imaging Trajectory

The imaging trajectory for the DS3 mission that is proposed by Linfield is shown in Figure 3.8. This pattern was selected as a 'strawman' maneuver profile for estimating other mission parameters. This trajectory has measurements being taken at approximately every 50 m for each of the collector spacecraft. This equates to 131 unique imaging locations for each collector spacecraft and therefore generates the 261 unique u-v points.

The imaging time quoted for the two collector spacecraft to complete the imaging trajectory using PPTs is 264 hours in the 'Stop and Stare' imaging mode [Linfield, 1997]. However, using the algorithm developed in this study, the time required for the collector spacecraft to complete the trajectory shown in Figure 3.8 is 328 hours. This difference occurs because of the simplifying assumptions made in Linfield, 1997. It is assumed that all the spacecraft imaging locations are 50 m apart. This, however, is not possible if the imaging trajectory in Figure 3.8 is used as not all the

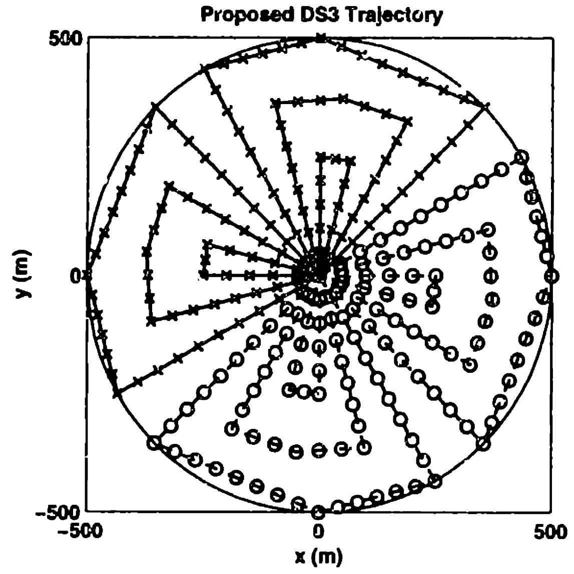

Figure 3.8 DS3 imaging trajectory proposed in Linfield, 1997.

distances between the points where the spacecraft are required to change direction are multiples of fifty. In this work, the imaging locations between the points at which the collector spacecraft are required to change direction, are distributed as evenly as possible and as closely as possible to the 50 m division. Due to this re-distribution of locations, the time required to traverse through the entire trajectory in a 'Stop and Stare' mode is therefore longer than the value quoted in Linfield, 1997. For comparison purposes, we use the re-distributed imaging time calculated using the metric developed in this study.

The treatment in Linfield, 1997, did not include other propulsion systems. Using the trajectory shown in Figure 3.8 and the mass estimates presented in Section 3.1.4, the total propellant mass required for the three spacecraft to complete their respective trajectories is 0.83 kg. This calculation assumes that all three spacecraft use the cold gas propulsion system.

Minimum Mass DS3 Trajectory

There exist, however, more optimal ways to maneuver the spacecraft through the DS3 imaging locations. Using the DS3 imaging locations, the minimum mass trajectory for the collector spacecraft is determined using the travelling salesman algorithm and is shown in Figure 3.9. Using this minimum mass trajectory, the total propellant mass required to obtain an image is 0.75 kg. This represents a savings of 9.64% over the DS3 trajectory proposed in Figure 3.8.

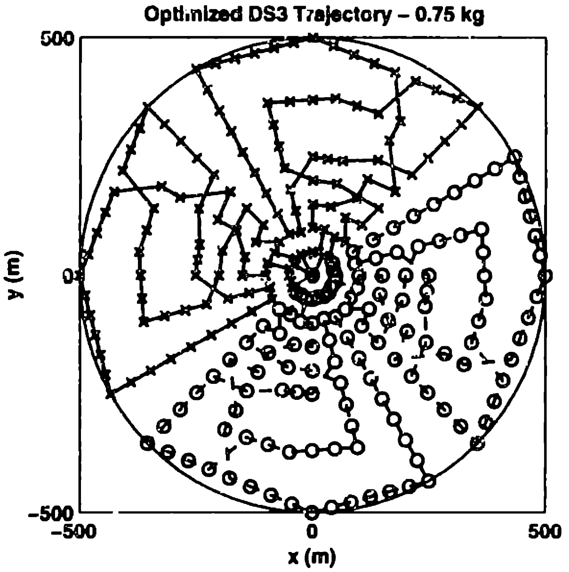

Figure 3.9 Optimal mass trajectory using the DS3 imaging locations.

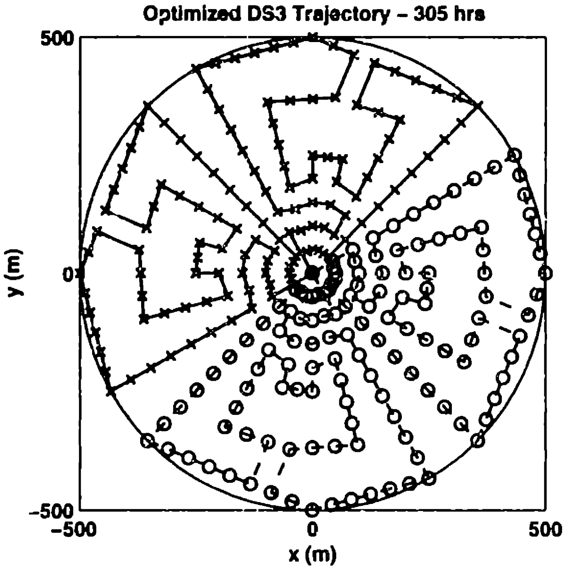

Figure 3.10 Optimal time trajectory using the DS3 imaging locations.

Minimum Time DS3 Trajectory

Equivalently, the minimum time trajectory using the re-distributed DS3 imaging locations is also determined and is shown in Figure 3.10. The time required to maneuver the spacecraft through these re-distributed imaging locations is 305 hours, which is approximately a 7.01% improvement over the trajectory shown in Figure 3.8.

3.2.3 Optimized MSE

The third imaging configuration that is considered in this chapter is the optimized MSE configuration developed in Chapter 2. Using those locations, both the minimum propellant and imaging time trajectories are determined. The following subsections present the results.

Mass Metric

Examples of minimum propellant trajectories using the optimized MSE imaging locations are shown in Figure 3.11. Similar to the results shown using the equivalent Cornwell imaging locations, the optimization tends to link imaging locations that are located at the same radial distance from the center. This observation is observed in the MSE-133 case and is even more clearly emphasized by the trajectories with higher numbers of imaging locations. The number shown in the title on top of each trajectory corresponds to the total number of u-v points in the trajectories. The minimum propellant trajectories using the optimized MSE imaging locations are shown in Appendix B.

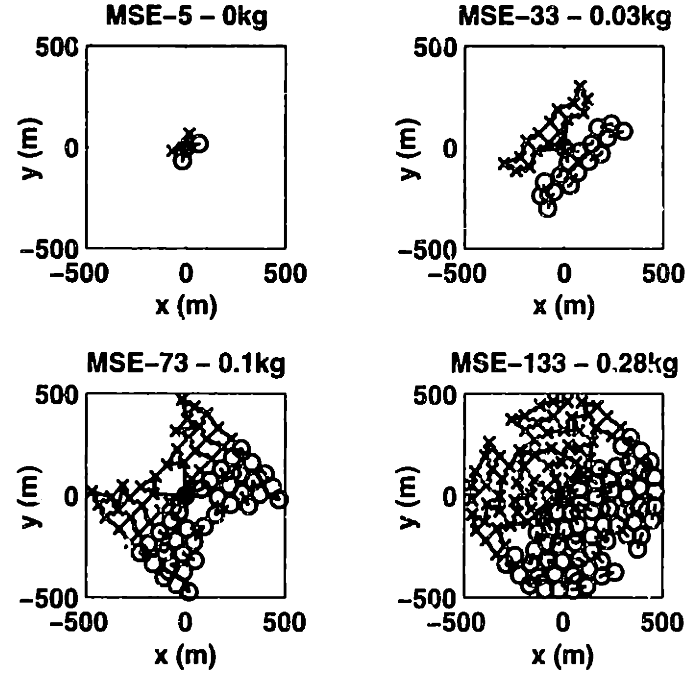

Figure 3.11 Examples of minimum propellant trajectories for a two collector interferometer using the optimized MSE imaging locations.

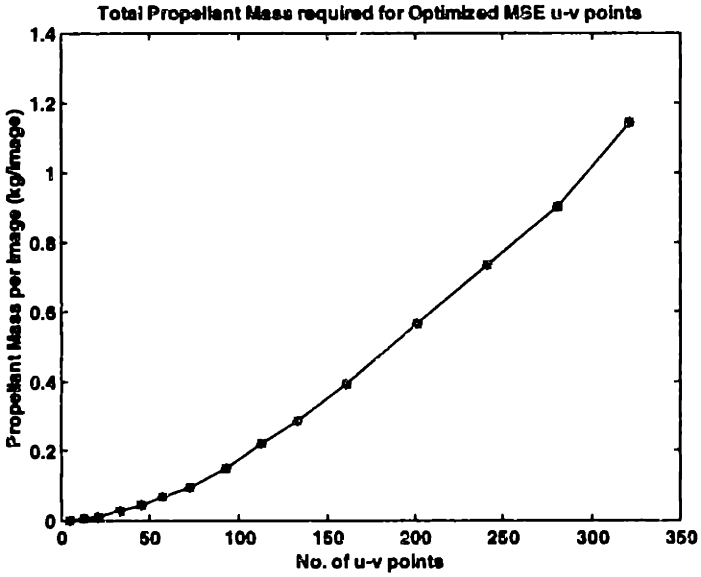

Figure 3.12 Total propellant mass required for the spacecraft to traverse through the optimized MSE imaging locations.

The propellant required for the spacecraft to complete the trajectories, plotted against the corresponding number of u-v points, is shown in Figure 3.12. Similar to the equivalent Cornwell imaging location results, the propellant requirement increases with the number of imaging locations.

Time Metric

Examples of minimum time trajectories using the optimized MSE imaging locations are shown in Figure 3.13. Similar to the trajectories shown using the equivalent Cornwell imaging locations, the optimization tends to link imaging locations that are closer to each other rather than linking imaging locations that are at the same radial distance from the center. This is mainly attributed to the cost involved in moving the combiner spacecraft in the mass optimization problem, which does not exist when using the time metric.

Plotting the time the that spacecraft require to complete the trajectories against the number of u-v points (Figure 3.14) shows that the maneuvering time increases with the number of u-v points, as expected.

Thus far, we have determined the resources required to obtain an image using three different configurations. In the next subsection, together with the results obtained in the previous chapter, we compare the interferometer performance using the different imaging configurations.

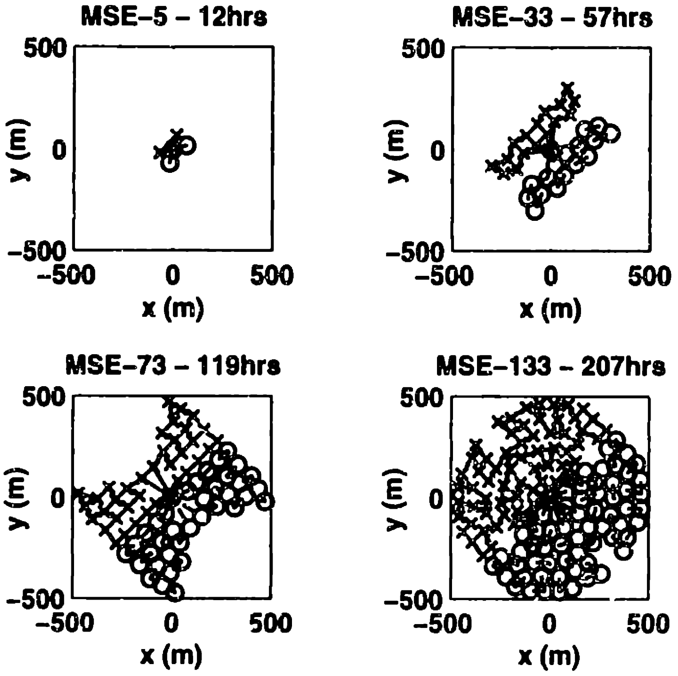

Figure 3.13 Examples of minimum time trajectories for a two collector interferometer using the optimized MSE imaging locations.

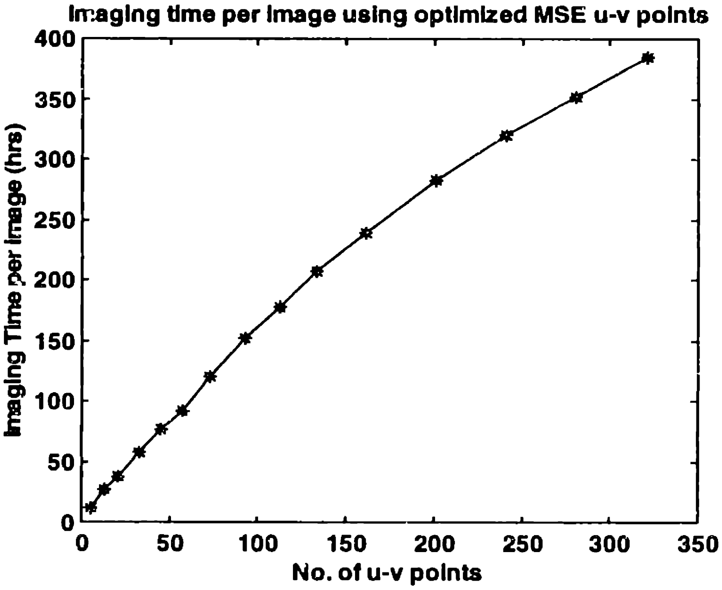

Figure 3.14 Imaging time per image for a two collector spacecraft interferometer using the optimized MSE imaging locations.

3.2.4 Comparisons

The performance of the different imaging configurations is compared in this subsection. However, rather than just comparing either the propellant usage or the time against the number of u-v points for the different imaging configurations, these performance metrics are plotted against their corresponding image quality obtained in Chapter 2. Using these plots, one can therefore clearly identify the best imaging configuration.

Mass Metric

The minimum propellant results, for the different imaging configurations obtained in this section, are plotted against the corresponding MSE results obtained in Chapter 2. This is shown in Figure 3.15 with the numbers attached to some data points indicating their corresponding number of unique u-v points. Since there exists only one datum point for the proposed DS3 imaging configuration, this configuration is defined as the nominal. The propellant requirement for the DS3 design is obtained from the optimal trajectory analysis discussed in Section 3.2.2. Imaging configurations that are located in the hatched region are the configurations that produce better image quality while requiring less propellant when compared to the DS3 imaging configuration. Hence, from the figure, even though the equivalent Cornwell imaging configurations require less propellant to image a particular object, the image quality obtained using this configuration is also worse than the image quality obtained using the DS3 imaging configuration. In fact, using the same

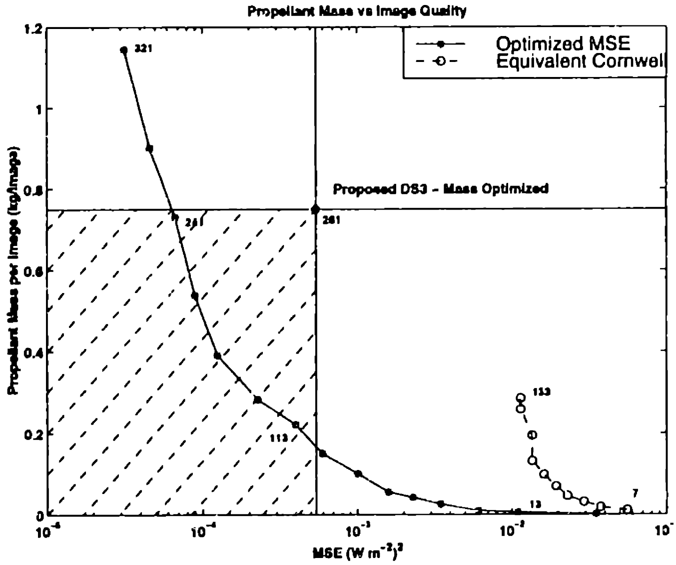

Figure 3.15 Propellant required to obtain the corresponding optimized image MSE.

number of imaging locations, the optimized MSE imaging configurations out perform the equivalent Cornwell imaging configurations in both propellant usage and also the obtainable image quality.

Comparing the optimized MSE configurations with the proposed DS3 configuration, the configurations that are located outside the hatched region perform better in either propellant usage or image quality but not both. Configurations that are located in the hatched region, however, perform better both in terms of propellant usage and image quality. Hence from Figure 3.15, one clearly sees that configurations which are located at the bottom left hand corner are in a 'win-win' situation. Some of the optimized MSE configurations are located in this corner.

Time Metric

Similarly, the imaging time per image for the different configurations can be plotted against the corresponding optimal image quality and is shown in Figure 3.16. Unlike Figure 3.15, there exist two imaging times for the proposed DS3 configuration: the imaging time obtained in Linfield, 1997, and the best imaging time using the re-distributed DS3 imaging locations. Hence, to show that the analysis made here is not biased, both values are included in the figure. Again, configurations that are located in the bottom left corner of the figure are configurations that produce better interferometric images in shorter periods of time. Since the optimized MSE configurations are

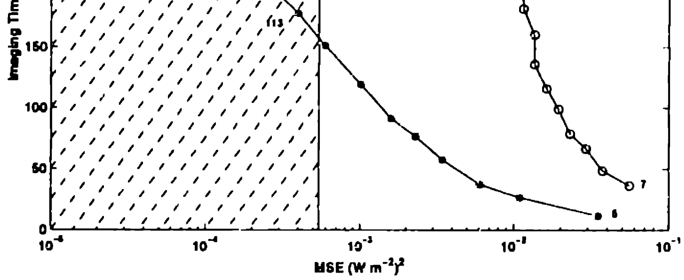

Figure 3.16 Minimum imaging time required to obtain the corresponding optimized image MSE.

clearly seen to be located in this corner, we can conclude that higher quality images can be obtained in shorter periods of time if these configurations are used.

Hence, in this section, we have determined the optimal imaging trajectories for a two collector and one combiner spacecraft using the different configurations. Even though sub-optimal, the optimized MSE configuration developed in this study was found to perform better in both the MSE and the trajectory metrics when compared with other configurations. This indicates that there are more optimal methods to image astronomical objects and the technique developed in this study brings us one step close to these optimal configurations.

3.3 Multiple Collector Interferometer

In the previous section, we determined the optimal trajectories based on the either the mass or time metric for a two collector and one combiner spacecraft. The basic trend is the increase in propellant usage as the number of imaging locations is increased. The results were based on the propellant required to image one object. If the number of objects is increased, the propellant requirement may eventually exceed the dry mass of the system. As an example, the propellant requirement for the two collector and one combiner spacecraft interferometer to image 498 images using the optimized imaging locations is shown in Figure 3.17.

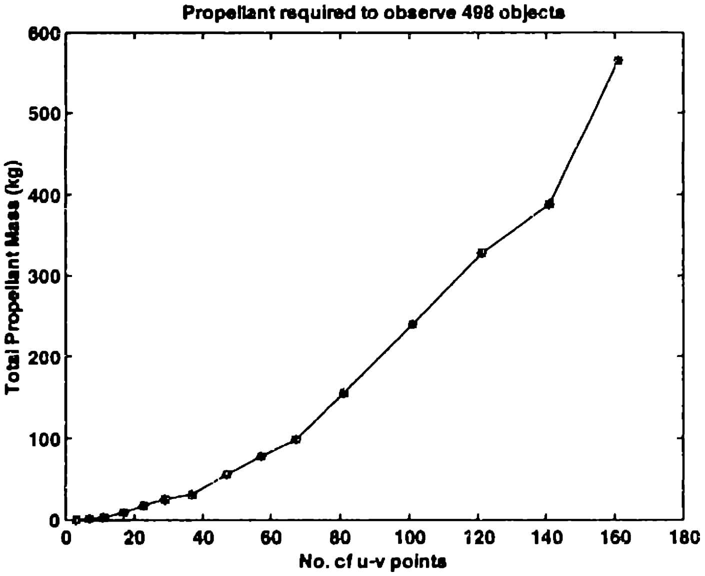

Figure 3.17 Propellant required for a two collector and one combiner interferometer to image 498 objects over 15 years.

The total dry mass of the three spacecraft system is 550 kg. Even though the propellant mass exceeds this 550 kg value for only the most detailed images, it is clear that a large amount of propellant is required to maneuver these spacecraft over 15 years. In almost any space mission, this type of propellant requirement is not feasible. Therefore, one must resort to alternative designs.

Rather than increasing the propellant mass of these spacecraft, it is also possible to increase the number of spacecraft in the system to fulfill the mission requirements. Hopefully, the addition of the extra spacecraft in the system will offset some of the propellant consumption since fewer maneuvers will be required to attain the same number of u-v point. In this section, the optimum number of collector spacecraft required to image 498 inter-stellar objects in 15 years using the Cornwell imaging locations is presented.

3.3.1 Cornwell Imaging Configuration

To illustrate the motivation behind adding more collector spacecraft to an interferometer, the Cornwell imaging locations are used, though other configurations could also be used. Using the mass metric in Section 3.1.1 to determine the propellant required to move the *N* spacecraft in the array, the total mass required to carry out the mission is determined.

The time metric is not considered as it does not present any interesting results. This is because increasing the number of collector spacecraft in the system will only reduce the total maneuvering time. The reduction in maneuvering time will eventually go down to zero when the number of collector spacecraft is either equal to or exceeds the number of imaging locations.

Mass Metric

Since the Cornwell imaging locations are located on a circle, the equal path length constraint from the collector spacecraft to the combiner spacecraft is met by placing the combiner spacecraft somewhere along the LOS of the array. Even though it is not possible to maintain an isosoles configuration during maneuvers, the spacecraft still preserve the isosoles configuration when they are located on the Cornwell imaging locations.

In order to obtain all the possible baseline separations that exist in a Cornwell imaging configuration, some of the *N* collector spacecraft must be re-oriented since the number of collector spacecraft is less than the number of imaging locations. The best maneuvering strategy for this *N* spacecraft interferometer is when only one collector spacecraft is allowed to re-orient at a time. Each time a spacecraft is re-oriented to a new imaging location, a maximum of 2(*N*-1) new u-v points is obtained. These u-v points are obtained at a cost of only two propellant burns (acceleration and deceleration) of a single spacecraft. However, if two spacecraft are allowed to re-orient instead, the maximum number of new u-v points that can be obtained is $2(N-1) + 2(N-2)$. This strategy, however, requires four propellant burns. Hence, when we compute the ratio between the number of new u-v points and the number of propellant burns, we see that the configuration which allows only one spacecraft to move at a time has a larger ratio of $(N-1)$ points per unit propellant burn as opposed to the $(N-3/2)$ ratio for the two spacecraft. Similarly, it can be shown that when M $(1 \leq M < N)$ spacecraft are re-oriented, the number of u-v points per unit propellant burn ratio that is achievable is $(N-(M+1)/2)$. Hence, for a given number of collector spacecraft (N), the best number of u-v points per unit propellant burn ratio is obtained when only one collector spacecraft $(M = 1)$ is allowed to re-orient at a time.

The optimal imaging sequence for an N collector spacecraft in a particular Cornwell configuration is determined using a Monte Carlo simulation. A total of 20,000 trials is used to determine the minimum propellant configuration given the constraint that an image must be obtained within 264 hours. The total propellant required is then multiplied by 498 (number of images in 15 years) and is added to the dry mass of the system. The dry mass of the system consists of the total mass of the collector spacecraft and the combiner spacecraft mass. Note that there is no propellant associated with the combiner spacecraft since a combiner spacecraft placed along the LOS of the array is already at an equal path length location from all the Cornwell imaging locations. The propellant required to reorient the entire array to image different parts of the sky is neglected in this study.

The total mass required to perform interferometric imaging using the different number of Cornwell locations is shown in Figure 3.18. For configurations that have greater than ten Cornwell points, there exist minimum total mass designs consisting of more than two collectors. To image the Cornwell-11 configuration, the optimal system mass occurs when three collector spacecraft are used. In the case of imaging the Cornwell-12 configuration, the optimal number of collector spacecraft is four. These minima represent the points at which increases in the dry mass of the system are equal to decreases in the propellant required to maneuver the collector spacecraft. In all other cases, the minimum system mass configuration occurs when only two collector spacecraft are used.

Hence, using the Cornwell imaging locations, we show that there exists an optimal number of collector spacecraft that should be used to image a particular Cornwell configuration over the lifetime of the mission. This feature is, however, not limited to only using the Cornwell imaging configu-

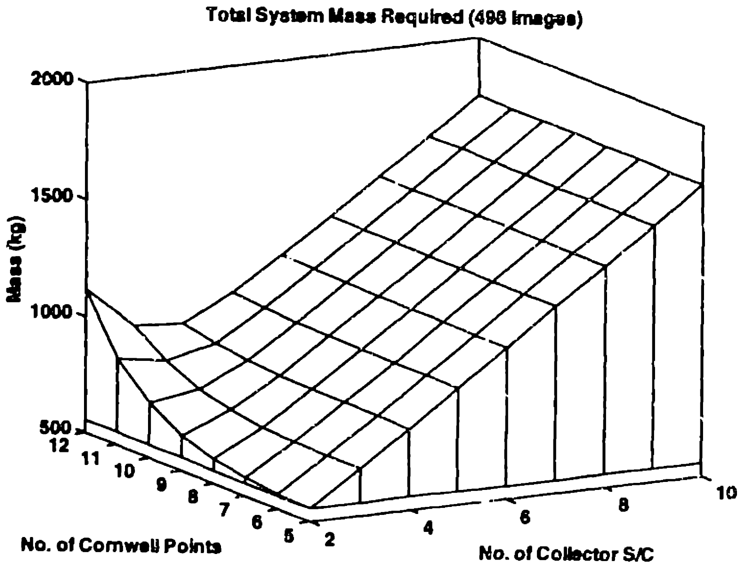

Figure 3.18 System mass required to image inter stellar objects using the different Cornwell imaging configurations.

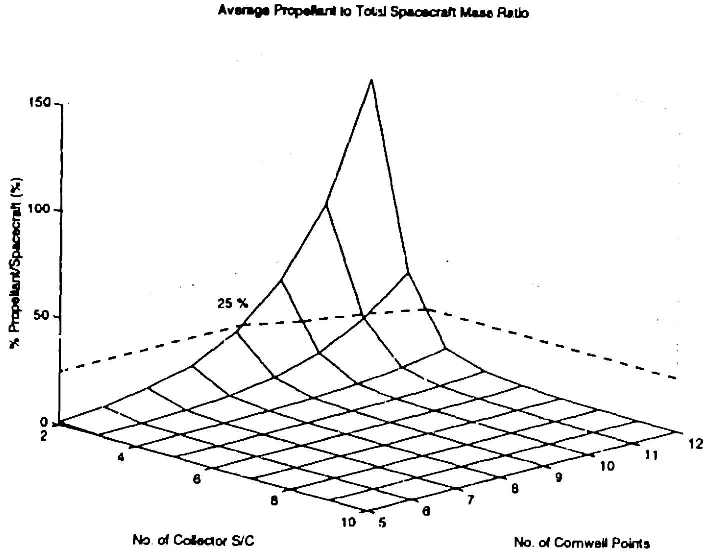

Figure 3.19 Average propellant to spacecraft mass ratio required to image 498 objects using the different Cornwell imaging configurations.

ration. Similar trades can be found whenever two competing options exist. The two competing options in this particular case are either adding more collector spacecraft to sample more u-v points per maneuver or increasing the propellant required to maneuver fewer collector spacecraft.

The existence of these minima is most pronounced when the propellant requirement exceeds the dry mass of a collector spacecraft.

Another issue that must be considered is the amount of on-board propellant that a spacecraft can carry. A plot of the propellant to total mass fraction per spacecraft is shown in Figure 3.19. Assuming that the maximum propellant to spacecraft mass ratio is set at 25%, the two collector spacecraft interferometer can only image up to the Cornwell-9 imaging configuration while the three collector system can be used for any configuration less than Cornwell-12. This would then change the optimum number of collector spacecraft that interferometer should use. Therefore, even though the optimum number of collector spacecraft can be determined based upon the total mass metric, issues such as the maximum propellant mass fraction must be considered. When a 25% constraint is imposed, the number of collector spacecraft required to image inter-stellar objects using the Cornwell-12 and Cornwell-10 configurations are four and three respectively, while other results remain the same as before.

3.4 Other Considerations

The analysis that was presented in this chapter considered only the 'Stop and Stare' imaging mode. The spacecraft are held stationary with respect to each other when the interferometric measurements are taken. There are, however, a number of issues that were not considered in this analysis that could be further investigated. The following presents some of these issues.

The two imaging modes that were considered in Linfield, 1997 are the 'Stop and Stare' mode and the 'Observe on the Fly' mode. In the latter mode, the three spacecraft are allowed to move relative to each other when the interferometric measurements are made, so long as the equilateral triangle configuration is maintained. As long as the spacecraft are travelling in a straight line (Figure 3.8), interferometric measurements can be taken on the fly. When the spacecraft reach the end of the line, they must then stop before accelerating again along a new direction. The spacecraft continue to do this until the image is completed.

In the case when the spacecraft are imaging in the 'Stop and Stare' mode, Linfield determined that the time required for the spacecraft to complete the trajectory is 264 hours. However, if the spacecraft are allowed to operate in the 'Observe on the Fly' mode, the amount of time required is only 104 hours. This represents a time savings of 60%!

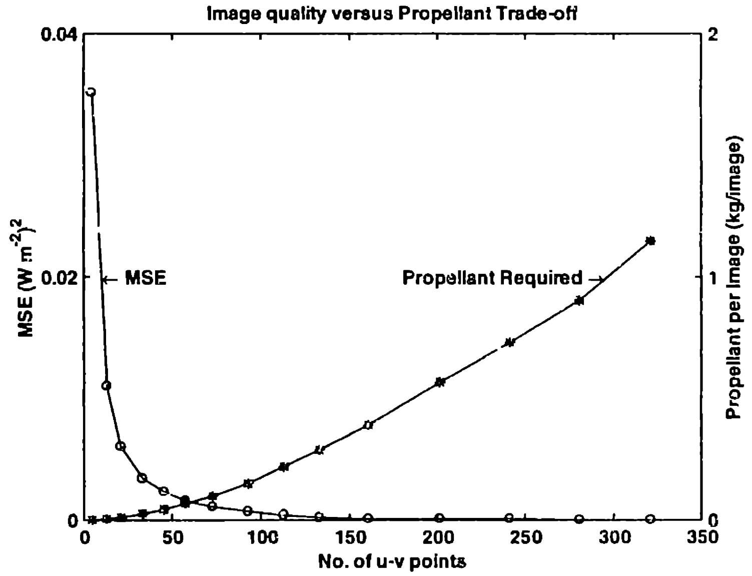

Figure 3.20 Image quality versus propellant requirement trade-off.

The advantage in allowing the spacecraft to 'Observe on the Fly' is not only limited to the spacecraft maneuvering time. In the case of the 'Stop and Stare' mode, the amount of total propellant required to maneuver the spacecraft using the trajectory shown in Figure 3.8 is 0.83 kg. In the 'Observe on the Fly' mode, only 0.14 kg is required, which represents a savings of 83%. Comparison with the optimal 'Stop and Stare' trajectory, which requires 0.75 kg, clearly shows the amount of propellant savings that the 'Observe on the Fly' mode provides.

Due to the significant savings using both the mass and time metrics, allowing the spacecraft to 'Observe on the Fly' must be investigated further. This can be done by changing the imaging trajectories for the collector spacecraft such that more imaging locations are located on the same line. However, since the imaging locations determined in Chapter 2 are optimal in terms of image quality, changing the imaging locations to save either the propellant or time will have a negative effect on the image quality. Hence, there exists a trade-off between the quality of image obtainable and the optimal trajectories obtainable. Figure 3.20 shows the trade-off between the image quality and the propellant required for the spacecraft to complete the trajectory.

The optimal trajectory determined in this chapter is based on the optimal imaging locations predetermined in Chapter 2. Depending upon the object that the interferometer is imaging, there exist different optimum imaging configurations. For example, if the object to be imaged happens to be an extended source, an interferometer with a small mainlobe is desirable. However, if the source turns out to be a collection of point sources, an interferometer with highly suppressed sidelobes is required. Unfortunately, since the concept behind the interferometer is to image objects that cannot be resolved by a single aperture, one cannot plan the imaging configurations apriori. It is possible, however, to allow the system to decide upon the interferometer's next imaging locations based upon the system's current state. The state of the system may be a function of time, the locations of the spacecraft, and also the interferometric measurements that have been taken. This possibility should be further investigated and could possibly be solved using what is known as the Partially Observable Markov Decision Processes [Cassandra et al, 1994].

3.5 Summary

In this chapter, the optimal trajectories for a two collector and one combiner spacecraft interferometer were determined. These optimal trajectories minimize the mass and time metrics introduced at the beginning of the chapter.

Based upon the mass estimates assumed for the DS3 mission, three different imaging configurations were compared. In each case, the resources required to obtain an image were found to increase with the number of imaging locations. Together with Chapter 2, imaging using the optimized MSE imaging configuration gives better images while requiring less resources.

Unfortunately, there exist cases where the propellant requirement is too prohibitively large for the individual spacecraft. In these cases, the propellant requirement can be reduced by introducing more spacecraft to reduce the amount of maneuvering required. This possibility is explored for a multiple collector spacecraft interferometer covering different numbers of Cornwell imaging configurations. In most cases, the optimum number of collector spacecraft required was found to be only two. However, in the case of using the Cornwell-12, Cornwell-11 and Cornwell-10 configurations, the optimum number of collector spacecraft required are four, three and three respectively. These results were based upon the total system mass and the constraint on the amount of on-board propellant that an individual spacecraft can carry.

The results obtained in this chapter are specifically for an interferometer that operates in a 'Stop and Stare' imaging mode. Even though not examined in this chapter, the advantages of allowing the spacecraft to operate in an 'Observe on the Fly' mode is discussed based on previous work. Up to 83% savings in propellant mass can be achieved if the spacecraft are allowed to image on the fly. In order to determine the optimal 'Observe on the Fly' trajectories using the optimized MSE imaging locations, a trade-off between better image quality and the two trajectory metrics should be made as reducing either the propellant or maneuvering time for the spacecraft by choosing a different set of the imaging locations, will reduce the quality of the interferometric image. This trade-off, even though not explored in this analysis, is briefly discussed and is a subject for future consideration.

Hence, in this chapter, we determined the optimal trajectories for a two collector and one combiner interferometer operating outside a gravity-well. The optimal configuration for a multiple spacecraft interferometer was also determined. In the next section, the orbit design for a separated spacecraft Earth imager operating within the Earth's gravity-well is discussed.

Chapter 4

EARTH IMAGING FROM WITHIN EARTH'S GRAVITY- WELL

Besides imaging interstellar objects, an interferometer can be used to obtain high resolution images of Earth. Programs such as the Air Force Ultralite system [Powers et al, 1997] and Techsat21 program [Sedwick et al, 1998], which consist of multiple apertures, have been proposed for Earth imaging or target detection using interferometric techniques. The dynamics of these spacecraft, however, are directly influenced by the Earth's gravitational tidal forces. Taking full advantage of this, the optimal orbit design for a separated spacecraft Earth imager using interferometric techniques is determined in this chapter.

Space interferometers can be divided into two main architectures depending on the distribution of the apertures. The first architecture is known as a structurally connected interferometer (SCI), where all the apertures are placed on the same platform. Studies by Surka et al, 1996 and Stephenson et al, 1998 indicate that a SCI architecture should be used if the resolution of the interferometer can be adequately satisfied with short aperture separations. However, when large aperture separations are required, these apertures must be placed on separate platforms. These spacecraft are grouped under the separated spacecraft interferometer (SSI) architecture. In general, the apertures in a SCI always remain fixed relative each other, even if the structure is in constant motion. This, however, is not true for a SSI.

In order to take interferometric measurements, the apertures must be placed in some formation. For an interferometer located in Earth orbit, this can be done by expending propellant to hold the spacecraft in a fixed formation to overcome the Earth's gravitational tidal forces [Yashko, 1998]. Alternatively, these tidal forces can be exploited to naturally allow the spacecraft to move such that the apertures remain fixed relative to each other. In doing so, the propellant expenditure for the spacecraft can be reduced, which in turn reduces the possibility of contaminating the interferometer optics.

As opposed to imaging astronomical objects, terrestrial targets tend to change more rapidly. The imaging of these rapidly changing targets is made possible with a Fizeau interferometer. The Fizeau interferometer, however, requires a full instantaneous u-v coverage, as was discussed in Chapter 2. Since it is not possible to obtain any advance information about the target, it does not make sense to tailor the interferometer's u-v coverage to anything but equal coverage in all angular directions. In the case of imaging in the visible range, a stricter requirement that must be met by the system is to interfere the science light in real time. This translates to having equal science light pathlength from the target to the combiner via each collector. Therefore, the requirements that must be met by an optical interferometer system are:

- Equal coverage in both u and v directions (Fourier Plane);
- Equal science light pathlength for real time imaging (required for visible wavelength).

Keeping these requirements in mind, is it then possible to obtain minimum propellant imaging configurations for these spacecraft and still meet the interferometric requirements? The objective of this chapter is to determine these optimum imaging configurations. The framework in which the analysis is performed is presented in the next section. This is followed by a validation of the assumptions by comparing the different perturbations that effect a spacecraft in an Earth orbit. The two sections which follow look at two different imaging configurations, one which involves an innovative exploitation of the properties of a circular paraboloid to meet the interferometric requirements. A case study using the two imaging configurations in a geosynchronous orbit to image terrestrial targets is presented in Section 4.5. The findings in this chapter are finally summarized in Section 4.7. The orbit design for a radio interferometer is not determined as it has been addressed in Mallory et al, 1998.

4.1 Hill's Equations and ΔV Derivation

In this section, we present the framework in which the analysis is being carried out. Once the framework is presented, the metric by which we compare the different imaging configurations is derived. This metric, known as ΔV, is a measure of how much velocity change is required and can be used to determine the propellant requirements.

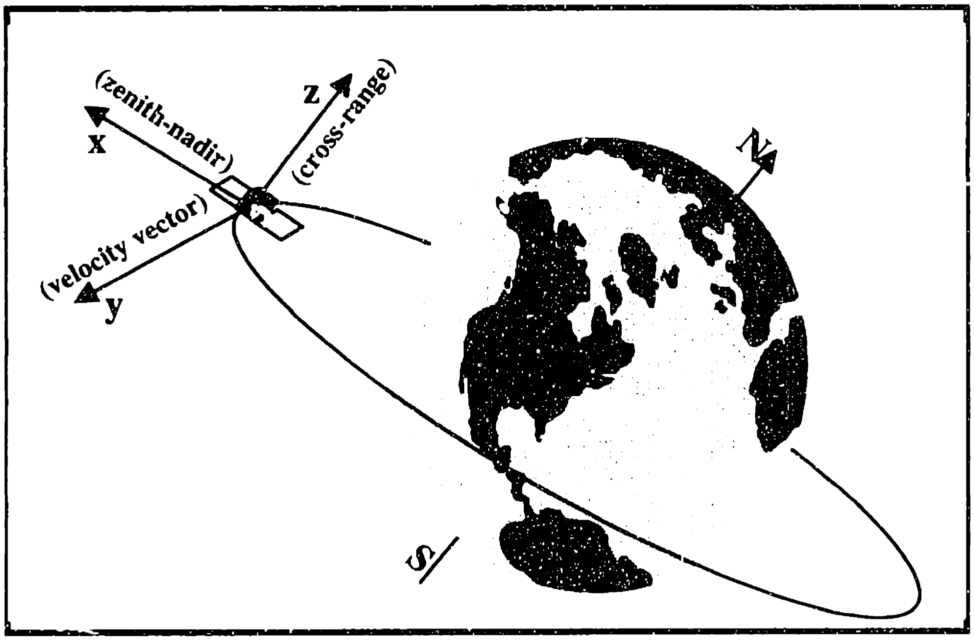

Figure 4.1 Hill's coordinate frame shown with respect to Earth.

Since the size of the array is relatively small compared to the size of its orbit, the dynamics of the spacecraft can be adequately captured by assuming a perfectly spherical Earth and linearizing the dynamics about the motion of the center of the array. This linearization is often referred as Hill's frame [Hill, 1978]. The Hill's equations govern the relative motion between two spacecraft for which one is travelling in a circular Keplerian orbit while the second is perturbed from this orbit. These equations with their three dimensional accelerations are given by:

$$\begin{aligned} a_x &= \ddot{x} - 3n^2 x - 2n\dot{y} \\ a_y &= \ddot{y} + 2n\dot{x} \\ a_z &= \ddot{z} + n^2 z \end{aligned} \tag{4.1}$$

where n is the orbital frequency, which is related to the orbital period (P) as $2\pi/P$, and a_x, a_y and a_z are the accelerations of the spacecraft in the respective directions. The x-variable in the equation is the displacement along the zenith-nadir line, the y-variable corresponds to the displacement along the orbital velocity vector, and the z-variable corresponds to the cross axis displacement left and right of the local velocity vector. However, the orbit need not be equatorial and notice that this is an accelerating frame (Figure 4.1).

The different imaging configurations can be compared in terms of the total system mass required for each system. To do so, the change in velocity (ΔV) required to keep the spacecraft in certain configurations is calculated. Using the acceleration terms from equation 4.1, the total ΔV for the spacecraft over a lifetime of T_{life} is

$$\Delta V = \int_0^{T_{life}} \sqrt{a_x^2 + a_y^2 + a_z^2} dt \tag{4.2}$$

Given the dry mass of the spacecraft and equation 4.2, the propellant mass to spacecraft dry mass ratio can be calculated using the rocket equation:

$$\frac{m_p}{m_d} = \exp\left(\frac{\Delta V}{I_{sp}g}\right) - 1 \tag{4.3}$$

where I_{sp} is the propulsion system's specific impulse measured in seconds and g is Earth's gravity measured in ms^{-2}. Only the propellant required to maneuver the spacecraft is of interest in this analysis. This is because the propellant associated with rotating the spacecraft is assumed to be small in comparison. Orbital insertion and de-orbit propellant consumption can be large but is well known and therefore outside of this analysis.

In this analysis, the propellant requirement for an interferometer to image any terrestrial targets located within its horizon's limit is presented. There are four different configurations in which these targets can be imaged, of which only three are studied in this work. The four different configurations are:

Forced Circular [Section 4.3]
In this configuration, all the collector spacecraft are forced to follow a circular trajectory about the combiner spacecraft. Spacecraft in this trajectory do not require any optical delay lines such that the same wavefront from the target can be interfered at the combiner spacecraft. Terrestrial targets that are located at different locations on the Earth's surface are imaged by slewing the entire array.

Forced Elliptical Trajectories [Section 4.4.4]
In this imaging configuration, all the collector spacecraft follows an elliptical trajectory which projects a circle onto the plane perpendicular to the array's line of sight (LOS). The elliptical trajectory is chosen such that when the LOS is pointed at nadir, no propellant is expended by the collector spacecraft. The combiner spacecraft, however, requires propellant to hold its position such that no delay lines are required to combine light reflected off the collector spacecraft. Off-nadir targets are imaged by slewing the entire array as in the forced circular configuration.

Combiner Relocation with Optical Delay Lines [Section 4.4.5]
This imaging configuration is essentially the same as the previous configuration. However, when off-nadir targets are to be imaged, only the combiner spacecraft is

required to be reoriented. Optical delay lines are required to allow the same wavefront to be combined at the combiner spacecraft.

Free Elliptical Trajectories
Later in this chapter, it is determined that no propellant expenditure is necessary when a spacecraft follows trajectories which project two-by-one ellipses onto the x-y plane in the Hill's frame. The free elliptical orbit in the last two configurations do in fact project a two-by-one ellipse onto the x-y plane, when an on-nadir target is imaged. There exist a number of these trajectories where propellant is not required to hold the spacecraft in their orbits. However, these free trajectories only exist for imaging terrestrial targets that are located on the x-z plane only. Since it is not possible to image all possible terrestrial targets within the interferometer's horizon-to-horizon limit, this option is not considered in this study. This particular option is discussed in more detail in Section 4.6.

The first three different configurations are studied in more detail in the next few sections. In order to get some numerical feel of the propellant requirements for these configurations, a case study involving these configurations located in a geosynchronous orbit is presented in Section 4.5. In the next section, other perturbations that affect the dynamics of a spacecraft in an Earth orbit are discussed. These effects are compared with the perfectly spherical Earth assumption made in the derivation of the Hill's equations.

4.2 Orbit Perturbations

The derivation of the linearized Hill's equations assumes a perfectly spherical Earth. However, the Earth is not spherical and there exist other disturbances in Earth orbit that must be considered. The orbit perturbations that are considered in this analysis are the Earth's non-spherical effect, third body perturbations from either the Moon or the Sun, solar radiation pressure and atmospheric drag. The emphasis in this section is to categorize the effects of these disturbances with respect to the linearized dynamics given by the Hill's equations. While perturbations which move the array are of little concern, pertubations which cause the array to deform, drift apart or compress are of critical concern.

4.2.1 Non-Spherical Effect

The first disturbance discussed is the effect on the dynamics of spacecraft due to the non-uniformity of the Earth's mass. The largest perturbation due to this effect is the J_2 component in the Earth's geo-potential function [Larson et al, 1992] given by:

$$\Phi = \left(\frac{\mu}{R}\right)[1 - J_2(R_E/R)^2 P_2(\sin\theta)] \tag{4.4}$$

where μ is the Earth's gravitational constant, R_E is the Earth's equatorial radius, P_2 is the second Legendre polynomial, R is the radius of the orbit of interest, θ is the geocentric latitude of the orbit and J_2 is a dimensionless geo-potential of 0.00108263. Since the Legendre polynomial $P_2(x)$ can be rewritten as $\frac{1}{2}(3x^2 - 1)$ [Kreyszig,1988], the acceleration experienced by a spacecraft in an orbit R is therefore:

$$\begin{aligned} a_z &= \frac{1}{R}\frac{\partial\Phi}{\partial\theta} \\ &= -\frac{3\mu J_2 R_E^2}{2R^4}\sin 2\theta \end{aligned} \tag{4.5}$$

Substituting the respective values into equation 4.5 ($R_E = 6{,}378$ km, $\theta = 45^\circ$, $\mu = 3.99 \times 10^{14}$ m^{3}s^{-2}), the maximum possible acceleration imposed on a spacecraft in Low Earth Orbit (LEO) (R = 7,378 km) is 8.9×10^{-3} ms^{-2} and 8.3×10^{-6} ms^{-2} in Geostationary Earth Orbit (GEO) (R = 42,164 km). Even though the latitude at GEO is 0°, the maximum acceleration is quoted for comparison purposes.

The differential acceleration experienced by two spacecraft that are separated by a distance of Δz is given by

$$\begin{aligned} \Delta a_z &= \left|\frac{1}{R}\frac{\partial a_z}{\partial\theta}\right|\Delta z \\ &= \frac{3\mu J_2 R_E^2}{R^5}\cos 2\theta\Delta z \end{aligned} \tag{4.6}$$

Evaluating the expression, the maximum differential acceleration experienced by two spacecraft in LEO separated by a distance of 1000 m is 2.4×10^{-6} ms^{-2}. Similarly, these two spacecraft will experience a differential acceleration of 4.0×10^{-10} ms^{-2} if they are located in GEO.

4.2.2 Third body perturbations

Two major sources of third body perturbations on a spacecraft in an Earth orbit are the Moon and the Sun [Abell et al, 1987]. Given that the mass of the Moon is approximately 7.4×10^{19} tons and approximately 384,404 km away from Earth's center, the gravitation experienced by a spacecraft in LEO is $a_{Moon} \approx 3.6 \times 10^{-5}$ ms^{-2}, while in GEO, it is $a_{Moon} \approx 4.3 \times 10^{-5}$. The differential accelerations, however, are $\Delta a_{Moon} \approx 1.9 \times 10^{-10}$ ms^{-2} and $\Delta a_{Moon} \approx 1.8 \times 10^{-10}$ ms^{-2}, respectively.

Repeating these calculations for perturbations due to the Sun, the gravitational pull experienced by a spacecraft in Earth's orbit is $a_{Sun} \approx 5.9 \times 10^{-3}$ ms^{-2}. The differential acceleration, however, is calculated to be $\Delta a_{Sun} \approx 7.9 \times 10^{-11}$ ms^{-2}. Note that these values are valid for both LEO and GEO because of the insignificant orbit difference compared with the Sun-Earth distance. The Sun's mass is 1.989×10^{27} tons with a mean distance of 1.496×10^{8} km away from Earth.

4.2.3 Solar Radiation Pressure

The effect of solar radiation pressure on a spacecraft in Earth orbit is dependent upon the cross-sectional area that is exposed to the sun. The magnitude of acceleration due to solar radiation pressure as a function of the cross sectional area (A) and the mass of the spacecraft (m) is [Larson et al, 1992]:

$$a_r \approx 4.5 \times 10^{-8}\frac{A}{m} \tag{4.7}$$

Assuming a collector spacecraft mass of 150 kg with a solar array panel of 1.4 m^2, the effect of solar radiation on the spacecraft acceleration is approximately $a_r \approx 4.2 \times 10^{-10}$ ms^{-2}. Assuming that the mass of the combiner spacecraft is 250 kg with the same solar array size, the differential acceleration experienced by these two spacecraft is $\Delta a_r \approx 1.7 \times 10^{-10}$ ms^{-2}.

4.2.4 Atmospheric Drag

Atmospheric drag is the principal non-gravitational force acting on satellites in low-Earth orbit (LEO). The equation for acceleration due to atmospheric drag on a spacecraft is given by [Larson et al, 1992]:

$$a_D = \frac{1}{2}\rho\frac{C_D A}{m}V^2 \tag{4.8}$$

where ρ (kgm^{-3}) is the atmospheric density, C_D is the coefficient of drag which is approximately 2.2 [Larson et al, 1992], A (m^2) is the spacecraft cross-sectional area, m (kg) is the mass of the spacecraft and V (ms^{-1}) is the relative velocity between the spacecraft and the atmosphere. The densities of the atmosphere at LEO (~ 1000 km) and at GEO are 1.43×10^{-14} kgm^{-3} and 5.12×10^{-19} kgm^{-3}, while the velocities of a spacecraft in circular orbits at these altitudes are 7.35 kms^{-1} and 3.075 kms^{-1}. Hence, using these values, the atmospheric accelerations experienced by a spacecraft in these orbits are $a_D = 7.9 \times 10^{-9}$ ms^{-2} and $a_D = 5.0 \times 10^{-14}$ ms^{-2}, respectively. However, the differential accelerations experienced by a collector spacecraft with respect to a combiner spacecraft are $\Delta a_D = 3.2 \times 10^{-9}$ ms^{-2} and $\Delta a_D = 2.0 \times 10^{-14}$ ms^{-2}, respectively.

4.2.5 Comparisons

The gravity acting on a spacecraft in Earth's orbit at a distance R from the Earth's center is given by:

$$a_E = \frac{GM_{earth}}{R^2} \tag{4.9}$$

Hence, the Earth's gravitational pull for a spacecraft in LEO is 7.32 ms^{-2} and 0.22 ms^{-2} at GEO. The differential gravitational pull experienced by spacecraft that are separated by a distance of 1000m in altitude are $\Delta a_E = 2.0 \times 10^{-3}$ ms^{-2} and $\Delta a_E = 1.6 \times 10^{-5}$ ms^{-2}, respectively.

The magnitude of the different orbital effects are summarized in Table 4.1. Comparisons of the different sources of orbit perturbations show that the two largest perturbations that are experienced by a spacecraft in LEO are the J_2 and atmospheric drag. However, these values are three orders of magnitude smaller than the gravitational pull exerted by a perfect Earth. In GEO, the solar radia-

TABLE 4.1 Comparisons of the various orbit perturbations.

	LEO (1000 km) (ms^{-2})		**GEO (35786 km) (ms^{-2})**	
Perturbations	**Absolute**	**Differential**	**Absolute**	**Differential**
Non-spherical effect	8.9×10^{-3}	2.4×10^{-6}	8.3×10^{-6}	4.0×10^{-10}
Moon's gravity	3.6×10^{-5}	1.9×10^{-10}	4.3×10^{-5}	2.6×10^{-10}
Sun's gravity	5.9×10^{-3}	7.9×10^{-11}	5.9×10^{-3}	7.9×10^{-11}
Solar Pressure	4.2×10^{-10}	1.7×10^{-10}	4.2×10^{-10}	1.7×10^{-10}
Atmospheric Drag	7.9×10^{-9}	3.2×10^{-9}	5.0×10^{-14}	2.0×10^{-14}
Earth's gravity	7.32	2.0×10^{-3}	2.2×10^{-1}	1.6×10^{-5}

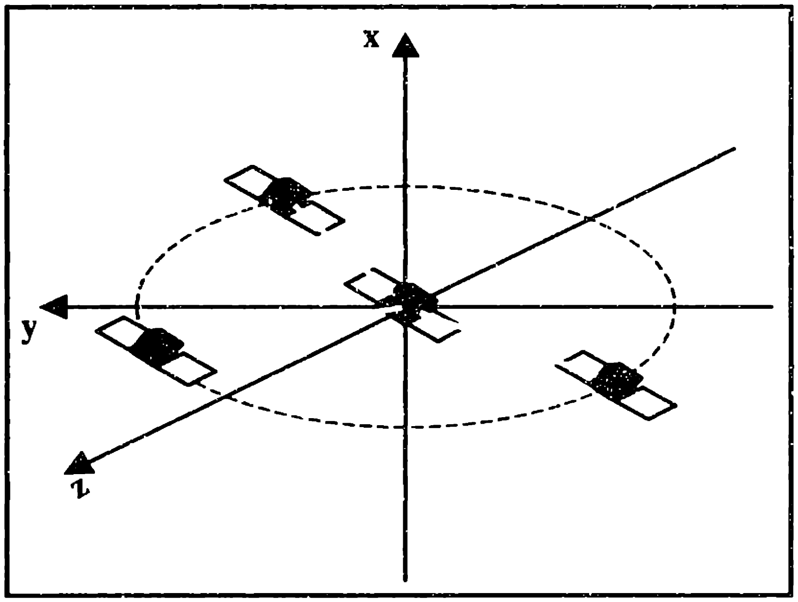

Figure 4.2 Collector Spacecraft in forced circular trajectory about a combiner spacecraft

tion has a larger percentage effect on the spacecraft but is still small compared with the Earth's gravitational pull. These results then indicate that the dynamics of a spacecraft in Earth orbit can be adequately captured by assuming a perfectly spherical Earth.

4.3 Circular Trajectories

First consider a system that is imaging a target in the nadir direction. In order to meet both interferometric requirements, one possible solution is to constrain the trajectory of the collector spacecraft to a circle that lies in the Hill's y-z plane (notice that this local horizontal plane rotates 360° in one orbit) with the combiner spacecraft located at the center of the circle in a natural Keplerian orbit. Collector spacecraft rotating about a central combiner provide equal coverage in both u and v directions while maintaining equal pathlength from the ground through each collector to the combiner. This design is essentially the Forced Circular configuration described in Section 4.1 and is shown in Figure 4.2.

4.3.1 Combiner Spacecraft Maintaining a Fixed Position

The ΔV required to maintain a spacecraft at a fixed location is determined in this subsection. For a spacecraft fixed in the Hill coordinate frame, both the velocity and acceleration terms in equation

4.1 are equal to zero. This then leaves the applied acceleration required to maintain a spacecraft in a fixed position:

$$\begin{aligned} a_x &= -3n^2x \\ a_y &= 0 \\ a_z &= n^2z \end{aligned} \tag{4.10}$$

The ΔV required for this spacecraft, calculated using equation 4.2 is then

$$\Delta V = n^2\sqrt{9x^2+z^2}T_{life} \tag{4.11}$$

Equation 4.11 indicates that more propellant is required to maintain a spacecraft in the x-direction as opposed to holding it in the z-direction. This makes sense, as holding a spacecraft in the x-direction is essentially putting a spacecraft at a higher altitude orbit but requiring it to have an orbital period of a lower altitude orbit. In the case of holding the spacecraft in the z-direction, the spacecraft is essentially in the same altitude orbit but is inclined. Spacecraft held in the y-direction require no propellant at all, since they are on the same circular orbit as the one located at the origin of the Hill coordinate frame. Also, ΔV increases as orbital altitude increases or orbital altitude decreases.

Therefore, in the case of forcing the collector spacecraft to rotate in a circular trajectory, the obvious location to put the combiner spacecraft is somewhere along the y-axis. However, to simplify later analysis, the combiner spacecraft is placed at the origin, which requires no velocity change at all to maintain its position.

4.3.2 Zero Zenith-Nadir Motion

In the previous subsection, we determined that placing a combiner spacecraft at the Hill's origin requires no velocity change. How about the collector spacecraft? In this subsection, we determine the ΔV for the collectors following a circular trajectory about the combiner. First, an imaging configuration with a line of sight (LOS) that is parallel to the x-axis is determined. In the next subsection, this LOS is varied so that different areas of the Earth can be imaged.

In the case of the circular imaging configuration, the LOS of the array is perpendicular to the plane in which the collector spacecraft trace out circular trajectories. Therefore, for an imaging configuration with an LOS that is parallel to the x-axis, the collector spacecraft are then constrained to be

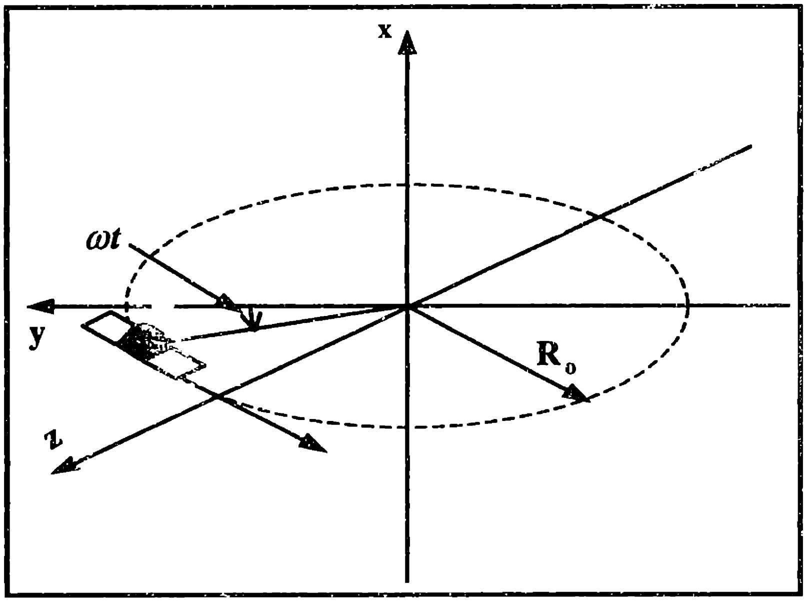

Figure 4.3 Spacecraft rotating about a circle of radius R_0 at an angular velocity of ω.

in the y-z plane. Specifying ω as the rotational speed of the collector spacecraft about a circle of radius R_o, the motion of a spacecraft is therefore

$$\begin{aligned} x &= 0 \\ y &= R_o\sin(\omega t+\alpha) \\ z &= R_o\cos(\omega t+\alpha) \end{aligned} \tag{4.12}$$

The positive sign of ω in equation 4.12 corresponds to a spacecraft traveling in a clockwise direction when seen from the positive x-axis direction. This is more clearly depicted in Figure 4.3. The variable α corresponds to the phase of the spacecraft in the orbit and for simplicity, a value of zero is assigned to it.

In this analysis, we let ω to be equal to n, the orbital frequency. This is done because the minimum propellant rotational frequency for a spacecraft can be shown to be equal to the rotational frequency of the orbit of interest and is shown in Section 4.4. Therefore, to compare the results from the different imaging configurations, the orbital frequency in this section is taken to be its natural orbital frequency. Using $\omega = n$, the acceleration required to keep a spacecraft in its circular trajectory is therefore

$$\begin{aligned} a_x &= -2n^2 R_o \cos nt \\ a_y &= -n^2 R_o \sin nt \\ a_z &= 0 \end{aligned} \tag{4.13}$$

Substituting equation 4.13 into equation 4.2, the ΔV required to keep a spacecraft in a circular trajectory for a lifetime of T_{life} is

$$\Delta V = n^2 R_o \int_0^{T_{life}} \sqrt{(-2\cos nt)^2 + (-\sin nt)^2}\, dt \tag{4.14}$$

Rewriting equation 4.14 in terms of sines and evaluating the integral over a period of 2π, the ΔV in equation 4.14 can be rewritten as

$$\begin{aligned} \Delta V &= \frac{n^3 R_o T_{life}}{2\pi} \int_0^{\frac{2\pi}{n}} \sqrt{(2\cos nt)^2 + (\sin nt)^2}\, dt \\ &= \frac{4n^3 R_o T_{life}}{\pi} \int_0^{\frac{\pi}{2n}} \sqrt{1 - \frac{3}{4}(\sin nt)^2}\, dt \end{aligned} \tag{4.15}$$

Recognizing that equation 4.15 is in the form of an elliptical integral, replacing the variable nt with θ and performing the integration over a quarter of the ellipse, equation 4.15 becomes

$$\Delta V = \frac{4n^2 R_o T_{life}}{\pi} \int_0^{\frac{\pi}{2}} \sqrt{1 - \frac{3}{4}(\sin\theta)^2}\, d\theta \tag{4.16}$$

which is in the form of a complete elliptic integral of the second kind with argument parameter of m [Abramowitz et al, 1972]. The elliptic integral with an argument parameter of $m = 3/4$ is

$$\begin{aligned} E\left(m = \frac{3}{4}\right) &= \int_0^{\frac{\pi}{2}} \sqrt{1 - \frac{3}{4}(\sin\theta)^2}\, d\theta \\ &= 1.211056 \end{aligned} \tag{4.17}$$

Finally, the ΔV required to maintain a spacecraft in a circular trajectory over a lifetime of T_{life} is

$$\begin{aligned} \Delta V &= \frac{4n^2 R_o T_{life}}{\pi} \times 1.211 \\ &= 1.542 n^2 R_o T_{life} \end{aligned} \tag{4.18}$$

which is considered to be a relatively high ΔV as will be shown in later comparisons.

4.3.3 Change of Line of Sight (LOS)

Thus far, only an on-nadir target has been considered. In this subsection, the ΔV required to maintain a spacecraft in a circular orbit which has an LOS that is not parallel to the *x*-axis in the Hill's frame is determined. This allows the calculation of how much propellant is required to image an object that is located at different Earth longitudes.

The LOS vector of a circular array is a vector that is perpendicular to the plane which contains the spacecraft. Hence, for each plane array, there exist two possible LOS vectors, directly opposite in direction to each other. To distinguish between these LOS, two vectors in opposing directions, LOS1 and LOS2, are introduced. The LOS1 vector is defined as the LOS which corresponds to the positive direction in which the spacecraft are rotating using the left hand convention. These vectors are shown in Figure 4.4.

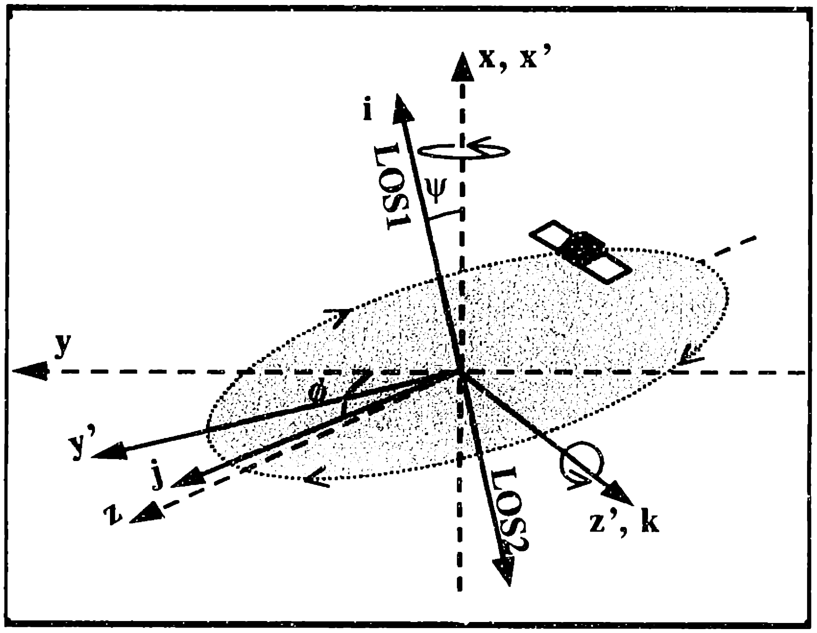

Figure 4.4 Varying LOS by rotating array through angles ϕ and ψ.

To change the LOS of the array, a 3-dimensional (ijk) coordinate frame is specified and attached to the LOS1 vector such that the positive direction of the LOS1 vector is in the same direction as the positive i-axis. The coordinate system is spherical, with the positive x-axis pointing at the north pole. The angle ϕ is the longitude measured from the positive y-axis, and ψ is the co-latitude, measured from the positive x-axis. The new ijk coordinate frame can be rotated by an angle ϕ about the x-axis (azimuth) and then rotated by an angle ψ about the new j-axis (declination) so that the direction of the LOS1 vector can be specified in terms of these two rotational angles. These rotation angles and the new coordinate frame (ijk) with respect to the Hill coordinate frame (xyz) are shown in Figure 4.4.

Specifying x', y', z' as the new coordinate frame after a rotation of ϕ about the x-axis, the relationship between this new coordinate frame and the Hill coordinate frame is

$$\begin{bmatrix} x \\ y \\ z \end{bmatrix} = \begin{bmatrix} 1 & 0 & 0 \\ 0 & \cos\phi & -\sin\phi \\ 0 & \sin\phi & \cos\phi \end{bmatrix} \begin{bmatrix} x' \\ y' \\ z' \end{bmatrix} \tag{4.19}$$

Rotating this new x', y', z' coordinate frame about the z'-axis through an angle ψ gives a rotation matrix between i, j, k and x', y', z'

$$\begin{bmatrix} x' \\ y' \\ z' \end{bmatrix} = \begin{bmatrix} \cos\psi & -\sin\psi & 0 \\ \sin\psi & \cos\psi & 0 \\ 0 & 0 & 1 \end{bmatrix} \begin{bmatrix} i \\ j \\ k \end{bmatrix} \tag{4.20}$$

Therefore, combining equations 4.19 and 4.20, the relationship between the new coordinate frame i, j, k and the Hill coordinate frame can be obtained. Since a collector spacecraft follows a circular trajectory in the plane that is perpendicular to the LOS1 vector, the collector spacecraft motion can be written as:

$$\begin{aligned} i &= 0 \\ j &= R_o \sin nt \\ k &= R_o \cos nt \end{aligned} \tag{4.21}$$

The circular frequency of the spacecraft is taken to be n such that comparison with later results can be made. Therefore, in the Hill coordinate frame, the circular motion of a spacecraft in the i, j, k frame is:

$$\begin{bmatrix} x \\ y \\ z \end{bmatrix} = R_o \begin{bmatrix} \cos\psi & -\sin\psi & 0 \\ \cos\phi\sin\psi & \cos\phi\cos\psi & -\sin\phi \\ \sin\phi\sin\psi & \sin\phi\cos\psi & \cos\phi \end{bmatrix} \begin{bmatrix} 0 \\ \sin nt \\ \cos nt \end{bmatrix} \tag{4.22}$$

Taking the first and second derivative of equation 4.22 and substituting these expressions into equations 4.1 and 4.2, the ΔV required to maintain a spacecraft in a circular trajectory with the LOS1 vector pointed in the (ϕ,ψ) direction can be determined. Replacing nt with θ, the ΔV expression as a function of θ can be rewritten:

$$\Delta V = \frac{n^2 R_o T_{life}}{2\pi} \int_0^{2\pi} \sqrt{f_x^2(\theta) + f_y^2(\theta) + f_z^2(\theta)}\, d\theta \tag{4.23}$$

where $f_{xyz}(\theta) = a_{xyz}(\theta)/R_o n^2$ which is a dimensionless quantity. Since the analytic expression of equation 4.23 cannot be easily found, a numerical solution is determined instead. Even in the case of setting both ϕ and ψ to zero, as shown in the previous subsection, the integral reduces to an elliptical integral which was determined numerically.

Using the expression in equation 4.23, a plot of $\Delta V/n^2 R_0 T_{life}$ as a function of the LOS1 angles ϕ and ψ is shown in Figure 4.5. Rather than plotting over all possible ϕ and ψ, the different LOS can be obtained by only varying the angle ϕ from -180° to 180° and ψ from 0° to 180°. This reduction is made possible due to the existence of pointing redundancies when the entire range of ϕ and ψ are plotted. For example, the LOS1 angles of $\phi = -90°$ and $\psi = 30°$ are as $\phi = 90°$ and $\psi = -30°$. A list of the extrema LOS1 vectors is shown in Table 4.2.

Since there exist two LOS vectors for each imaging array, by flipping the collector spacecraft over, the reverse is also true. Hence, to image a particular object, the direction in which the spacecraft should traverse in the array is determined by comparing the two LOS1 vectors. To illustrate this, the LOS1 vector configuration of $\phi = 90°$ and $\psi = 90°$ is compared with its opposite LOS1 vector of $\phi = -90°$ and $\psi = 90°$. The latter case requires a normalized $\Delta V/n^2 R_0 T_{life}$ of only 1.54 units, while the former requires a $\Delta V/n^2 R_0 T_{life}$ of 4.63 units. This represents a savings of 66.7% when a collector spacecraft traverses in the opposite direction.

In this section, we have determined the $\Delta V/n^2 R_0 T_{life}$ required for a collector spacecraft in the Forced Circular configuration to image any terrestrial targets. In the next section, we present the concept behind the other two configurations that are considered in this study.

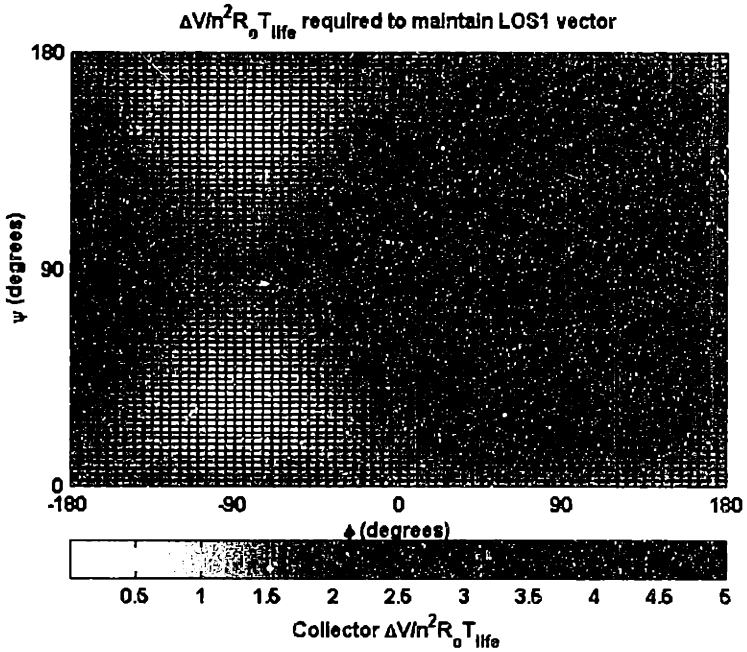

Figure 4.5 Variation in $\Delta V/n^2R_0T_{life}$ as array LOS1 vector is varied.

TABLE 4.2 Extrema LOS1 vector orientations as shown in Figure 4.5.

Extrema	ϕ (degrees)	ψ (degrees)	$\Delta V/n^2R_0T_{life}$
Minimum	-90	30	0
Minimum	-90	150	0
Maximum	90	90	4.63

4.4 Paraboloid Orbits

Rather than restricting the collector spacecraft to travel in a circular trajectory, it is possible to allow a spacecraft to follow a closed trajectory that is not circular, but projects a circular trajectory onto a plane normal to the interferometer's LOS. One such closed trajectory is elliptical. In this section, we will show that a spacecraft traversing in a propellant free orbit that projects a circle onto a plane, maps out an elliptical trajectory. The next issue is then, how does one satisfy the equal science light pathlength requirement of the interferometer? This issue is addressed in Section 4.4.2 by using the properties of a circular paraboloid. The ΔV required to maintain a configuration having different LOS is presented in Section 4.4.4. The ΔV associated with the third imaging configuration discussed in Section 4.1 is determined in Section 4.4.5.

4.4.1 Free Elliptical Trajectories

Given that a spacecraft must project a circular trajectory onto a plane normal to the interferometer's LOS, what is the trajectory that it must traverse such that minimum propellant is expended? The propellant required by a spacecraft to traverse a particular trajectory is given by equation 4.2. Since the ΔV is an integral of the instantaneous acceleration of the spacecraft over time, a global minimum is obtained when ΔV equals zero, which occurs if the integrand is also zero. In order to obtain zero instantaneous acceleration, the spacecraft acceleration in the three orthogonal directions must therefore be zero as well. Therefore, the equations of motion for a spacecraft in a propellant free orbit are given by:

$$\begin{aligned} 0 &= \ddot{x} - 3n^2x - 2n\dot{y} \\ 0 &= \ddot{y} + 2n\dot{x} \\ 0 &= \ddot{z} + n^2z \end{aligned} \tag{4.24}$$

In order to obtain equal coverage in both u and v directions, the collector spacecraft must traverse a trajectory such that a circle is projected onto the plane that is perpendicular to the array's LOS. As analyzed in Section 4.3.2 for the case with a LOS that is along the x-axis of the Hill coordinate frame, the spacecraft trajectory is chosen such that a circle is projected onto the y-z plane. The spacecraft motion projected onto the y-z plane is then:

$$\begin{aligned} y &= R_o\sin(\omega t + \alpha) \\ z &= R_o\cos(\omega t + \alpha) \end{aligned} \tag{4.25}$$

In order to determine ω, the relationship for z in equation 4.25 is substituted into the third line in equation 4.24, the relationship between ω and n is then given by:

$$\omega = \pm n \tag{4.26}$$

The existence of two answers is due to the fact that the spacecraft can rotate in either direction. Replacing the variable ω with $\pm n$, $\alpha = 0$, and taking the respective derivatives of y, the spacecraft motion in all three directions, obtained from equations 4.24 and 4.25 is therefore

$$\begin{aligned} x &= \mp\frac{R_o}{2}\cos nt \\ y &= \pm R_o\sin nt \\ z &= R_o\cos nt \end{aligned} \tag{4.27}$$

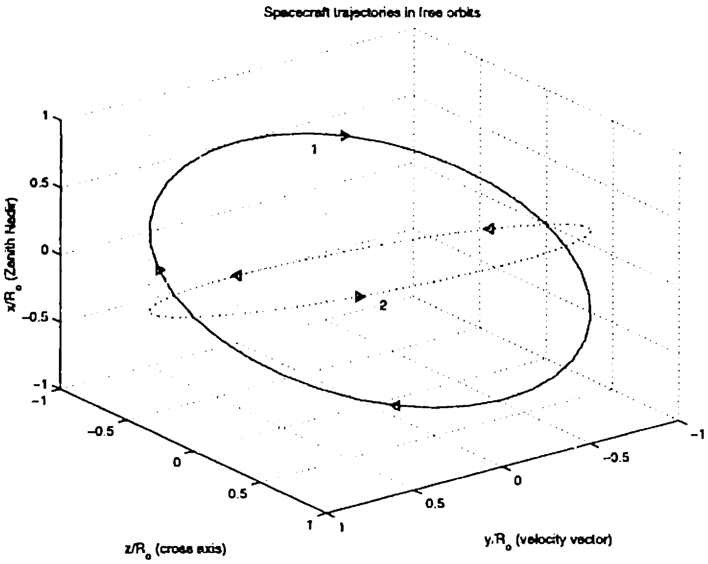

Figure 4.6 Two possible trajectories for a spacecraft to traverse in free orbits.

Equation 4.27 indicates that there are two propellant free trajectories that a spacecraft can traverse while projecting circles onto the y-z plane. In the case when $\omega = n$, a collector spacecraft will traverse in a clockwise direction when viewed from the positive x direction. This is shown as the trajectory labeled as '1' in Figure 4.6. The trajectory of a spacecraft traveling in the opposite direction is also shown in Figure 4.6 represented by the trajectory labeled '2'. Notice that both solution project a two-by-one ellipse onto the x-y as required by Hill's equations.

Given equation 4.27 and Figure 4.6, can these trajectories be represented by a simple closed form object such as a circle or ellipse? The answer to this question is yes and the trajectories defined by equation 4.27 are actually ellipses. To prove this claim, the trajectory defined in equation 4.27 is transformed such that its trajectory lies only in a principal plane in an orthogonal coordinate frame. The trajectory shown in Figure 4.6 projects a line onto the x-z plane which indicates that by rotating this trajectory by an angle η about the y-axis, this transformed trajectory will lie in the y-z plane. The angle η is found by determining the angle that the projected line makes with the z-axis. This angle is therefore

$$\begin{aligned} \eta &= \operatorname{atan}\left(\frac{x}{z}\right) \\ &= \mp 26.57^\circ \end{aligned} \tag{4.28}$$

Since the ellipse in equation 4.27 is to be rotated by an angle η about the y-axis, the transformation matrix from the xyz frame to the $x'y'z'$ frame through an angle η about the y-axis is given in equation 4.20, with its inverse transformation given by:

$$\begin{bmatrix} x' \\ y' \\ z' \end{bmatrix} = \begin{bmatrix} \cos\eta & 0 & -\sin\eta \\ 0 & 1 & 0 \\ \sin\eta & 0 & \cos\eta \end{bmatrix} \begin{bmatrix} x \\ y \\ z \end{bmatrix} \tag{4.29}$$

Therefore, substituting $\eta = \mp 26.57°$ into equation 4.29 and replacing the x, y and z variables with equation 4.27, this trajectory in the new coordinate frame will then be

$$\begin{aligned} x' &= 0 \\ y' &= \pm R_o \sin nt \\ z' &= \frac{\sqrt{5}}{2} R_o \cos nt \end{aligned} \tag{4.30}$$

Substituting equation 4.30 into the equation which defines the general form of an ellipse, one will immediately recognize that the y' and z' of equation 4.30 are the parametric equations of an ellipse with a semi-major axis of $a = \frac{\sqrt{5}}{2} R_o$ in the z' direction and a semi-minor axis of $b = R_o$ in the y' direction, centered on the origin. The general form of an ellipse centered about (h,k) is given by:

$$\frac{(y'-h)^2}{a^2} + \frac{(z'-k)^2}{b^2} = 1 \tag{4.31}$$

where h and k are the coordinates of the center which in the current example, are zero.

4.4.2 Circular Paraboloid

In the previous subsection, it was shown that a spacecraft traversing in a propellant free orbit that projects a circle onto the y-z plane, actually traverses in an elliptical motion about the origin of the Hill's frame. Hence to fulfill the equal science light pathlength requirement, is it then possible to determine a point such that the same wavefront originating from the target, passes through any point on the ellipse and arrives at this point at the same instant in time? To determine the answer to this question, the properties of a circular paraboloid are first investigated.

A circular paraboloid, as opposed to an elliptical paraboloid, is a surface that is obtained by revolving a parabola about its axis. A parabola is defined as a set of points in a plane that are equidistant from both a given fixed point and fixed line in the plane [Thomas et al, 1988]. The fixed point is called the focus of the parabola and the fixed line the directrix. However, in this application, it is the reflecting properties of the parabola that are of interest. From the definition of the parabola, one finds that the distance measured from any point on a line that is parallel to the directrix to the focus, reflected off the surface of the parabola, is the same. Hence, the equal science light path-length requirement can be satisfied by a circular paraboloid if the science light wavefront is perpendicular to the axis of the paraboloid and also planar, which is the case if the target is in the far-field.

The geometries that we have encountered thus far (circle, ellipse and parabola), together with the hyperbola, are commonly known as conic sections [Thomas et al, 1988]. These geometries are obtained by intersecting a cone with a plane. However, does the intersection between a plane and a paraboloid define an ellipse in which a spacecraft would traverse without expending any propellant? To begin this analysis, a new coordinate frame which coincides with the Hill coordinate frame is first defined as $i'j'k'$. The general form of a paraboloid opening in the negative i' direction with an apex at (h,k,l) is given by:

$$(j' - k)^2 + (k' - l)^2 = -p(i' - h) \tag{4.32}$$

The focus of this parabola is therefore located at $\left(h - \frac{p}{4}, k, l\right)$. Attaching the parabola to a coordinate system (x',y',z') such that the axis of the parabola lies on the x' axis, equation 4.32 can be rewritten as:

$$y'^2 + z'^2 = -p(x' - h) \tag{4.33}$$

with its focus located at $\left(h - \frac{p}{4}, 0, 0\right)$. Intersecting an inclined plane to this right circular paraboloid is equivalent to transforming this paraboloid such that it intersects the j'-k' plane at an inclined angle. Since a circular paraboloid is rotationally symmetric, the analysis can be simplified by rotating the paraboloid about either the j' or k' axis. Also, to simplify later comparisons between the free orbit ellipse and loci obtained from the intersection of the paraboloid and the j'-k' plane, the paraboloid is chosen to rotate about the j' axis by an angle ψ. Using the transformation matrix in equation 4.29, a paraboloid rotated by an angle ψ written in the i', j' and k' frame is therefore:

$$j'^2 + (i'\sin\eta + k'\cos\eta)^2 = -p(i'\cos\eta - k'\sin\eta - h) \tag{4.34}$$

The focus of this paraboloid is located at $\left(\left(h-\frac{p}{4}\right)\cos\eta, 0, -\left(h-\frac{p}{4}\right)\sin\eta\right)$ obtained by using the transformation matrix in equation 4.20. The intersection between the paraboloid and the *j'*-*k'* plane is obtained by setting $i' = 0$. This is given by the following equation:

$$j'^2 + (k'\cos\eta)^2 = -p(-k'\sin\eta - h) \tag{4.35}$$

By expanding the terms in equation 4.35 and completing the squares with respect to the *z'*-variable, the equation can be rewritten as:

$$\frac{j'^2}{(\cos\eta)^2} + \left[k' - \frac{p\tan\eta}{2\cos\eta}\right]^2 = \frac{(p\tan\eta)^2}{4(\cos\eta)^2} + \frac{ph}{(\cos\eta)^2} \tag{4.36}$$

Dividing equation 4.36 by the term on the right hand side, equation 4.36 takes the form of an ellipse centered about $\left(0, 0, \frac{p\tan\eta}{2\cos\eta}\right)$ when compared with equation 4.31. The inclined circular paraboloid and the ellipse that is formed from its intersection with the *j'*-*k'* plane is shown in Figure 4.7.

Depending on the angle that η is inclined at, different conic sections can be obtained. In the case where $\eta = 0^o$, equation 4.36 reduces to

$$j'^2 + k'^2 = ph \tag{4.37}$$

which represents a circle with radius $\sqrt{ph}$ centered about (0,0,0). However, when $\eta = \pm 90°$, equation 4.35 reduces to

$$j'^2 = -p(\mp k' - h) \tag{4.38}$$

which represents a parabola opening in either the positive or negative *k'* direction with its focus either at $(0, 0, -h-\frac{p}{4})$ or $(0, 0, h-\frac{p}{4})$. Therefore, the intersection between a circular paraboloid and a plane represents a circle for the case when the plane is perpendicular to the paraboloid's axis ($\eta = 0^o$), a parabola when the plane is parallel to the paraboloid axis ($\eta = \pm 90°$) and an ellipse when the plane is inclined to the paraboloid's axis.

The ellipse in equation 4.35 is centered about a point that is not at the origin of the Hill frame, which is different from the free orbit ellipse obtained in Section 4.4.1. Hence to match these two ellipses, the ellipse in equation 4.36 is translated such that it is centered about the origin of the Hill

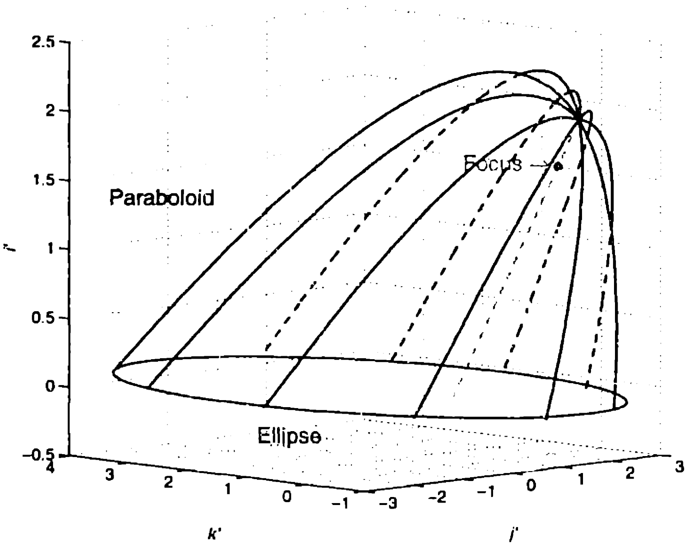

Figure 4.7 Illustration of the intersection between an inclined circular paraboloid and the y-z plane.

frame. Denoting x'', y'' and z'' as this new coordinate frame, both the paraboloid and ellipse defined in equations 4.34 and 4.36 are translated by:

$$\begin{aligned} i' &= x'' \\ j' &= y'' \\ k' &= z'' + \frac{p\tan\eta}{2\cos\eta} \end{aligned} \tag{4.39}$$

The result of the translation imposed on equations 4.34 and 4.36 is given by the following two equations:

$$y''^2 + \left(x''\sin\eta + z''\cos\eta + \frac{p}{2}\tan\eta\right)^2 = -p\left(x''\cos\eta - z''\sin\eta - \frac{p}{2}(\tan\eta)^2 - h\right) \tag{4.40}$$

$$\frac{y''^2}{(\cos\eta)^2} + z''^2 = \frac{(p\tan\eta)^2}{4(\cos\eta)^2} + \frac{ph}{(\cos\eta)^2} \tag{4.41}$$

The paraboloid will now have a focus at $\left(\left(h - \frac{p}{4}\right)\cos\eta, 0, -\left(h - \frac{p}{4}\right)\sin\eta - \frac{p\tan\eta}{2\cos\eta}\right)$, while the ellipse's center is located at the origin of the x'', y'', z'' frame. Comparing equation 4.41 with the parametric form of the free orbit ellipse, the following two equations are obtained:

$$(\cos\eta)^2 = \frac{4}{5} \qquad (4.42)$$
$$\eta = \mp 26.57°$$

$$\left(\frac{p}{2}\tan\eta\right)^2 + ph - R_o^2 = 0 \qquad (4.43)$$

Equation 4.42 indicates that a circular paraboloid which is rotated by $\eta = \mp 26.57°$ will project the ellipses that were defined by equation 4.30. The negative value of ψ corresponds to the ellipse labeled '1' in Appendix 4.6. The apex of the paraboloid in the x-axis is found by rewriting equation 4.43:

$$h = \frac{16R_o^2 - p^2}{16p} \qquad (4.44)$$

while the focus of the paraboloid, obtained in terms of p is:

$$x'' = \frac{16R_o^2 - 5p^2}{8\sqrt{5}p}$$
$$y'' = 0 \qquad (4.45)$$
$$z'' = -\frac{16R_o^2 + 5p^2}{16\sqrt{5}p}$$

The equations that have been developed thus far are in a frame in which the ellipse lies in the y'' and z''plane. Finally, equations 4.40, and 4.45 must be rotated by $\xi = -\eta$ such that the ellipse in equation 4.41 is written in its equivalent form in the Hill coordinate frame. The paraboloid, written in terms of the Hill coordinate frame, obtained by rotating equation 4.40 using the transformation matrix in equation 4.29 with $\xi = \pm 26.57°$ and substitution of p in equation 4.44 is therefore

$$y^2 + \left(z \mp \frac{p}{4}\right)^2 = -p\left(x - \frac{16R_o^2 + p^2}{16p}\right) \qquad (4.46)$$

The focus of this paraboloid, obtained using equation 4.20 with $\xi = \pm 26.57°$, is therefore,

$$
\begin{aligned}
x &= \frac{16R_o^2 - 3p^2}{16p} \\
y &= 0 \\
z &= \pm\frac{p}{4}
\end{aligned}
\tag{4.47}
$$

The parameter p defined in equation 4.32 assumes a positive value such that the paraboloid opens in the negative x direction. The parameter p cannot assume a value of zero because it represents a point on the origin of the coordinate frame. Therefore, p must be greater than 0. The upper bound of p is determined by analyzing the ordinate of the paraboloid's apex in the x direction. Given that the ellipse can only assume a maximum value of $\frac{R_o}{2}$ (from equation 4.27), the apex of the paraboloid must at least be greater than this value. Therefore, the upper bound condition for p is:

$$\frac{16R_o^2 + p^2}{16p} \geq \frac{R_o}{2} \tag{4.48}$$

Solving the above equation for p and together with the lower bound of p, one can show that the value of p is bounded between 0 and $4R_o$. A plot of a circular paraboloid in equation 4.46 intersecting with a plane to give the free orbit ellipse labelled as '1' in Figure 4.6 is shown in Figure 4.8.

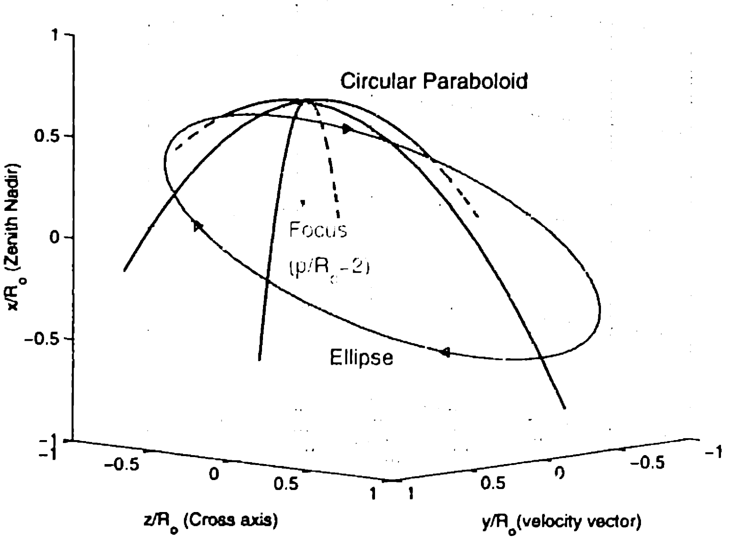

Figure 4.8 Intersection between a circular paraboloid and a plane resulting in an ellipse.

4.4.3 Paraboloid Foci - The Hyperbola

The intersection between a plane and paraboloid has been shown to produce an ellipse. Also shown in the previous subsection is that there is a family of paraboloids that will fit the free orbit ellipse by varying the parameter p. Given this family of paraboloids, which one should then be chosen? The answer lies in the location of the focus of the paraboloid that requires minimal propellant burn to maintain the combiner spacecraft location.

Before determining the optimal paraboloid that should be fitted to the free orbit ellipse, the locus of the foci of these paraboloids is first determined. Interestingly enough, as will be shown next, the foci of these paraboloids map out an hyperbola. Since the location of the focus of the paraboloids is given by equation 4.47, one can eliminate the variable p in that equation to obtain:

$$x = \frac{R_o^2 - 3z^2}{\pm 4z} \tag{4.49}$$

Equation 4.49 is in fact an hyperbola! However, to prove it more conclusively, the x and z variables are rotated such that only terms containing x^2 and z^2 are present. Using the rotational matrix in equation 4.29, equation 4.49 can be rewritten as:

$$3(x\sin\eta + z\cos\eta)^2 \pm 4(x\cos\eta - z\sin\eta)(x\sin\eta + z\cos\eta) - R_o^2 = 0 \tag{4.50}$$

The cross terms are eliminated by setting $\eta = \mp 26.57°$ and the resulting equation is:

$$\frac{4z^2}{R_o^2} - \frac{x^2}{R_o^2} = 1 \tag{4.51}$$

Equation 4.51 shows that the loci of the foci of the paraboloids, that fit onto the ellipses defined in equation 4.27, actually map out an hyperbola that is rotated by $\eta = \pm 26.57°$.

The paraboloid that should be chosen to fit the free orbit ellipse is the paraboloid with a focus that minimizes equation 4.11. Substituting the x and z variables of equation 4.47 into equation 4.11 and minimizing the resulting equation with respect to p between 0 and $4R_o$, the optimal paraboloid is the paraboloid with $p = 2.2076R_o$ that has a focus at:

$$\begin{aligned} x &= 0.0390R_o \\ y &= 0 \\ z &= \pm 0.5519R_o \end{aligned} \tag{4.52}$$

This optimal focus corresponds to a $\frac{\Delta V}{n^2 R_o T_{life}}$ of 0.5642 units as is shown in Figure 4.9 when p is varied from 0 to $4R_o$.

In this subsection, together with the previous two subsections, it was determined that in order to project a circle onto the y-z plane, collector spacecraft will have to traverse in one of two free elliptical orbits in the H''' frame. In order to meet the interferometric equal pathlength requirement, the intersection between a right circular paraboloid and a plane was found to be an ellipse, as is shown in Figure 4.8. This means that any spacecraft located on this ellipse will meet the equal science light pathlength requirement by reflecting light from the target to the paraboloid's focus and dos so without consuming propellant. Then, it was also determined that there is a family of right circular paraboloids that could fit onto the free orbit ellipse in equation 4.27. The locus of the foci of these paraboloids trace out an hyperbola. The optimal paraboloid (focus position) was found by determining the minimum ΔV required to hold a combiner spacecraft at that position. Note that these four geometrical shapes, the circle, ellipse, parabola and hyperbola, are in fact the four conic sec-

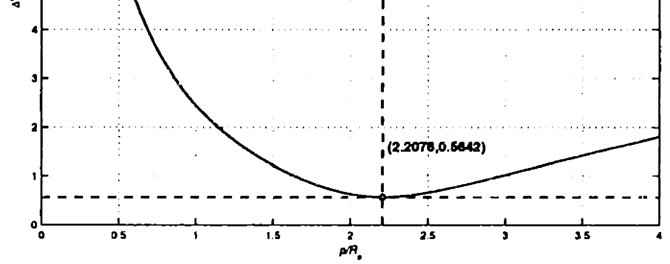

Figure 4.9 $\Delta V/n^2 R_o T_{life}$ required for combiner spacecraft as various paraboloids are fitted onto the free orbit ellipse.

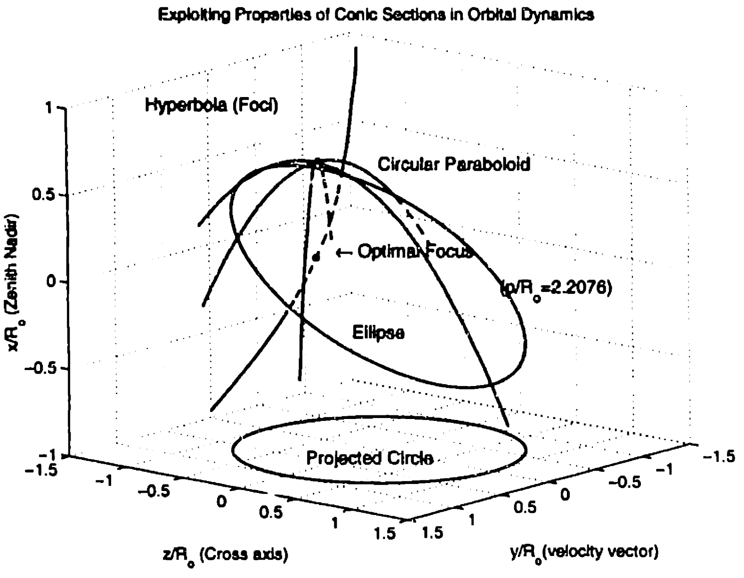

Figure 4.10 Exploitation of conic section properties in free collector orbits

tions! The exploitation of these conic sections in this orbital dynamics problem is clearly depicted in Figure 4.10.

4.4.4 Change of LOS - Rotating the Configuration

Similar to Section 4.3.3, the ΔV required to maintain the configuration for different LOS is determined for the elliptical orbit case. The free elliptical orbit given by equation 4.27 is rotated by using the rotation matrix in equation 4.22, which means that the collector spacecraft are no longer in a free orbit ellipse. The rotation of the free ellipse by the angles ϕ and ψ is given by:

$$\begin{bmatrix} x \\ y \\ z \end{bmatrix} = R_o \begin{bmatrix} \cos\psi & -\sin\psi & 0 \\ \cos\phi\sin\psi & \cos\phi\cos\psi & -\sin\phi \\ \sin\phi\sin\psi & \sin\phi\cos\psi & \cos\phi \end{bmatrix} \begin{bmatrix} \mp\frac{1}{2}\cos nt \\ \pm\sin nt \\ \cos nt \end{bmatrix} \tag{4.53}$$

Differentiating equation 4.53 with respect to time and substituting these expressions into equations 4.1 and 4.2, an expression similar to equation 4.23 is derived and is used to obtain the plot in Figure 4.11. Figure 4.11 shows the $\Delta V/n^2R_oT_{life}$ required to maintain a collector spacecraft in the rotated elliptical orbit.

As expected, a minimum in propellant usage is observed when $\phi = 0^o$ and $\psi = 0^o$ as this is the same free elliptical orbit labelled as '1' in Figure 4.6 and corresponds to imaging in the nadir

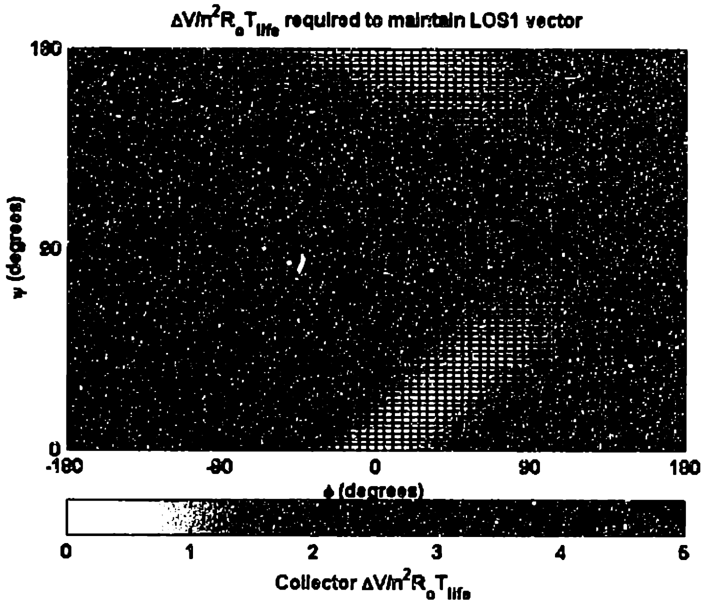

Figure 4.11 $\Delta V/n^2R_0T_{life}$ required to maintain a collector spacecraft in the rotated free elliptical orbit due to varying the array's LOS.

direction. Interestingly, a second minima occurs when the ellipse is rotated by $\phi = 0^o$ and $\psi = 180^o$. This second minima corresponds to the free orbit ellipse labelled as '2' in Figure 4.6 which confirms the occurrence of two possible free elliptical orbits that project the same circle onto the *y-z* plane. The maximum $\Delta V/n^2R_0T_{life}$ occurs when the ellipse is rotated such that a collector spacecraft traverses only in the *x-y* plane (i.e. $z = 0$) as shown in Figure 4.12. This make sense as in the case of free orbit, when a collector traverses through the highest altitude in its orbit (highest *x* ordinate), it has a minimum velocity and tends to slow down with respect to a geo-stationary point. Therefore, a spacecraft will naturally tend to rotate in the clockwise direction, opposite to the orbit shown Figure 4.12. This is the reason for the high propellant usage required to maintain a collector spacecraft in the orbit shown in Figure 4.12. The alternative to this orbit is therefore to choose the orbit with a LOS pointed at $\phi = 180^o$ to the maximum $\Delta V/n^2R_0T_{life}$ orbit (eg. $\phi = 90^o$, $\psi = 116.57^o$). The extrema points in Figure 4.11 are listed in Table 4.3.

As opposed to the analysis done in Section 4.3.3, the combiner of these imaging arrays (focus point of the paraboloid) is no longer at the center of the Hill coordinate frame. This will therefore result in propellant burn to maintain the combiner spacecraft at the focus of the chosen paraboloid. As determined in Section 4.4.3, there are a number of paraboloid foci at which one can place the combiner spacecraft for each particular LOS1 vector. The locus of feasible foci for the different LOS1 vectors is obtained by transforming the equation of the foci in equation 4.27 with the transformation matrix in equation 4.53. Substituting the resultant equation into equation 4.11 and tak-

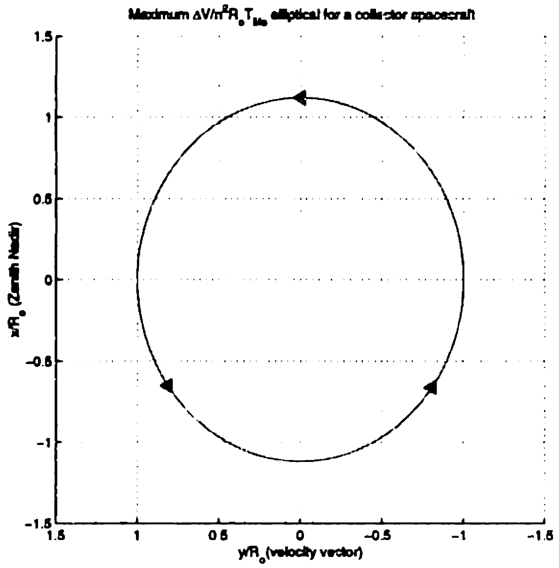

Figure 4.12 Elliptical orbit traversed by a collector spacecraft that results in a maximum $\Delta V/n^2R_0T_{life}$ value in Figure 4.11.

TABLE 4.3 Extrema LOS orientations as shown in Figure 4.11.

Extrema	**ϕ (degrees)**	**ψ (degrees)**	**$\Delta V/n^2R_0T_{life}$**
Minimum	0	0	0
Minimum	0	180	0
Maximum	0	116.57	4.99

ing the first derivative of the resulting equation, the optimal value of p for each LOS1 vector can therefore be determined. Substituting this value back into equation 4.11, the minimum $\Delta V/n^2R_0T_{life}$ required for the combiner spacecraft at the various LOS1 vectors is obtained and shown in Figure 4.13.

The plot in Figure 4.13 shows the result at any point is repeated at 180° in the angle ϕ. Unlike in Figure 4.11, it is not possible to choose another point to place the combiner such that better propellant usage configuration is obtained. To check that the result obtained in Figure 4.13 is appropriate, at $\phi = 0^o$ and $\psi = 0^o$, the minimum $\Delta V/n^2R_0T_{life}$ obtained is 0.5642, which is the result obtained in Section 4.4.3.

The LOS in this section is varied by rotating the entire array such that the LOS is pointing at the desired target. However, if certain constraints are allowed to be relaxed, it is possible to change the LOS of the array by just relocating the combiner spacecraft and not the entire array. This may

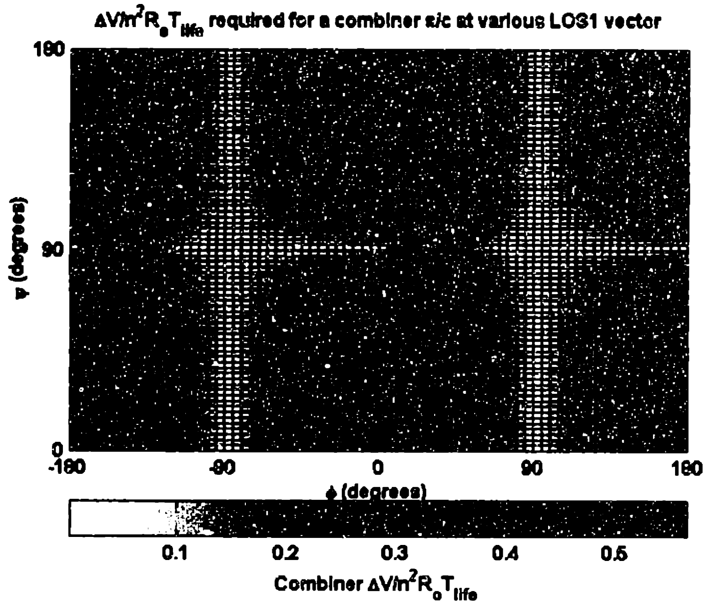

Figure 4.13 Minimum $\Delta V/n^2 R_0 T_{life}$ required to maintain the combiner s/c position at the optimum foci at the various array LOS1 vector.

prove to give better propellant performance at the expense of placing delay lines in either the combiner or collector spacecraft. The concept, which is the third imaging configuration considered in this study, is exploited in the next subsection.

4.4.5 Change of LOS - Relocating the Combiner

In the previous sections, it was determined that when a circular paraboloid is fitted onto the free orbit ellipse, the same wave front originating from the target at nadir and arriving at the focus of the circular paraboloid can be interfered when light from the target is reflected from any spacecraft located on the free orbit ellipse. However, it is only possible to fit the free orbit ellipse to circular paraboloids that have either axes that are parallel to the x-axis or parallel to the z-axis. All other paraboloids are elliptical in form and therefore have no common focus. Therefore, it is not possible to determine a single location such that the same wave front from an off-nadir target reflected off a spacecraft on an free orbit ellipse can be interfered as there exists no common focus.

However, if one were to consider using delay lines in the system to ensure that the same wave front of science light is interfered, it is then possible to determine a location for the combiner spacecraft. Hence, the objective of this section is to determine the optimal location to place the combiner spacecraft and the maximum delay length required to image an off-nadir target.

For an LOS pointing in the angles of ϕ and ψ, the task is therefore to fit parabolas with axes that are parallel to the LOS specified. However, in this analysis, the ellipse will first be rotated by $-\psi$ and then $-\phi$ such that parabolas with axes that are parallel to the x-axis are fitted to the rotated ellipse. The transformation matrix for the ellipse, taking into account the signs of the angles, is therefore

$$\begin{bmatrix} x' \\ y' \\ z' \end{bmatrix} = R_o \begin{bmatrix} \cos\psi & \sin\psi\cos\phi & \sin\psi\sin\phi \\ -\sin\psi & \cos\psi\cos\phi & \cos\psi\sin\phi \\ 0 & -\sin\phi & \cos\phi \end{bmatrix} \begin{bmatrix} \mp\frac{1}{2}\cos nt \\ \pm\sin nt \\ \cos nt \end{bmatrix} \tag{4.54}$$

The different parabolas are determined by fitting them onto the different pairs of opposing points on the rotated ellipse (nt and $nt + \pi$). Associated with these parabolas are their foci which are the equal pathlength locations from the target via the two opposite points on the ellipse. The general form of the parabola that is to be fitted onto the two points on the ellipse is given by equation 4.32 while the focus of the paraboloid is given by $\left(h - \frac{p}{4}, k, l\right)$. However, rather than dealing with the four variables of the paraboloid, it is possible to simplify the paraboloid equation by rotating the ellipse about the x-axis such that the two opposite points on the ellipse lie on $y = 0$. Using the transformation matrix in equation 4.19, the angle in which the ellipse has to be rotated is given by $\phi = \operatorname{atan}\left(\frac{y'}{z'}\right)$ and the equation of the parabola to be fitted onto these two points is therefore

$$(z' - l)^2 = -p(x' - h) \tag{4.55}$$

Substituting the ellipse in equation 4.54 into equation 4.55, and manipulating the equations, it is possible to determine the focus of the parabola as a function of p only. The focus of the fitted parabola is then rotated back by the angle $\phi = -\operatorname{atan}\left(\frac{y'}{z'}\right)$, again using the transformation matrix in equation 4.19 to give the location of the focus in the $x'y'z'$ frame. Hence, for each opposite pair of points on the ellipse, the different values of p will therefore determine the equal pathlength location from the target via these two points. The idea is then to determine the values of p for the different opposite pairs of points on the ellipse such that the distances between the foci are being minimized. The location of the combiner spacecraft is then the mid point between the two foci that are furthest apart.

The determination of the combiner spacecraft location as described in the above paragraph is only valid for combining light from the collector spacecraft that are located at the opposite points on the ellipse. In order to combine light from points that are not located at the opposite points on the ellipse, the difference in pathlength from the target to the respective foci via any collector on the ellipse must also be minimized. Hence the metric to determine the maximum pathlength required in the system is the maximum between half the length of the two foci that are furthest apart and the maximum difference in pathlength from the target to the respective foci.

Once the location of the combiner is determined in the $x'y'z'$ frame, the entire array is then rotated by the angles ϕ and ψ, using equation 4.22 such that the collector spacecraft trajectory is the free elliptical orbit. This step is required to determine the location of the combiner spacecraft in the Hill coordinate frame but is not required to determine the maximum difference in pathlength from the target to this location.

Since the maximum of the delay lines required in the system is of interest, one can then simplify the problem by setting one of the two rotation angles to zero, while the other is set to the maximum. For comparison with the Section 4.5 and to simplify the mathematics, the values chosen for ϕ and ψ are 0^o and 5^o, where the latter value is the maximum extent at which the LOS for a system in a geo-stationary orbit can still point to a location on the Earth's surface. The imaging points on the ellipse chosen for this optimization are equally spaced at 10^o apart. Therefore, for each case, there are 18 parameters (p) to be optimized.

The optimization technique used to determine the eighteen parameters is the same as the one used in Chapter 2, simulated annealing. However, in this optimization, in each trial, one of the 18 parameters is chosen randomly and substituted with a random value. Unfortunately, it was not possible to determine the global optimum set of p due to the large number of variables and possibilities for p. Hence, optimal locations for the combiner spacecraft were optimized for bounded values of the parabola sizes (p). A plot of the maximum delay required to combine light from the different collector spacecraft against the average value of p_{ave} is shown in Figure 4.14. The average parabola size, p_{ave} is determined by taking the average of the 18 values of p fitted onto the ellipse.

Figure 4.14 shows that as the size of parabola is decreased (small p_{ave}), less delay is required to combine light from the different collector spacecraft. This makes sense as smaller parabola sizes correspond to the focus of the parabola being further away from the ellipse along the axis of the parabola. Hence, as p_{ave} approaches zero, the foci of the parabolas approach infinity which means that the differential distance between the collector spacecraft and the combiner approaches zero. As the size of the parabolas increases, larger delay is required to combine light from the different

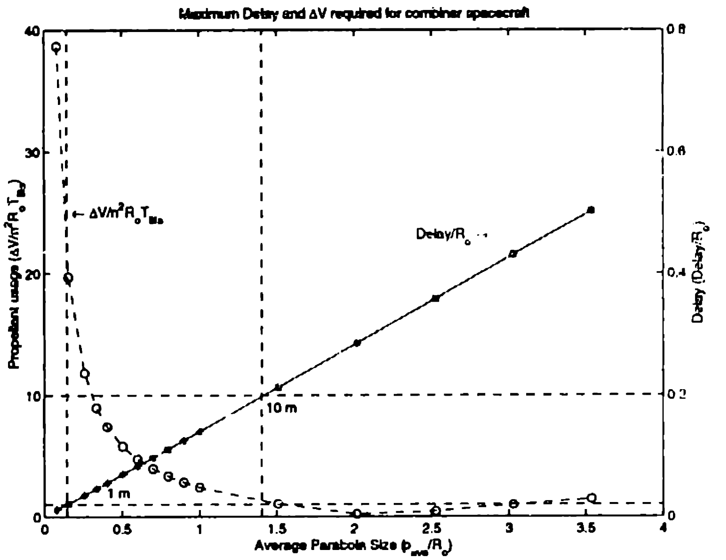

Figure 4.14 Maximum delay line required to combine light from spacecraft in the elliptical orbit and the $\Delta V/n^2R_0T_{life}$ required to maintain the combiner spacecraft for the different imaging configurations

collector spacecraft when an off-nadir target is imaged. Hence, the imaging configuration which required the least optical delay will therefore be one with a small value of p_{ave}.

However, the disadvantage in choosing small values of p_{ave} is that the focus is located at a very large distance away from the center of the Hill coordinate frame and according to equation 4.11, this corresponds to high propellant usage. Included in Figure 4.14 is also the $\Delta V/n^2R_0T_{life}$ required to maintain the combiner spacecraft for the different values of p. As in the case of fitting a circular paraboloid onto the free orbit ellipse in Section 4.4.3, there exists an optimal location in terms of ΔV to place the combiner spacecraft. The value of p_{ave} that corresponds to this minimum ΔV location is approximately $2.015R_o$. The increase in ΔV beyond this point is due to the increase in the z ordinate of the combiner spacecraft as p_{ave} is increased. The corresponding maximum optical delay required to combine light from the different collector spacecraft at the minimum ΔV location is $0.2856R_o$.

Hence, given that the array projects a circle of radius 50 m onto a plane that is perpendicular to the LOS and say that only a maximum delay of 1 m is allowable, what is then the minimum ΔV required to maintain the location of the combiner spacecraft? According to Figure 4.14, the minimum $\Delta V/n^2R_0T_{life}$ required to maintain the spacecraft is approximately 20 units which is high compared to the value required to hold a combiner spacecraft by re-orientating the entire array as shown in Figure 4.13. However, if a maximum delay of 10 m is introduced, the $\Delta V/n^2R_oT_{life}$ required is only 1.36 units! This represents a savings of at least 93% in the ΔV requirement and may prove to be the more efficient design for off-nadir imaging especially when the total $\Delta V/n^2R_oT_{life}$ requirement for each design is considered. This comparison is made and discussed in Section 4.5.

4.5 Case Study: Geosynchronous Orbit

The propellant requirements that have been determined thus far are in terms of a normalized ΔV with respect to the frequency of the orbit, the size of array and the lifetime of the mission. In order to get some numerical sense of the amount of propellant required, a case study involving the different orbit designs for an Earth imager operating at a geosynchronous altitude is presented. Note that even though a geosynchronous orbit case study is presented, the analysis thus far is valid for any Earth orbit. The propellant requirements for the different orbits can be determined by changing the value for the orbital frequency, *n*.

For a separated spacecraft interferometer centered about a geostationary orbit, the different spacecraft appear to be hovering about a point on the equator. At this altitude, the horizon-to-horizon field-of-view for the spacecraft is approximately $\pm 8°$. However, since it is not possible for the spacecraft to image a target that is located at the horizon, in this comparison, the LOS of the array is limited to $\pm 5°$ from the nadir axis which is consistent with the value used in Section 4.4.5.

4.5.1 Mission Parameters

In order to compare the performance of the different orbit designs, the propellant requirement of the system can be obtained from equation 4.3. However, since the results obtained thus far are in terms of $\Delta V/n^2R_oT_{life}$, one must therefore specify the orbit of the system, the size of the constellation and the lifetime of the mission. As this case study is performed for a system in the Earth's geosynchronous orbit, the value of *n* is therefore 7.27×10^{-5} rad/s. For comparison purposes, the size of the array is set at $R_o = 100$ m and the mission lifetime is arbitrarily chosen to be 10 years.

In order to complete the propellant calculation using equation 4.3, the mass estimates for the spacecraft must be assumed. The mass estimate for a collector spacecraft is set to 150 kg, while the combiner is set to 250 kg as these values are obtained from the proposed DS3 mission and are also consistent with the values used in Chapter 3. A cold gas propulsion system with a specific impulse of 62.5 sec. is assumed for all the spacecraft.

Also, to simplify the calculation, all the collector spacecraft are assumed to travel on the same trajectory in the Hill coordinate frame. Hence, the total collector spacecraft propellant requirement is then just simple multiplication of the propellant required by a single collector spacecraft by the number of collector spacecraft in the system.

4.5.2 Mass Comparisons

Using the mass estimates presented in the previous subsection, plots of the total propellant required in the system as a function of the number of collector spacecraft for both the forced circular and the free elliptical designs are presented in Figure 4.15. The interferometer is assumed to image a target that is directly below the constellation. For the Forced Circular case, the figure shows that as the number of collector spacecraft is increased, the propellant requirement in the system increases linearly. However, no propellant is required for the combiner spacecraft as it is located on the center of the Hill coordinate frame. In the case of the free elliptical design, propellant is only required for the combiner spacecraft to hold its position at the focus of the imaginary circular paraboloid. No propellant is required for the collector spacecraft as they are in the free elliptical trajectory, which is a propellant free orbit around the Earth. Hence, the propellant requirement for an interferometer using the free orbit design remains the same even if more collector spacecraft are added into the system. From the figure, one can clearly see the significant advantage in propellant usage in using the free elliptical design. This significant advantage leads to the conclusion that it is more favorable to choose the free orbit design to image a target directly below the constellation.

Extending the comparison further, the propellant required to maintain the spacecraft in configurations such that targets that are located off the nadir axis can be imaged is also determined. The maximum and minimum propellant requirement for the two different designs determined by varying the LOS within the ±5° horizon-to-horizon limit, are presented in Figure 4.16. The LOS of the system is varied by slewing the entire array. As in Figure 4.15, the propellant requirement for the Forced Circular design varies linearly with the number of collectors. However, in the case of the Free Elliptical design, the maximum propellant requirement for the system is dependent upon the number of collector spacecraft and also the location of the combiner spacecraft. This maximum propellant requirement is determined by adding the total propellant required for the collector

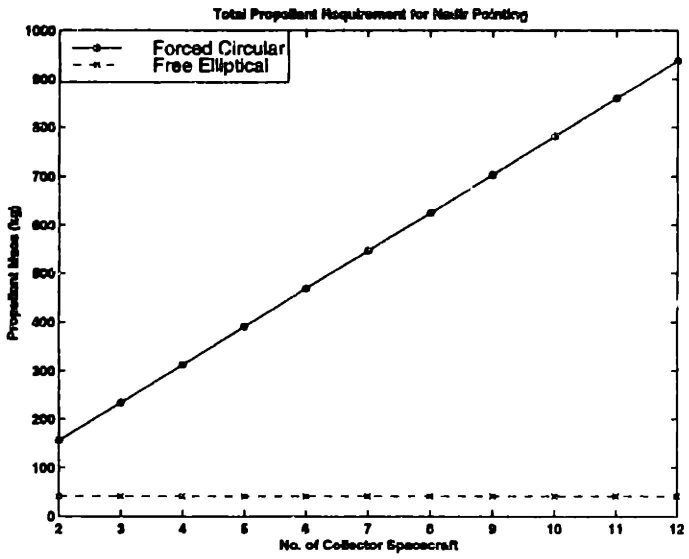

Figure 4.15 Comparison of total spacecraft propellant required for nadir pointing Earth imager.

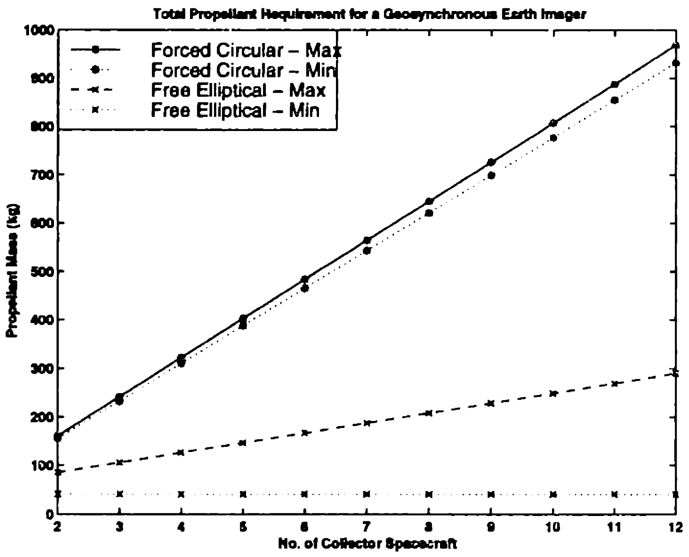

Figure 4.16 Comparison of total spacecraft propellant required for off-nadir pointing Earth imager.

spacecraft to maintain their position in their elliptical trajectory, which is not a free orbit for an off-nadir LOS configuration, and the propellant required to hold the combiner spacecraft at the focus of the imaginary circular paraboloid. It is clear from Figure 4.16 that the propellant requirement for the free elliptical design is significantly lower than that required by the forced circular design. This point is greatly emphasized as the number of collector spacecraft is increased in the system.

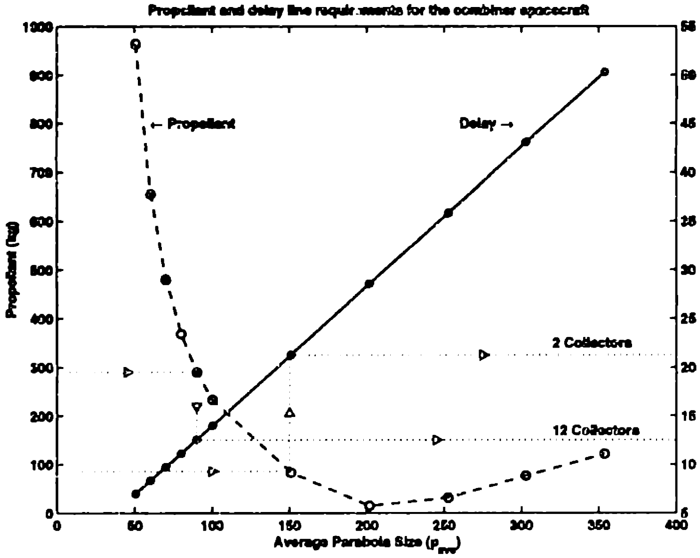

Figure 4.17 Relocating the combiner spacecraft for off-nadir imaging.

Even though in the $\Delta V/n^2 R_o T_{life}$ plots for both of these designs (Figure 4.5 and Figure 4.11) tend to indicate that relatively similar amounts of propellant are required for the two designs when the LOS of the systems are varied, the plots in Figure 4.16 do not support such observation. This is because only imaging configurations with LOS that are within the ±5° region are considered in Figure 4.16 for Earth imaging purposes. Due to this small change in the pointing of the LOS for imaging off-nadir targets, the propellant requirement for the two designs do not change appreciably from the amount of propellant required for nadir pointing. Note that in Figure 4.16, the minimum propellant for both the designs correspond to the propellant requirement for nadir pointing, as expected for the free elliptical design.

As was discussed earlier, another possible design for off-nadir LOS imaging is to move the combiner spacecraft only in the free elliptical trajectory design. In such a design, depending upon the location of the combiner spacecraft, delay lines must be included in the system such that the same wavefront originating from the target through the collector spacecraft can be interfered at the combiner. Figure 4.17 shows the propellant requirement to maintain the position of the combiner spacecraft and the minimum delay lengths required in the system as a function of the average paraboloid size for imaging a target that is located at 5° off nadir. The propellant and delay line requirements can be assumed to be smaller for targets that are located at less than 5° off nadir.

From the figure, it is clear that as the size of the paraboloid is increased, less propellant is required to maintain the combiner spacecraft. However, the downside is that longer delay length is required in the system. Therefore, if one can design a system with long delay lines, it is then possible to reduce the total propellant requirement for the combiner spacecraft. Note that increasing the delay line length beyond 28 m will in fact increase the propellant required to maintain the combiner spacecraft location for reasons that are discussed in Section 4.4.5.

Since the only propellant required in this design is used to maintain the combiner spacecraft location, increasing the number of collector spacecraft in the system does not change the propellant requirement. In fact, more propellant savings can be achieved when systems with high numbers of collector spacecraft are compared. For example, in the case of the twelve collector spacecraft following an elliptical trajectory, the maximum propellant requirement for the system is determined to be 290 kg from Figure 4.16. If only the combiner is moved, this amount of propellant will allow the system to image a 5° off nadir target with only a delay length of 12.5 m. However, if the maximum amount of propellant required for the two collector spacecraft in the elliptical orbit is used, the minimum length of delay lines required for the combiner steering system is then 21 m. Hence, if one were to come up with a design that allows for 21 m delay lines, there is no advantage in going with the combiner steering system for a two collector system. However, the twelve collector spacecraft array with save at least 200 kg worth of propellant. Both the maximum propellant requirements for the two and twelve collector spacecraft in the elliptical trajectory are shown in Figure 4.17.

Depending upon the length of the delay lines that are available in the system, significant amounts of propellant can be saved. At present, a reasonable length of a delay line is in the order of meters, which is the typical dimensions of a spacecraft. However, a recent design proposal for the DS3 interferometer is to use only two spacecraft. On one of the collector spacecraft, delay lines are being placed so that the same wavefront can be combined at this spacecraft. Should this design be chosen, the limit at which these delay lines can be built may be pushed further.

4.6 Other Considerations

It is clear from the previous section that the best trajectory design for an Earth imager is to use the elliptical trajectory design. Taking this another step further, the most ideal orbit design for an Earth imager is the ability to change the LOS of the system by changing the location of the combiner spacecraft only. This, of course, depends upon the length of the delay lines available. However, there are a number of issues that arise from this analysis. The following are the discussions of the issues that came out from this analysis and the issues that warrant future considerations.

Circular versus Elliptical Trajectories

In the previous section, it was determined that there exists a significant propellant advantage in using the elliptical trajectory design. There are, however, two disadvantages in using such a design. In the circular trajectory design, since all the spacecraft are designed to follow a trajectory that is perpendicular to the LOS of the interferometer, the angle between the light from the target and the light reflected to the collector is the same (90^o) for all the collector spacecraft irrespective of their location in the circular trajectory. This, however, is not true for the elliptical trajectory design. Since the elliptical trajectory projects a circle which is perpendicular to the LOS of the interferometer, the elliptical trajectory itself is not perpendicular to the LOS. This will then change the angle between the incident light from the target and the reflected light to the combiner as the collector spacecraft travels in its elliptical trajectory. For example, the angle between the two light rays for a collector spacecraft that is at the highest point of the elliptical trajectory will always be smaller than the angle for a spacecraft located at the lowest point of the trajectory. Therefore, some form of control at the collector must ensure that reflected light is constantly re-directed towards the combiner spacecraft.

The second disadvantage that the elliptical design inherited is the different angles at which the science light must be reflected (to the combiner spacecraft) by the collector spacecraft as it traverses along in its elliptical trajectory. Consider the case in which the combiner spacecraft is not in the elliptical trajectory plane as shown in Figure 4.18. To ensure that the science light is reflected to the combiner spacecraft, the angle at which a collector spacecraft must reflect the light when it is at the top of the elliptical trajectory (α_1) is smaller when compared to a collector spacecraft that is at the lowest point of the trajectory (α_2). Not only do the collectors need to ensure that the reflected light is directed at the combiner spacecraft, the combiner spacecraft must also ensure that the instruments that receive the reflected light are also pointed at the collector spacecraft ($\beta_1 \neq \beta_2$). This second issue, however, does not appear for the case when the combiner spacecraft is in the plane of the elliptical trajectory.

Note that even though the distance between the collector spacecraft and the combiner spacecraft changes as the spacecraft traverses the elliptical trajectory, this however is not an issue. In fact, the difference of these distances is the key to allow the same wavefront to be combined at the collector.

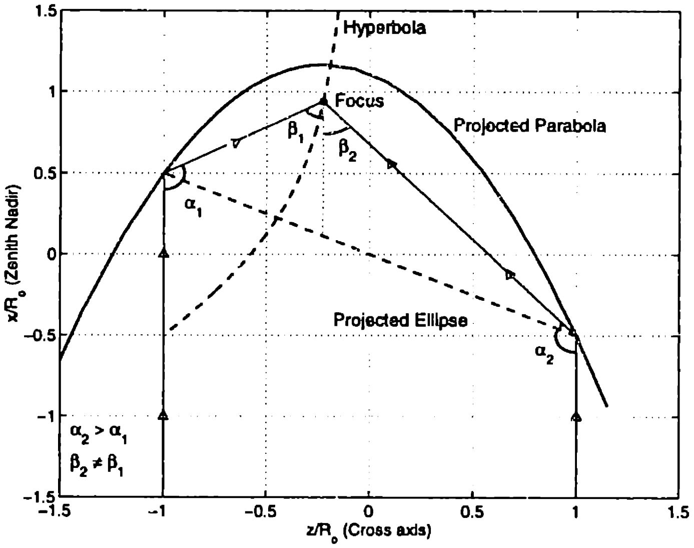

Figure 4.18 Difference angles between the incoming light ray and the reflected light ray at the collector and the angles at which the combiner spacecraft see the collector spacecraft.

Free Elliptical and Combiner Relocation

In Section 4.4.5, the maximum delay length required for the system as a function of the location of the combiner spacecraft was determined. In this design, there does exist a point at which the reflected light rays from the collector spacecraft can be brought together such that the same wavefront is interfered at the combiner. Hence, the determination of the maximum delay line required. However, as the collector spacecraft rotates about its elliptical trajectory, the distance between the combiner and the collector spacecraft changes and hence, the distance from the target to the combiner spacecraft via the collector spacecraft changes as well. Therefore, depending upon the location of the collector spacecraft, some form of control must be used to change the length of the delay lines. This issue, however, does not exist for both the forced circular and the free elliptical designs, where the LOS of the array is varied by slewing the entire array.

The delay lines required in the array can either be placed in the combiner or on the collector spacecraft. Assuming that for each collector spacecraft, a delay line is required, then one can either place all these delay lines in the combiner spacecraft or place a delay line on each collector. By placing all the delay lines on the combiner, the array reliability may be significantly reduced since it is a single point failure that now has additional mechanisms. Hence, it makes more sense to place the delay lines in the collector as the failure of a collector spacecraft will not render the entire array useless. It also makes more sense to distribute the mass of the optics among the collector spacecraft to reduce the amount of propellant required in the system due to the higher combiner spacecraft mass.

Varying the Array's LOS

In this chapter, the pointing of the array's LOS has been considered only for cases where the entire array is slewed or only the location of the combiner spacecraft is changed. In all these cases, the shape of the collector trajectories remain the same. There exist, however, possibilities of imaging an image located off-nadir requiring only propellant to maintain the location of the combiner spacecraft and not requiring any delay lines. The following discusses such a design.

In the case of the free elliptical orbit design, it was determined that a circular trajectory is projected onto a plane that is perpendicular to the array's LOS. It was shown that this free elliptical trajectory makes a 26.57° angle with the Hill's y-z plane. The spacecraft that travels in this elliptical trajectory does not require any propellant. Projecting this free elliptical trajectory onto the x-y plane, an ellipse with a dimension of two units in the y direction and one unit in the x direction is seen. Using equations 4.1 and 4.2, it can be shown that this projected two-by-one ellipse is the reason why no propellant is required for the collector spacecraft. Hence, any spacecraft trajectory that has a two by one ellipse projected onto the Hill's x-y plane, is in fact a free orbit.

Surely, there must exist more than one trajectory that can project a two by one ellipse onto the x-y plane. To show this, a circular trajectory in the y-z plane is considered. In order for the circular orbit to project a two-by-one ellipse, the circular trajectory must be rotated by either $\pm 30^{\circ}$ along y-axis, depending upon the direction the collector spacecraft is travelling. From Figure 4.5, rotating the trajectory by 30° corresponds to an LOS pointing at $\phi = -90^{\circ}$ and $\psi = 30^{\circ}$ which requires no propellant expenditure. Therefore, between the angles 26.57° and 30° about the y-axis, there must exist elliptical trajectories that project a two-by-one ellipse onto the x-y plane.

Depending upon the projection angle, all ellipses do project a circle onto a plane. Since it is possible to fit a circular paraboloid onto a projected circle, as shown in the free elliptical design, it is then possible to fit different circular paraboloids onto the different free trajectory ellipses. The LOS of arrays in these free orbit ellipses are perpendicular to the plane in which the circular trajectory is projected. And, if circular paraboloids can be fitted onto these elliptical trajectories, then there exist foci at which the combiner can be placed such that the same wavefront originating from the target can be interfered. Hence, there exist a number of free elliptical trajectories such that targets located off-nadir can be imaged.

It was shown that the free elliptical trajectory that is rotated by an angle of 26.57° about the *y*-axis has an LOS of 0° with respect to the nadir direction. The free circular trajectory, however, has an LOS of 30° with respect to the nadir direction in the *x*-*z* plane. Hence, this suggests that changing the free trajectory plane by only 3.43° changes the LOS of the array by 30°.

The free elliptical trajectories that exist between the angles 26.57° and 30° about the *y*-axis are limited to imaging targets that are in the *x*-*z* plane (side-looking imager). At the angle 30°, the orientations of the semi-major and the semi-minor axes of the elliptical trajectory swap and causes the direction of the projected circle to bifurcate beyond 30° of side-looking elevation. This limiting case for these free elliptical trajectories is the two-by-one ellipse in the *x*-*y* plane itself. Since the ellipse is of dimension two in the *y* direction, the LOS of the array must lie in *y*-*z* plane in order to obtain a circular projection. In fact, there exist four directions at which the ellipse can be viewed to get a circular projection. Therefore, between the free circular trajectory and the two-by-one ellipse, the LOS of the array must change from being in the *x*-*z* plane to the *x*-*y* plane. Considering only the viewing angles from the positive *z* direction, the LOS of the array splits into two directions to approach the two positive *z* direction LOS of the two by one ellipse as the free trajectories are rotated beyond the 30° mark.

Hence, there exist other free propellant trajectories that allow imaging of off-nadir targets and require no delay lines. Even though the horizon-to-horizon limit for a geosynchronous system is only 7°, this analysis can be applied to a system in low earth orbit, which has a horizon-to-horizon limit of approximately ±40°. These free propellant trajectories are currently being investigated and are the subject of on-going research.

Spacecraft Reorientation

The propellant requirements that were determined in this chapter were obtained for maintaining the spacecraft in their corresponding trajectories. The propellant required to re-orient the array was not considered. The array can be re-oriented in several ways. The first is to expand the size of the array, that is to change the size of the projected circle. The entire array can also be relocated to another point on the *y*-axis so that different parts of the Earth can be imaged. The optimal trajectories to re-orient the spacecraft can be determined using principles of optimal control theory [Kirk, 1970].

Increasing the Number of Collectors

Both the mass of the collector and combiner spacecraft in this analysis are assumed to be independent of the makeup of the array. However, if there are more collector spacecraft in the array and all of the reflected light is to be combined simultaneously, more optics and therefore complexity would be required of the combiner spacecraft. Therefore, the mass of the combiner spacecraft should be dependent upon the number of collectors in the array. If this adjustment is made to the combiner spacecraft, the propellant required to maintain the position of the combiner spacecraft in the array will increase and hence increase the total propellant requirement. This may possibly make the forced circular design more favorable especially for an array with a high number of collector spacecraft.

Imaging Inter-Stellar Objects

Even though the focus of this chapter was the design of orbits geared towards Earth imaging, it is possible to use these orbits to image inter-stellar objects. Unlike an Earth imaging system, the interferometer does not have continuous view of the target, except for objects that are located perpendicular to ecliptic. Hence, the trajectories of the spacecraft must be designed such that the LOS of the array is pointed at the object long enough to obtain interferometric measurements. Of course, the maximum attainable baseline of such a system will be smaller than an interferometer located outside the Earth's gravity-well.

4.7 Summary

In this chapter, different orbit designs for a multiple spacecraft interferometer system for an Earth imager are presented. The framework in which the analysis is carried out is presented together with the general form of the ΔV calculation.

Since it is assumed that the system is to be used for Earth imaging in the visible regime, three different orbit designs that satisfy the interferometric requirements are presented. The first is a forced circular design, in which the collector spacecraft are forced to follow a circular trajectory with the combiner located at the center of the trajectory. The propellant requirement for the spacecraft are determined as a function of the array's LOS pointing.

The second orbit design that is presented is the free elliptical trajectory. This innovative orbit design has all the elements of the conic sections. From the interferometric requirements, it was determined that the optimum coverage is provided by a circular u-v coverage. Requiring that the projection of the spacecraft trajectory be that of a circle, the free orbit trajectory for these collector are found to be an ellipse. It was then shown that the ellipse is in fact the result of intersecting a plane and a circular paraboloid. From the property of a circular paraboloid, the combiner spacecraft is then placed at the focus of this paraboloid such that the distance from the target through any of the collectors on the free elliptical trajectory to the combiner spacecraft is the same. However, it was then determined that there exist more than circular paraboloid that can fitted onto the elliptical trajectory, which means that there exists more than one location at which the combiner can be placed. In fact, the locus of the focus traces out an hyperbola. Hence, it was determined that collector spacecraft that traverse along a free propellant elliptical trajectory met the circular u-v coverage requirement. It was then determined that to provide equal pathlength from the target to the combiner via the collectors, the combiner spacecraft should be placed at the focus of the imaginary circular paraboloid fitted onto the elliptical trajectory. The locations at which the combiner spacecraft can be located was then determined to be an hyperbola. Since the collector spacecraft do not require any propellant, the only propellant expenditure comes from maintaining the combiner spacecraft at one of these foci. In order to image off-nadir targets, the entire array is slewed such that the array's LOS is directed at the target, which means that the collector spacecraft is no longer in a free propellant elliptical trajectory.

There is, however, another alternative for imaging off-nadir targets: relocating the combiner spacecraft only. This option, however, requires the introduction of delay lines to ensure that the same wavefront from the target is interfered at the combiner. This option is most advantageous for an array with a large number of collector spacecraft. In reality, one is actually substituting delay lines for the propellant required by the array for off-nadir imaging. This is the third design option considered in this study.

Comparison of the first two orbit designs for a geosynchronous Earth imager clearly indicates the significant propellant savings realized in using the free elliptical design. This savings is most pronounced when the array consists of a high number of collector spacecraft. The downside in choosing the free elliptical design, however, is the more complex instrumentation required to ensure that the reflected light from the collector spacecraft is directed towards the combiner spacecraft and that the combiner optics are pointed correctly. Depending upon the length of delay lines are available, the third design option warrants further consideration.

Issues that arise from using the different orbit designs are discussed. Another innovative concept to allow off-nadir targets to be imaged is briefly discussed. This concept involves that the size of the free elliptical trajectory be changed such that different free elliptical trajectories can be formed. Spacecraft in these free elliptical trajectories do not require any propellant to maintain their position in the trajectory. Finally, the need for determining the optimal trajectories to relocate the spacecraft is also discussed briefly.

Chapter 5

CONCLUSIONS

5.1 Summary

The main objective of this study was to determine the optimal imaging trajectories for a separated spacecraft interferometer operating either within or outside a gravity-well. The approach taken in this study was to first determine the optimal imaging configurations and then the appropriate optimal trajectories of the spacecraft through these configurations. In the case where the interferometer is placed outside a gravity-well, the optimal imaging locations are identified so that the optimal trajectories can be derived. For an Earth imager, the minimum aperture size is found such that images of a terrestrial target can be obtained using a minimum mass array. The orbits in which these apertures should be placed are also derived.

5.1.1 Imaging Configurations

In this study, the derivation of the optimal imaging configurations for a separated spacecraft interferometer was separated into two major sections. In the first section, where a Michelson interferometer was used, the optimal imaging locations for different numbers of apertures operating in the radio regime was found. The mean square error (MSE) metric was used to find these locations. This measure determines how well an interferometer with a limited number of apertures mimics the nominal point spread function (PSF). Comparison with proposed imaging configurations such as Cornwell and Golay clearly indicates that the optimized MSE imaging configurations are better at mimicking the nominal PSF.

Furthermore, this methodology allows different weightings to be placed across the nominal PSF in order to tailor the distribution of ambiguity in the point response. This is to say that imaging locations that best mimic the weighted nominal PSF can be determined, a feature which is not possible using the metrics that have been proposed elsewhere. For example, the imaging locations that will suppress sidelobes in a preferential portion of the PSF map were presented.

The optimal imaging locations for an interferometer operating in the visible regime were also studied. Specifically, a two collector and one combiner interferometer was considered. The results obtained from the study clearly indicate that more imaging locations allow the ideal PSF to be better replicated. However, the incremental improvement in point response quality (rate of return) diminishes as the number of imaging locations is increased.

The second section deals with a Fizeau interferometer used for Earth imaging. Rather than determining the optimal imaging locations, Golay and Cornwell configurations are used as they are optimized for instantaneous u-v coverage. With these imaging locations, the minimum aperture size required for full instantaneous u-v coverage is found as a function of the number of apertures. In the case where the interferometer is only operating at a single electromagnetic frequency, smaller apertures are required when the Golay imaging locations are used. The fill factor, the ratio of the interferometer's total aperture area to the area of a filled aperture area that provides equivalent u-v coverage, decreases as the number of apertures is increased. However, if the interferometer has the capability to operate over the entire visible spectrum, significant improvement in fill factor is observed when the Cornwell imaging locations are used. Again, the fill factor for the two imaging configurations improve as the number of apertures is increased.

5.1.2 Imaging Outside the Gravity-Well

Using the optimal imaging locations for the two collector and one combiner interferometer operating in the visible regime, the optimal trajectories to move the collector spacecraft to these locations were found. The two performance measures that were considered in determining the optimal trajectories were the propellant mass and maneuvering time metrics. In the time optimized trajectories, it was assumed that the required propellant mass is very small compared with the spacecraft dry mass. It was found that by increasing the number of imaging locations, more resources were required for the spacecraft to complete their trajectories.

Combining the optimal trajectory results with the image quality results, it is clear that the optimized MSE imaging locations provide better image quality while requiring fewer propellant and time resources. In general, when the image quality of the interferometer is increased by increasing the number of imaging locations, the resources required for the spacecraft to complete the trajectories increases as well. Similarly, as the image quality of the system is decreased, fewer resources are required.

Rather than just increasing the propellant required for the spacecraft to complete trajectories with more imaging locations, it is also possible to add more collector spacecraft to the interferometer. In cases where the propellant mass approaches the dry mass of a spacecraft, there exist an optimum number of spacecraft that should be used in the interferometer to minimize lifetime mass of the total array.

5.1.3 Imaging in Earth's Gravity-Well

In Chapter 4, the orbit designs for a separated spacecraft Earth imager operating in the visible regime are presented. The spacecraft must be placed in orbits that bound the relative motion between spacecraft and provide axisymmetric angular resolution while allowing the same wavefront to be interfered. In this study, two orbit designs were discussed. Of the two, the simpler design has the collector spacecraft following a circular trajectory in the plane normal to the line-of-sight with the combiner placed at the center of this trajectory.

The second orbit design involves an innovative use of all four conic sections. In order to provide equal resolution in all directions, the trajectory of the collector spacecraft projected onto the image plane must be circular. Spacecraft traversing in a free elliptical trajectory in the Hill's frame can provide this circular projection. By placing a combiner spacecraft at the focus of an imaginary circular paraboloid fitted onto the free elliptical trajectory, a common wavefront of light reflected from the various collector spacecraft can be interfered in real time. Depending on the size of the circular paraboloid, there exist a number of locations at which the combiner spacecraft can be placed. This locus of foci actually traces out a hyperbola. Since this hyperbola does not pass through the Hill's origin, the location at which the combiner consumes the least propellant was found.

Comparison of the two orbit designs for an interferometer operating in a geosynchronous orbit clearly shows the significant savings of the free elliptical orbit over the circular trajectory. This is true even when off-nadir terrestrial targets are imaged. Rather than slewing the entire array to image an off-nadir target, targets located at a small angle off-nadir can be imaged by moving only the combiner spacecraft. However, optical delay lines are required to compensate for differential pathlength between collector pairs. As the combiner spacecraft is brought closer to the elliptical trajectory, less propellant but longer delay lines are required. In essence, the delay lines are used to offset the propellant required to image off-nadir targets. Hence, depending upon the complexity of the additional optics and the propellant required to slew the entire array, it may prove to be more beneficial to introduce delay lines into the interferometer.

5.2 Conclusion

The conclusions derived as a result of this study are listed in this section. From the determination of the optimal imaging configurations in Chapter 2, the following are concluded:

(i) Irrespective of whether the interferometer is operating in either the radio or visible spectrum, increasing the number of imaging locations increases the ability of the interferometer to mimic the ideal point spread function. However, the incremental increases in point response quality per incremental increase in the number of imaging locations (rate of return) diminishes as the number of locations increases.

(ii) The methodology developed in this study allows one to determine the optimal imaging locations that best mimic a weighted PSF map. This feature is not offered using other methodologies for placing the imaging locations.

(iii) When full instantaneous u-v coverage is desired, interferometers with collector spacecraft located at the Golay imaging locations offer the best fill factor performance. However, when the entire visible spectrum is considered, significant improvement in fill factor performance is observed when the collectors are located at the Cornwell imaging locations. This performance is comparable to that of the Golay configurations.

In Chapter 3, the imaging trajectories for a two collector and one combiner spacecraft were determined. Also studied in this chapter was the trade-off between improved image quality and propellant consumption as the number of collector spacecraft is increased. The following are the conclusions derived in Chapter 3:

(i) As more imaging locations are added, more resources are required for the spacecraft to complete their trajectories.

(ii) Interferometers that follow the optimized MSE imaging trajectories can provide images with better image quality while requiring fewer resources when compared with other candidate imaging configurations.

(iii) In cases where the propellant required to maneuver the spacecraft is large, lower system mass can be achieved by increasing the number of collector spacecraft. The optimal number of spacecraft corresponds to a balance between the total dry mass of the system and the propellant required to maneuver the spacecraft.

In Chapter 4, two orbit designs for a separated spacecraft Earth imager were presented. One design is an innovative concept involving the four conic sections. The following are concluded from Chapter 4:

(i) The dynamics of a spacecraft located in Earth's orbit can be sufficiently captured by considering a perfectly spherical Earth. Even when the largest perturbation is considered, the dynamics of a spacecraft located in LEO changes by only 0.1%.

(ii) There exists an orbit design where the interferometric requirements are met only the combiner spacecraft requires propellant and the collector spacecraft are in free orbits. The properties of the conic sections are fully exploited in this orbit design. This design gives the best propellant performance among the designs that were considered.

(iii) The propellant required for the interferometer to image an off-nadir target can be offset by introducing delay lines. In fact, there is no need to change any of the spacecraft trajectories, including the combiner spacecraft, to enable any terrestrial target to be imaged by an Earth imager in a geosynchronous orbit. All these can be done by just introducing delay lines into the interferometer.

Fundamentally, synthetic imaging using separated spacecraft interferometers involves a trade between the quality of the image and the amount of maneuvering resources (propellant and time) expended to achieve this quality. When the interferometer is placed within a planetary gravity-well, the natural motion between collector spacecraft, induced by gravitational tidal forces, can be exploited to dramatically reduce propellant consumption. Optimizing maneuver trajectories and exploiting orbital dynamics is essential to realizing the revolutionary improvements in imaging performance enabled by separated spacecraft interferometers.

5.3 Future Issues

This study only addresses a small fraction of design considerations for SSI. There exist a number of issues that warrant further investigation. The issues listed here are in fact a summary of the issues that were presented in the respective chapters.

(i) 'Observe on the Fly' Imaging Mode - In Chapter 3, the optimal trajectories for an interferometer operating in the 'Stop and Stare' mode were determined. There exists, however, the possibility of allowing these spacecraft to take interferometric measurements while they move relative to each other. This avenue should be explored in more depth as significant savings in resources have been shown to occur when the interferometer is allowed to observe on the fly.

(ii) Optimal Array Re-orientation - In Chapter 4, the propellant requirements for imaging nadir and off-nadir terrestrial targets was found. In these formulations, the propellant required to re-orient the array from imaging one target to another was not determined. These propellant requirements should be included in the total propellant requirement when different architectures are compared. These optimal trajectories can possibly be determined using principles of Optimal Control Theory. Not only minimum propellant trajectories should be determined, minimum time trajectories should also be determined for time critical cases.

(iii) Imaging of Inter-stellar Objects from Within Earth's Gravity-Well - The orbits designed in Chapter 4 are intended for an Earth imaging interferometer. It is possible to design orbits such that astronomical objects can be imaged while exploiting orbital dynamics. This option should definitely be explored as there are a number of advantages in placing such as system in Earth's orbit rather than outside its gravity-well.

(iv) Off-Nadir Imaging - One option that was presented for off-nadir imaging is to slew the entire array such that the spacecraft follow new trajectories. In most circumstances, this requires propellant. Since a free elliptical trajectory was found for a nadir looking array, there must exist other free elliptical trajectories that allow off-nadir targets to be imaged. In fact, an argument was presented in Chapter 4 as to why these free elliptical trajectories should exist and therefore warrant further investigation.

The number of imaging missions requiring the services of separated spacecraft is increasing more so than ever. Obtaining the optimum imaging architecture is therefore becoming critical. The issues discussed here will definitely play an important role in determining the best architecture for these missions.

REFERENCES

[Abell et al, 1987] Abell, G. O., Morrison, D., and Wolff, S. C., *Exploration of the Universe*, Saunders College Publishing, 1987.

[Abramowitz et al, 1972] Abramowitz, M., and Stegun, I. A., *Handbook of Mathematical Functions*, Dover Publication, Inc, New York, pg 609, 1972.

[AFRL, 1998] Air Force Research Laboratory, *Techsat21 Space Missions Using Satellite Clusters*, <URL:http://www.vs.afrl.af.mil/factsheets/techsat21.html> Accessed 24 September 1998.

[Blackwood et al, 1998] Blackwood, G. H., Dubovitsky, S., Linfield, R. P., and Gorham, P. W., *Interferometer instrument design for New Millennium Deep Space 3*, SPIE's International Symposium on Astronomical Telescopes and Instrumentations, Paper no. 3350-83, March 1998.

[Beichman et al, 1996] Beichman, C. A., ed., et. al., *A Road Map for the Exploration of Neighboring Planetary Systems (ExNPS)*, Final Report of the ExNPS Team, Jet Propulsion Laboratory Report No. JPL 96-22, NASA, Pasadena, CA, August 1996.

[Cassandra et al, 1994] Cassandra, A. R., Kaelbling, L. P., and Littman, M. L., *Acting Optimally in Partially Observable Stochastic Domains*, Proceedings of the National Conference on Artificial Intelligence Proceedings of the 12th National Conference on Artifical Intelligence, Vol. 2, Jul 31-Aug 4 1994.

[Cornwell, 1988] Cornwell, T. J., *A Novel Principle for Optimization of the Instantaneous Fourier Plane Coverage of Correlation Arrays*, IEEE Transactions on Antennas and Propagation, Vol. 36, No. 8, August 1988.

[Feynman et al, 1989] Feynman, R. P., Leighton, R. B., and Sands, M. L., *The Feynman Lectures on Physics: Commemorative Issue*, Addison-Wesley Publishing Company, 1989.

[Gallagher et al, 1998] Gallagher, D., Lau, K. H., Blackwood, G. H., Leschly, K., Shao, M., *New Millennium deep space 3 mission: separated spacecraft optical interferometer*, SPIE's International Symposium on Astronomical Telescopes and Instrumentations, Paper no. 3350-09, March 1998.

[Golay, 1971] Golay, M., *Point Arrays Having Compact Non-Redundant Autocorrelations*, Journal of Optical Society America, Vol 61, pg 272, 1971.

[Gorham, 1998] Gorham, P., 22 June 1998, Personal Communication.

[Hecht, 1987] Hecht, E., *Optics*, Addison-Wesley Publishing Company, 2nd edition, 1987.

[Hill, 1978] Hill, G. W., *Researches in the Lunar Theory*, American Journal of Mathematics, vol. 1, No. 1, pp. 5-26, 1978.

[Jilla, 1998] Jilla, C. D., *Separated Spacecraft Interferometry - System Architecture Design and Optimization*, Masters Thesis, Department of Aeronautics and Astronautics, Massachusetts Institute of Technology, 1998.

[JPL, 1998] Jet Propulsion Laboratory, *Planet Imager*, <URL:http://origins.jpl.nasa.gov/missions/planetimg.html>. Accessed 18 October 1998.

[JPL, 1998] Jet Propulsion Laboratory, *Space Interferometry Mission*, <URL:http://huey.jpl.nasa.gov/sim/>. Accessed 22 September 1998.

[Isakowitz, 1991] Isakowitz, S. J., *International Reference Guide to Launch Systems*, American Institute of Aeronautics and Astronautics Publication, Washington DC, 1991.

[Kirk, 1970] Kirk, D. E., *Optimal Control Theory - An Introduction*, Prentice-Hall Networks Inc., New Jersey, 1970.

[Kirkpatrick et al, 1983] Kirkpatrick, S., Gelatt, C.D. Jr., Vecchi, M.P., *Optimization by Simulated Annealing*, Science, Vol. 220, No. 4598, 13 May 1983.

[Kong et al, 1998] Kong, E. M., and Miller, D. W., *Optimization of Separated Spacecraft Interferometer Trajectories in the Absence of A Gravity-Well*, SPIE's International Symposium on Astronomical Telescopes and Instrumentations, Paper no. 3350-13, March 1998.

[Kreyszig,1988] Kreyszig, E., *Advanced Engineering Mathematics*, John Wiley & Sons, 6th edition, 1988.

[Larson et al, 1992] Larson, W. J., and Wertz, J. R., *Space Mission Analysis and Design*, Microcosm, Inc and Kluwer Academic Publishers, 2nd edition, 1992.

[Lin, 1965] Lin, S., *Computer Solutions of the Traveling Salesman Problem*, Journal of Bell System Technology, Vol. 44, pg. 2245, 1965.

[Linfield, 1997] Linfield, R., *Number of Sources DS3 can Observe, as a Function of Spacecraft Power*, Jet Propulsion Laboratory Inter-office Memorandum 335.1-97-0.14, 16th May 1997.

[Loiseau et al, 1996] Loiseau, S, and Shaklan, S., *Optical design, modelling and tolerancing of a Fizeau interferometer dedicated to astrometry*, Astronomy and Astrophysics Supplement Series No. 177, pg. 167-178, May 1996.

[Mallory et al, 1998] Mallory, G. J., Jilla, C. D., Miller, D. W., *Optimization of Geosynchronous Satellite Constellations for Interferometric Earth Imaging*, AIAA/AAS Astrodynamics Specialists Conference, August 1998.

[Miller et al, 1998] Miller, D. W., Shaw, G. B., Kong, E. M., *Systems Level Analysis of Proposed JPL's Earth Imager Program*, Power Point Presentations for JPL's 6-week Study, June 1998.

[Naderi, 1998] Naderi, F. M., *NASA Origins and Fundamental Physics Program*, SPIE's Interna-

tional Symposium on Astronomical Telescopes and Instrumentations, Paper no. 3350-125, March 1998.

[Powers et al, 1997] Powers, M., Leitner, J., Hackney, E., Bell, K. D., Boucher, R., Roberston, L., Schrader, K., *Assessment of a large aperture telescope trade space and active opto-mechanical control architecture*, IEEE Aerospace Applications Conference Proceedings, Proceedings of the 1997 IEEE Aerospace Conference, p 197-229, Feb 1-2, 1997.

[Sedwick et al, 1998] Sedwick, R. J., Kong, E. M. C., Miller, D. W., *Exploiting Orbital Dynamics and Micropropulsion for Aperture Synthesis Using Distributed Satellite Systems: Applications to Techsat21*, AIAA Defense & Civil Space Programs Conference, AIAA-98-5289, October 1998.

[Shaw, 1998] Shaw, G. B., *The Generalized Information Network Analysis Methodology for Distributed Satellite Systems*, PhD Thesis, Department of Aeronautics and Astronautics, Massachusetts Institute of Technology, 1998.

[Staelin et al, 1994] Staelin, David H., Morgenthaler, Ann W., Kong, Jin Au, *Electromagnetic Waves*, Prentice Hall, 1994.

[STScI, 1998] Space Telescope Science Institute, *General Overview of the Hubble Space Telescope*, <URL:http://www.stsci.edu/hst/>. Accessed 22 September 1998.

[Stephenson et al, 1998] Stephenson, J. L., Jr., Miller, D. W., and Crawley, E. F., *Comparative System Trades Between Structurally Connected and Separated Spacecraft Interferometers for the Terrestrial Planet Finder Mission*, MIT Space Engineering Reseach Center Report #3-98, May 1998.

[Stockman ed., 1997] Stockman, H. S., ed., *The Next Generation Space Telescope: Visiting a Time When Galaxies Were Young*, June 1998.

[Surka et al, 1996] Surka, D. M., and Crawley, E. F., *A Comparison of Structurally Connected and Multiple Spacecraft Interferometers*, SERC Report #9-96, MIT Space Systems Laboratory, 1996.

[Thomas et al, 1988] Thomas G. B. Jr., Finney, R. L., *Calculus and Analytic Geometry*, Addison-Wesley Publishing Company, 7th edition, 1988.

[Thompson et al, 1986] Thompson, A. R., Moran, J. M., Swenson, G. W. Jr., *Interferometry and synthesis in radio astronomy*, 1986.

[Yashko, 1998] Yashko, G., *Ion Micro-Propulsion and Cost Modelling for Satellite Clusters*, MIT Space Engineering Research Center Report #9-98, June 1998.

[Yu et al, 1998] Yu, J. W., Marr, J., Stoller, R. L., Kahn, P., *SIM interferometer design*, SPIE's International Symposium on Astronomical Telescopes and Instrumentations, Paper no. 3350-05, March 1998.

Appendix A

POINT SPREAD FUNCTIONS

The imaging locations and their corresponding Point Spread Functions (PSFs) generated for the different imaging configurations in Chapter 2 are shown in this appendix. The following is a list of the figures contained in this appendix.

Nominal PSFs (101x101 Pixels) 158
Cornwell PSFs 160
Square Parition (75x75 Pixels) 161
Square Partition (51x51 Pixels) 163
Rectangular Partition (101x51 Pixels) 165
Two Collector Interferometer (75x75 Pixels) 167
Golay PSF - Two Collector Intefermeter. 169
Cornwell PSF - Two collector Interferometer 170

Nominal PSFs (101x101 Pixels)

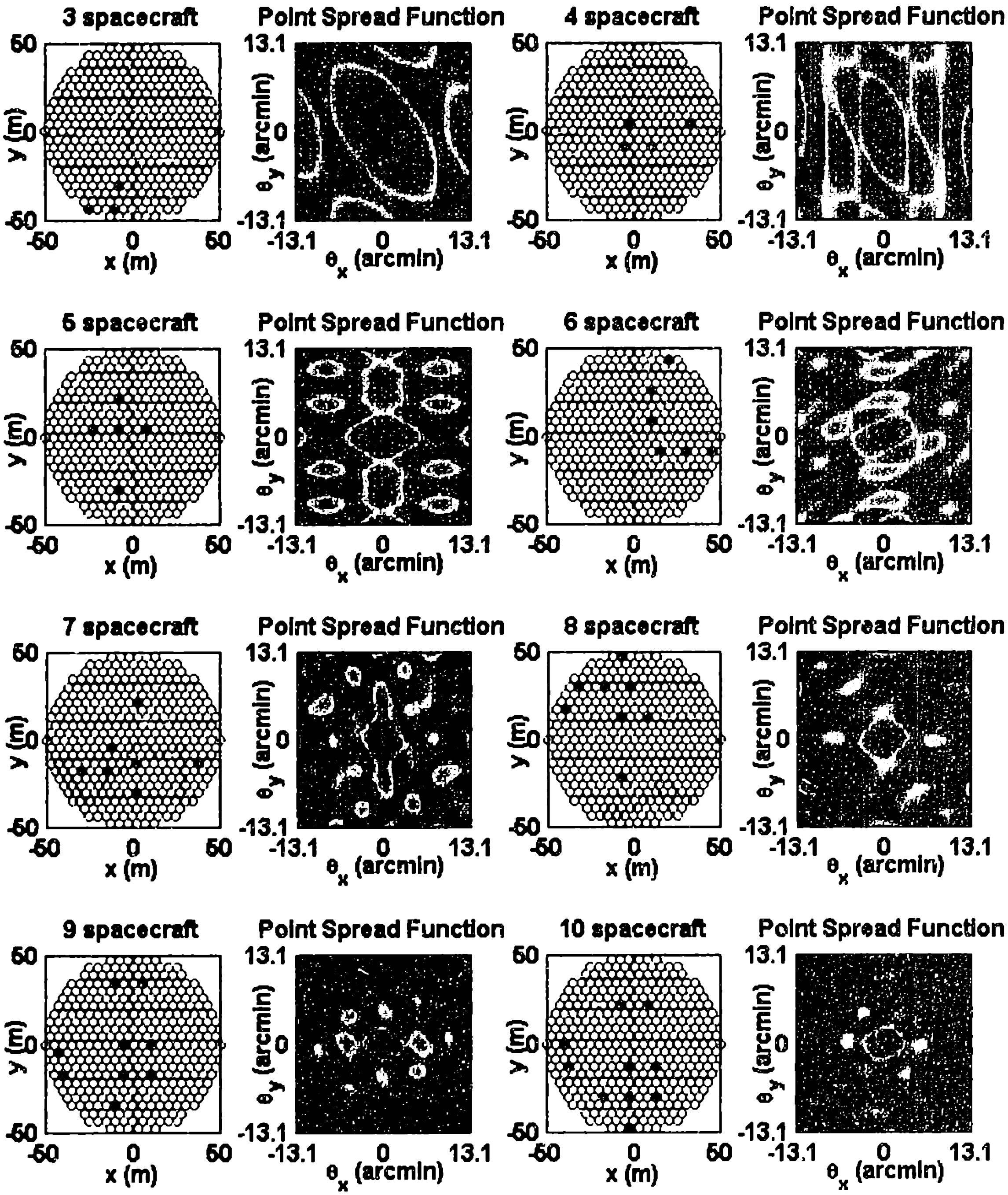

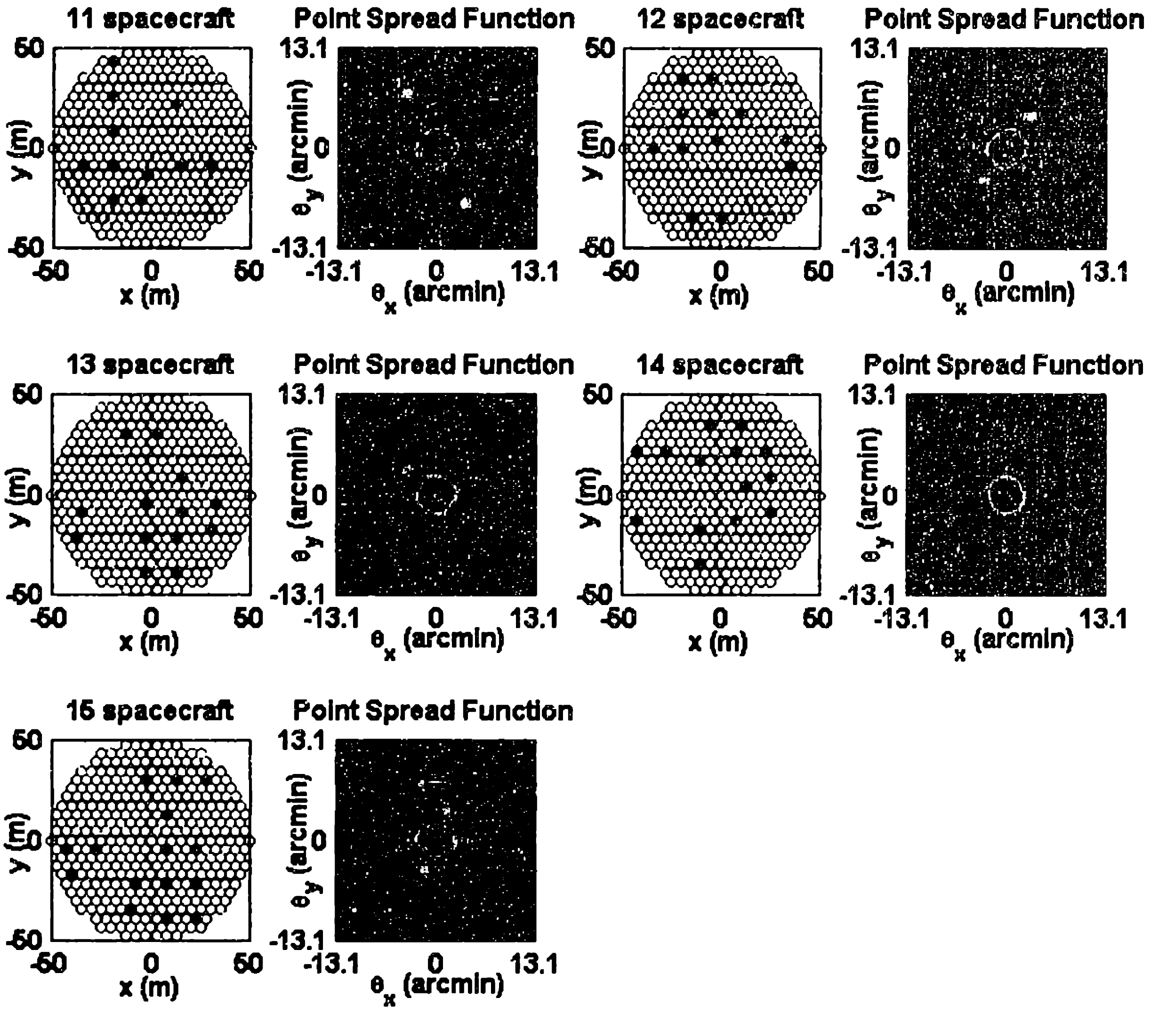
11 spacecraft
Point Spread Function
12 spacecraft
Point Spread Function
13 spacecraft
Point Spread Function
14 spacecraft
Point Spread Function
15 spacecraft
Point Spread Function
y (m)
x (m)
50
0
-50
θ_y (arcmin)
θ_x (arcmin)
13.1
0
-13.1

Cornwell PSFs

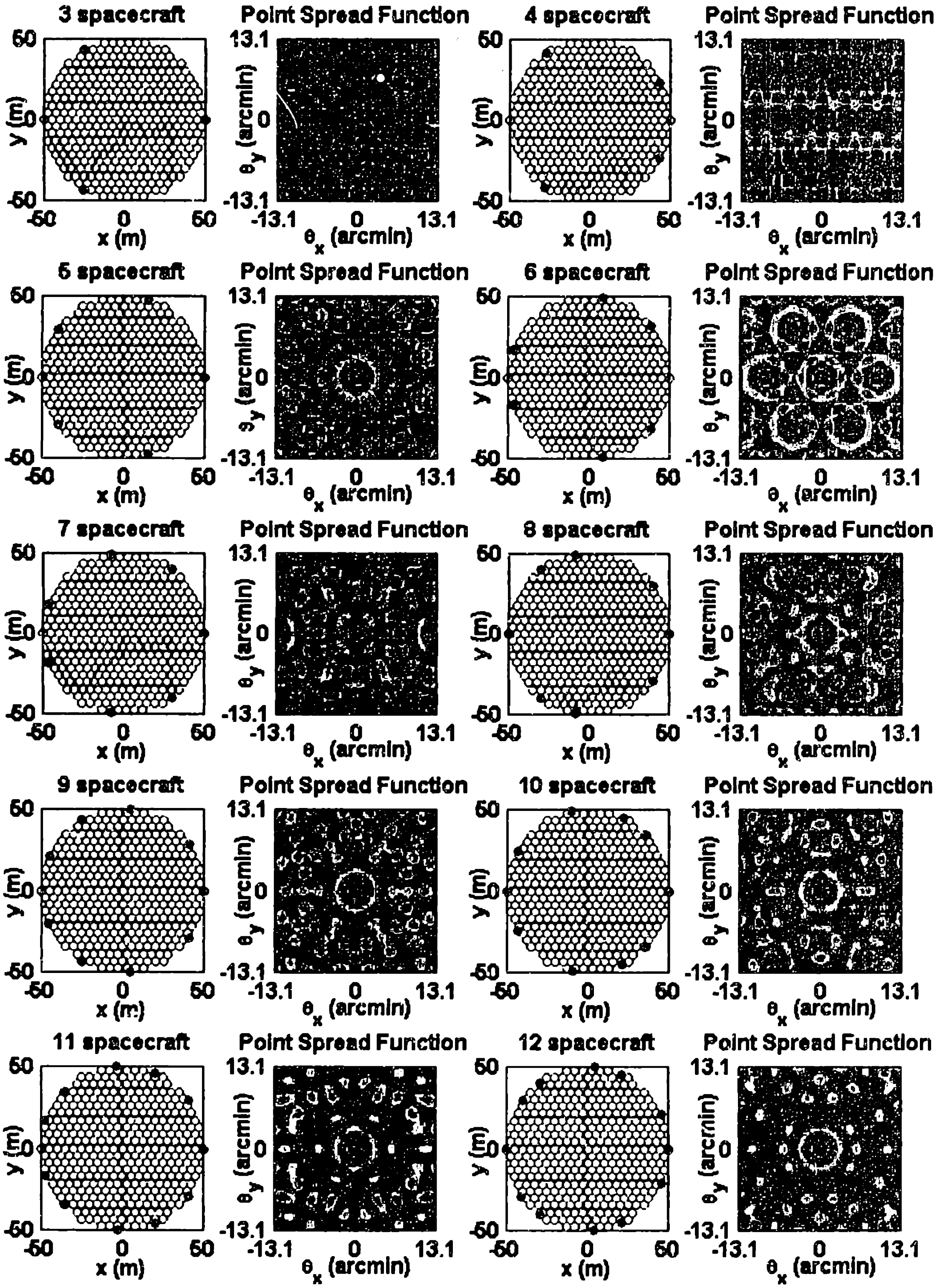

Square Parition (75x75 Pixels)

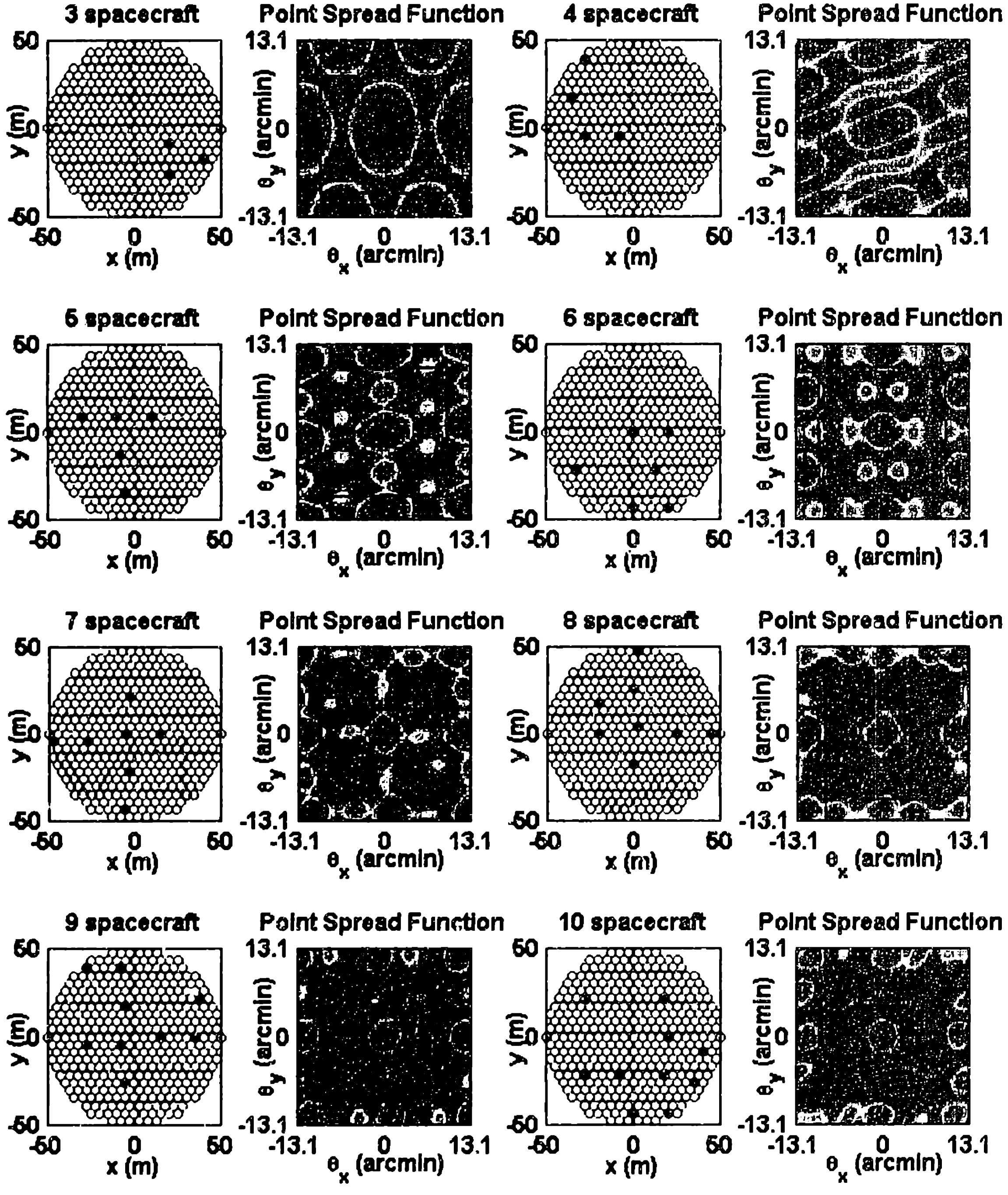

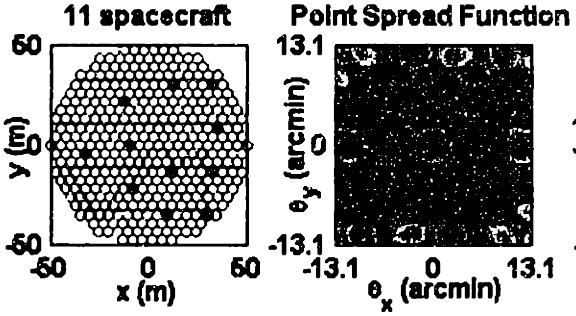
11 spacecraft
50
0
-50
y (m)
-50
0
50
x (m)
Point Spread Function
13.1
0
-13.1
θy (arcmin)
-13.1
0
13.1
θx (arcmin)

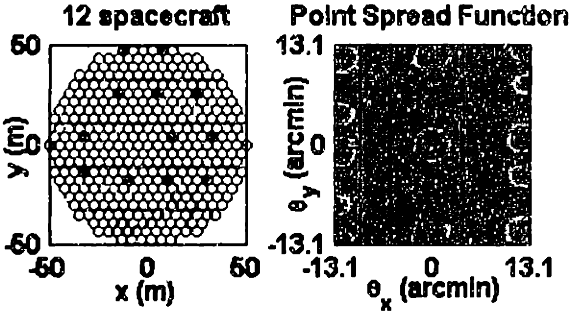
12 spacecraft
50
0
-50
y (m)
-50
0
50
x (m)
Point Spread Function
13.1
0
-13.1
θy (arcmin)
-13.1
0
13.1
θx (arcmin)

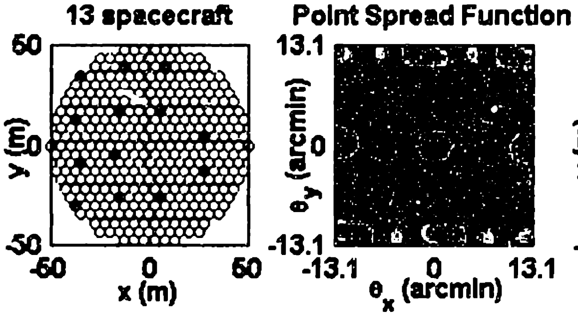
13 spacecraft
50
0
-50
y (m)
-50
0
50
x (m)
Point Spread Function
13.1
0
-13.1
θy (arcmin)
-13.1
0
13.1
θx (arcmin)

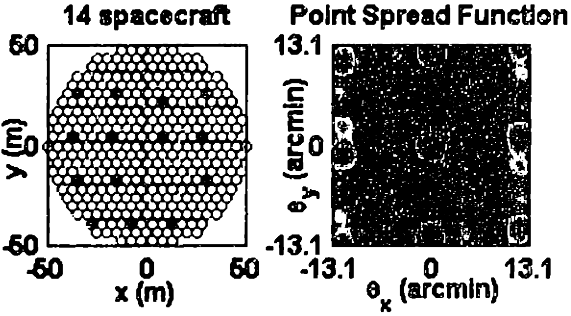
14 spacecraft
50
0
-50
y (m)
-50
0
50
x (m)
Point Spread Function
13.1
0
-13.1
θy (arcmin)
-13.1
0
13.1
θx (arcmin)

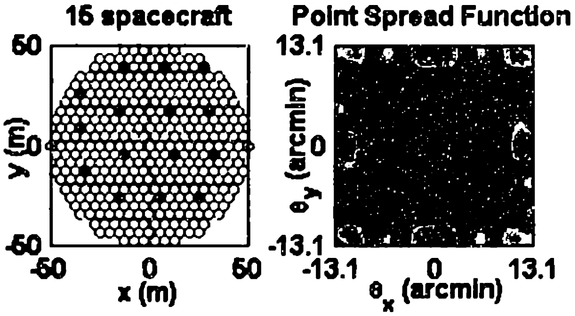
15 spacecraft
50
0
-50
y (m)
-50
0
50
x (m)
Point Spread Function
13.1
0
-13.1
θy (arcmin)
-13.1
0
13.1
θx (arcmin)

Square Partition (51x51 Pixels)

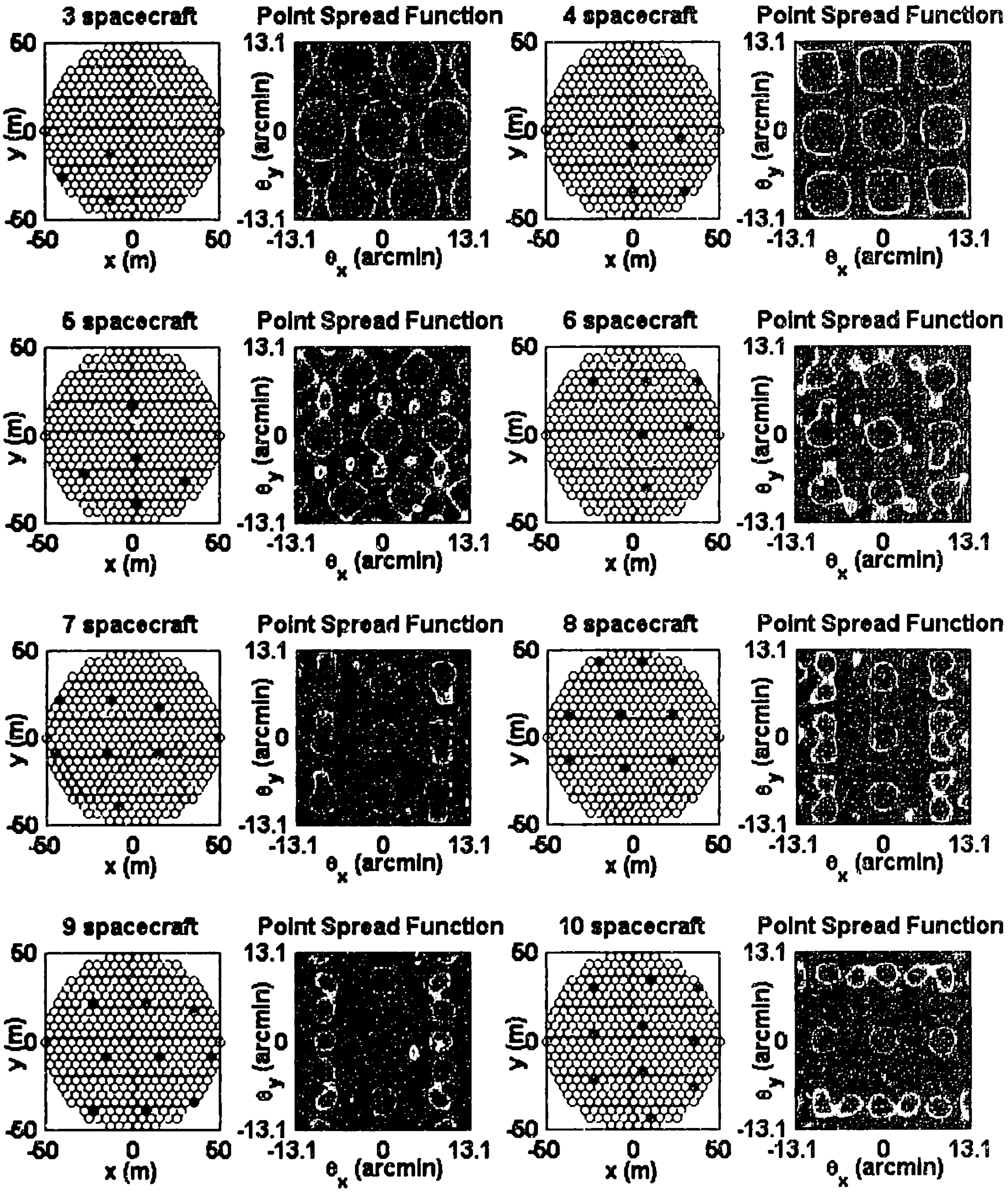

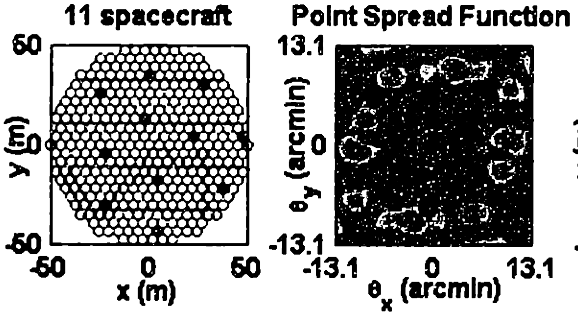
11 spacecraft
Point Spread Function
50
y (m)
0
-50
-50
0
50
x (m)
13.1
θ_y (arcmin)
0
-13.1
-13.1
0
13.1
θ_x (arcmin)

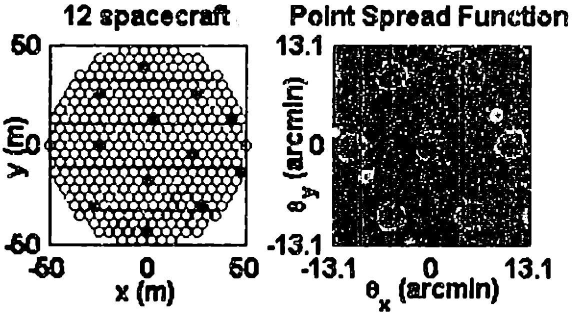
12 spacecraft
Point Spread Function
50
y (m)
0
-50
-50
0
50
x (m)
13.1
θ_y (arcmin)
0
-13.1
-13.1
0
13.1
θ_x (arcmin)

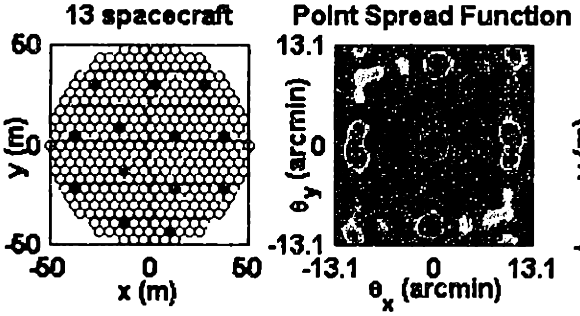
13 spacecraft
Point Spread Function
50
y (m)
0
-50
-50
0
50
x (m)
13.1
θ_y (arcmin)
0
-13.1
-13.1
0
13.1
θ_x (arcmin)

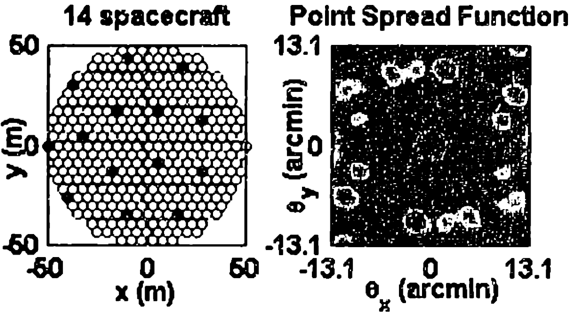
14 spacecraft
Point Spread Function
50
y (m)
0
-50
-50
0
50
x (m)
13.1
θ_y (arcmin)
0
-13.1
-13.1
0
13.1
θ_x (arcmin)

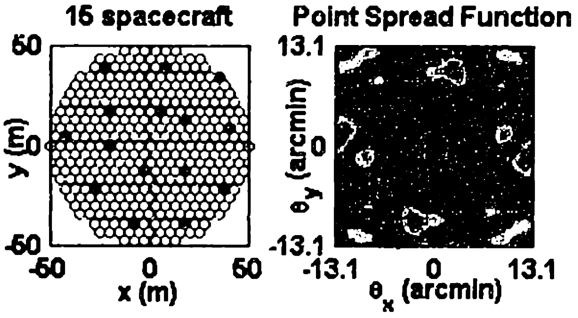
15 spacecraft
Point Spread Function
50
y (m)
0
-50
-50
0
50
x (m)
13.1
θ_y (arcmin)
0
-13.1
-13.1
0
13.1
θ_x (arcmin)

Rectangular Partition (101x51 Pixels)

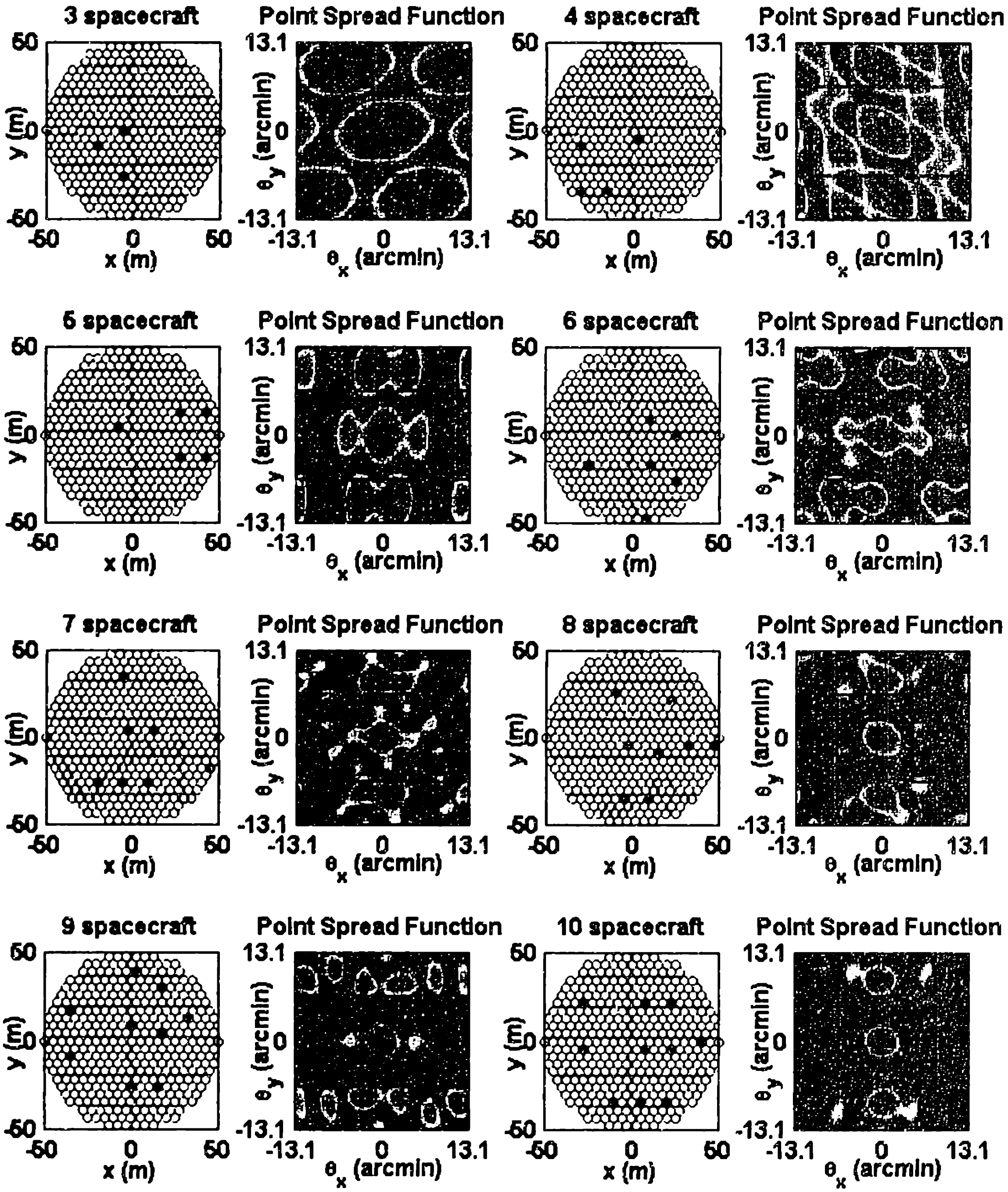

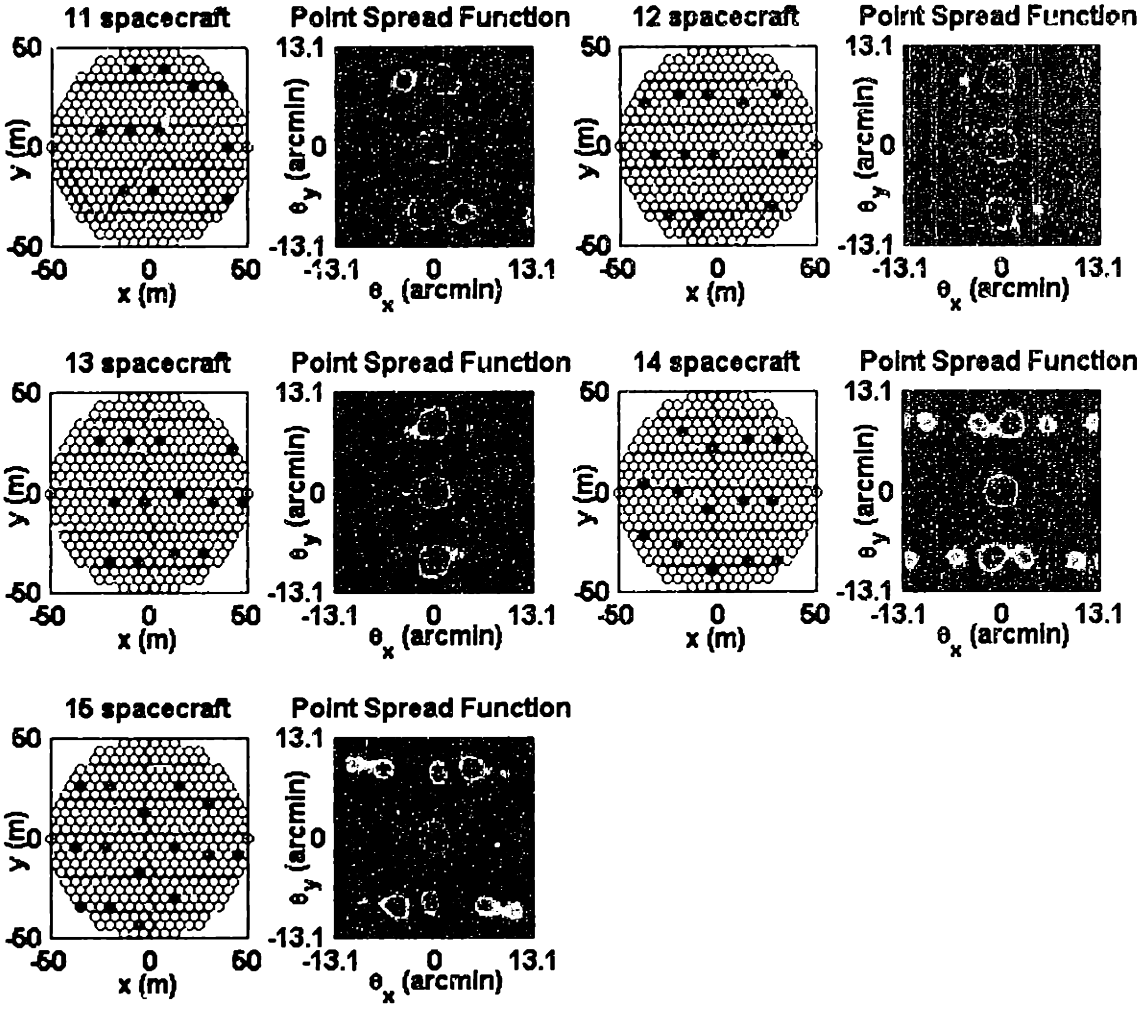
11 spacecraft
Point Spread Function
12 spacecraft
Point Spread Function
13 spacecraft
Point Spread Function
14 spacecraft
Point Spread Function
15 spacecraft
Point Spread Function
50
0
-50
y (m)
x (m)
13.1
-13.1
θ_y (arcmin)
θ_x (arcmin)

Two Collector Interferometer (75x75 Pixels)

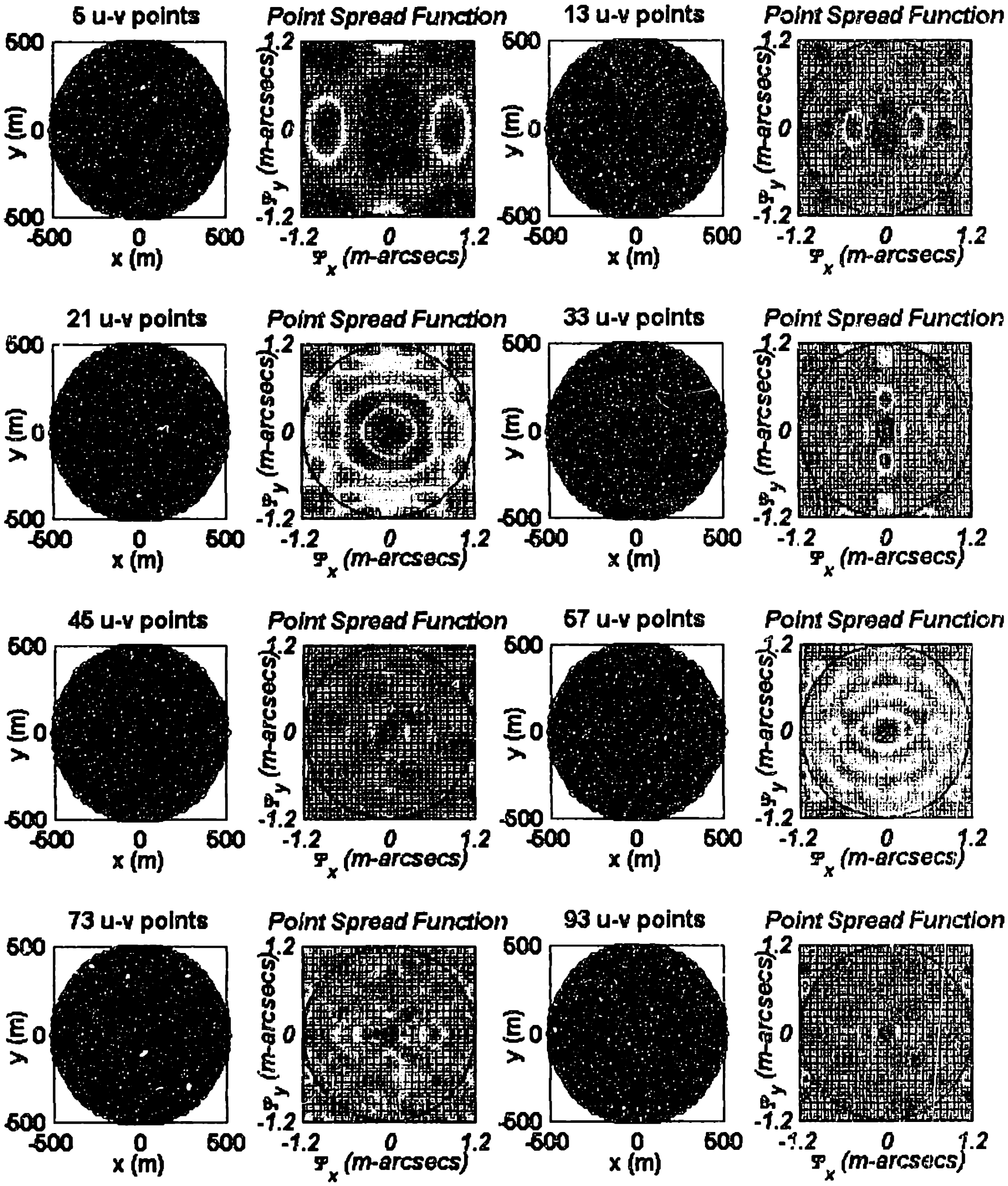

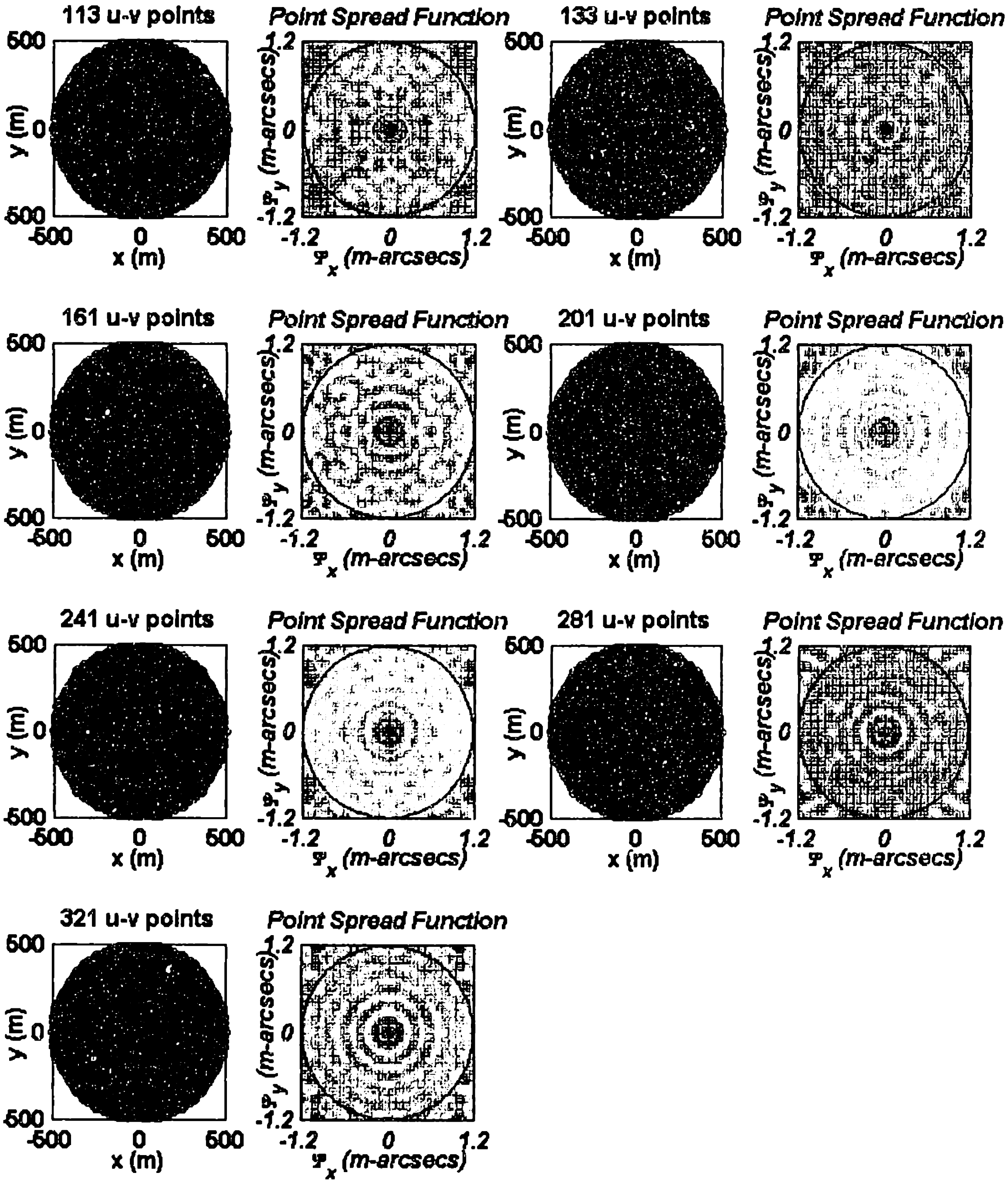
113 u-v points
Point Spread Function
133 u-v points
Point Spread Function
161 u-v points
Point Spread Function
201 u-v points
Point Spread Function
241 u-v points
Point Spread Function
281 u-v points
Point Spread Function
321 u-v points
Point Spread Function
y (m)
x (m)
500
0
-500
Ψ_y (m-arcsecs)
Ψ_x (m-arcsecs)
1.2
0
-1.2

Golay PSF - Two Collector Intefermeter

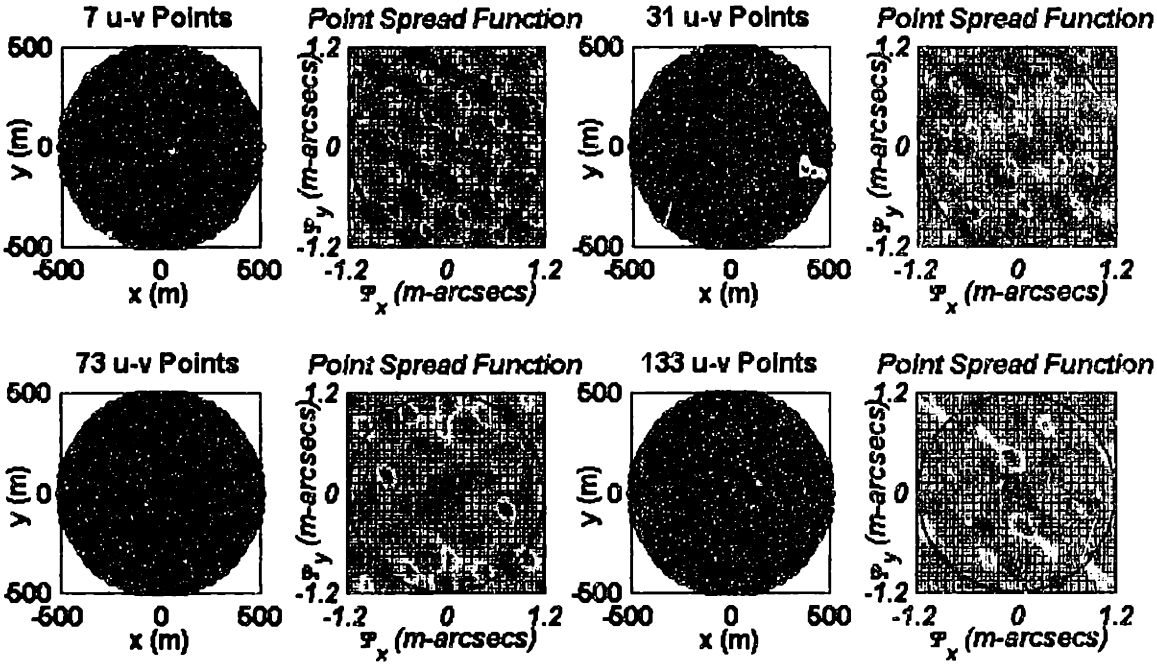

Cornwell PSF - Two collector Interferometer

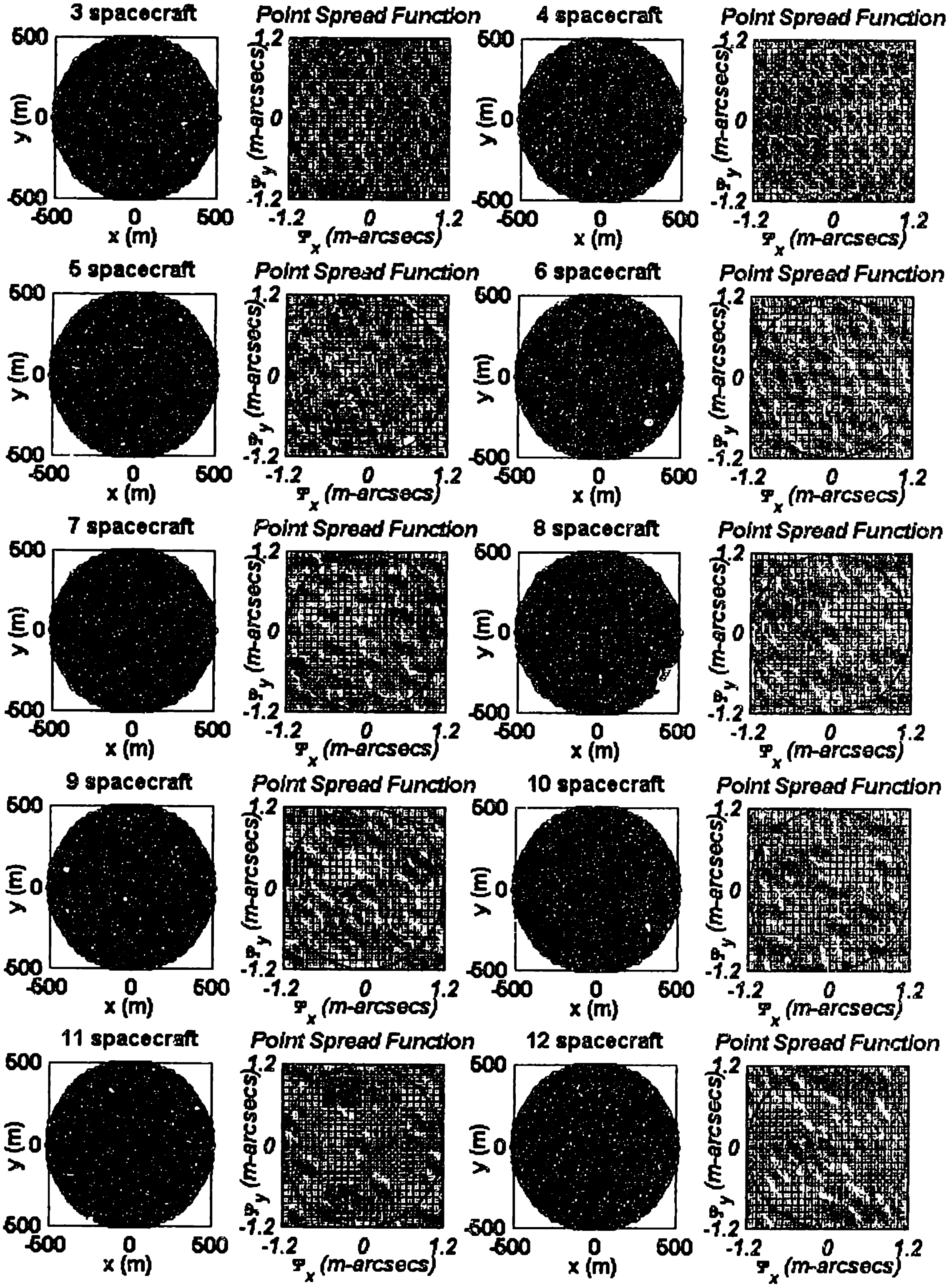

Appendix B

OPTIMAL IMAGING TRAJECTORIES

The optimal imaging trajectories for the different imaging configurations obtained in Chapter 3 are shown in this appendix. The following is a list of the optimal imaging trajectories presented here:

Equivalent Cornwell Imaging Locations - Optimal Propellant Trajectories 172
Equivalent Cornwell Imaging Locations - Optimal Time Trajectories 173

Equivalent Cornwell Imaging Locations - Optimal Propellant Trajectories

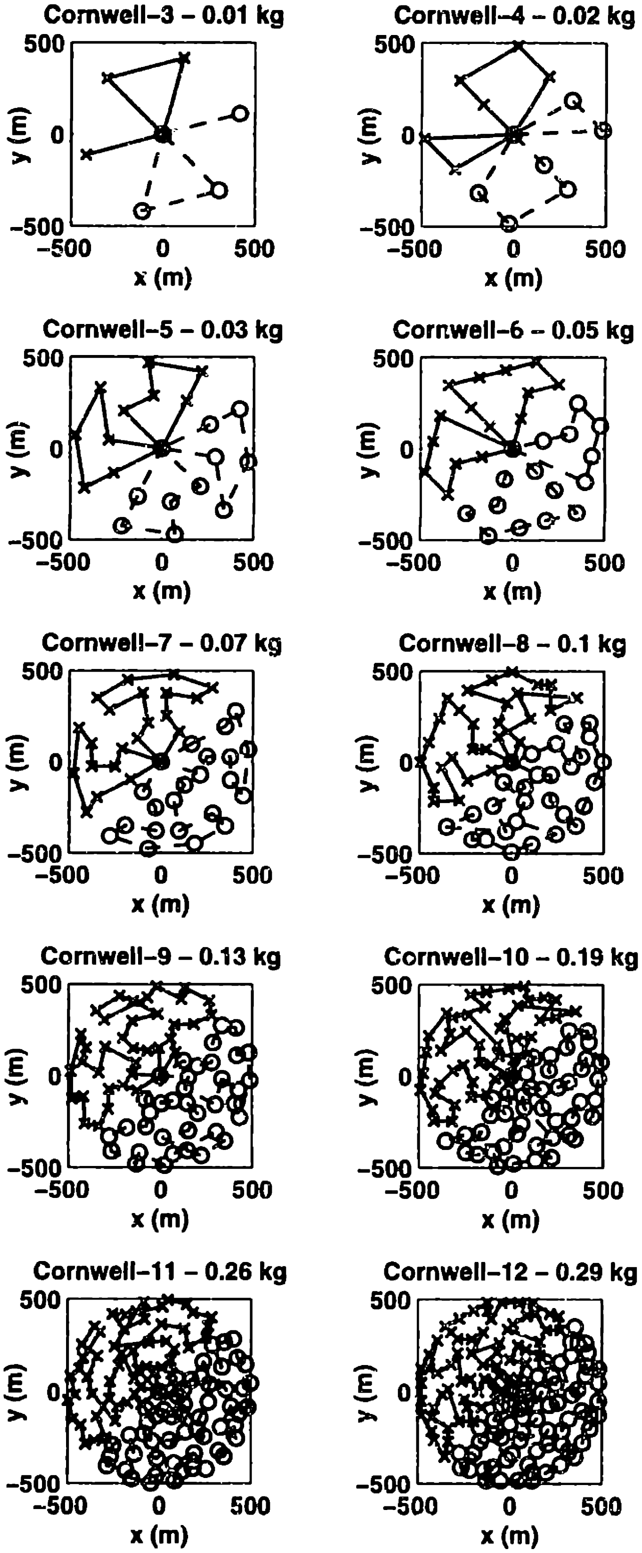

Equivalent Cornwell Imaging Locations - Optimal Time Trajectories

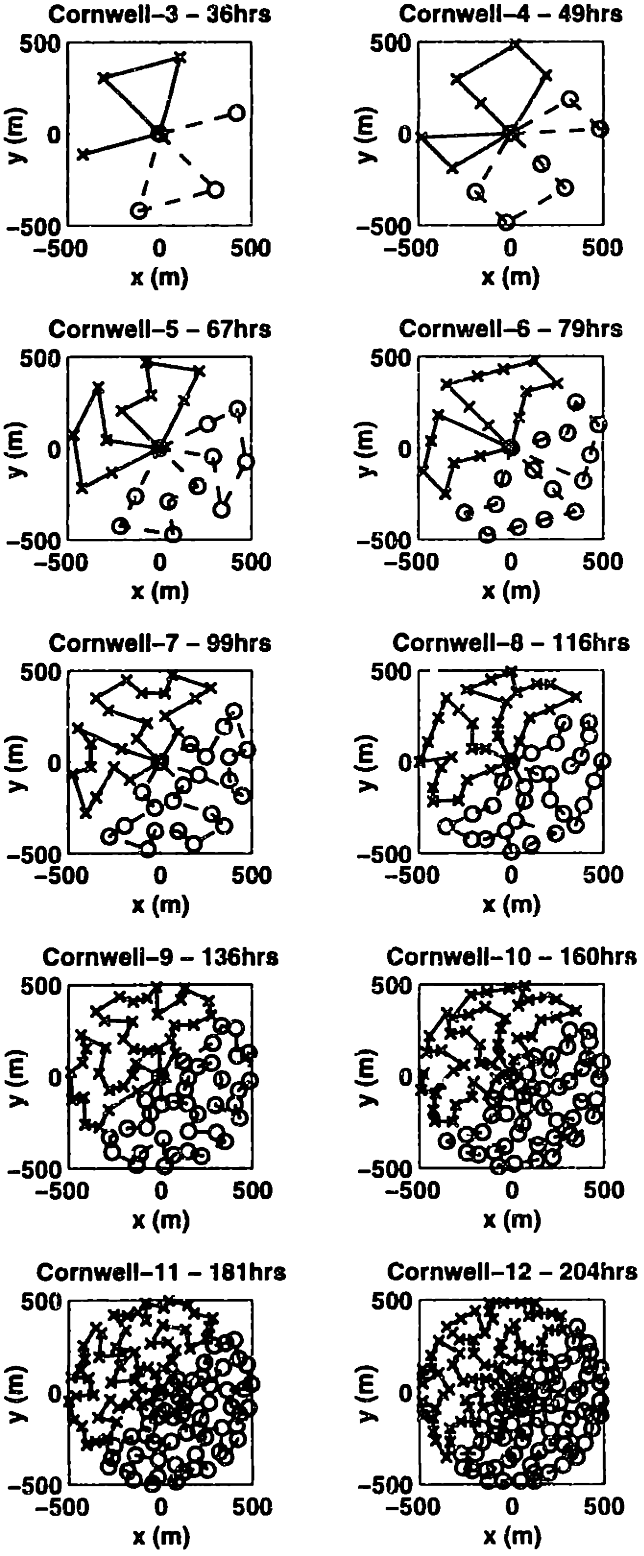

Optimized MSE Locations - Optimal Mass Trajectories

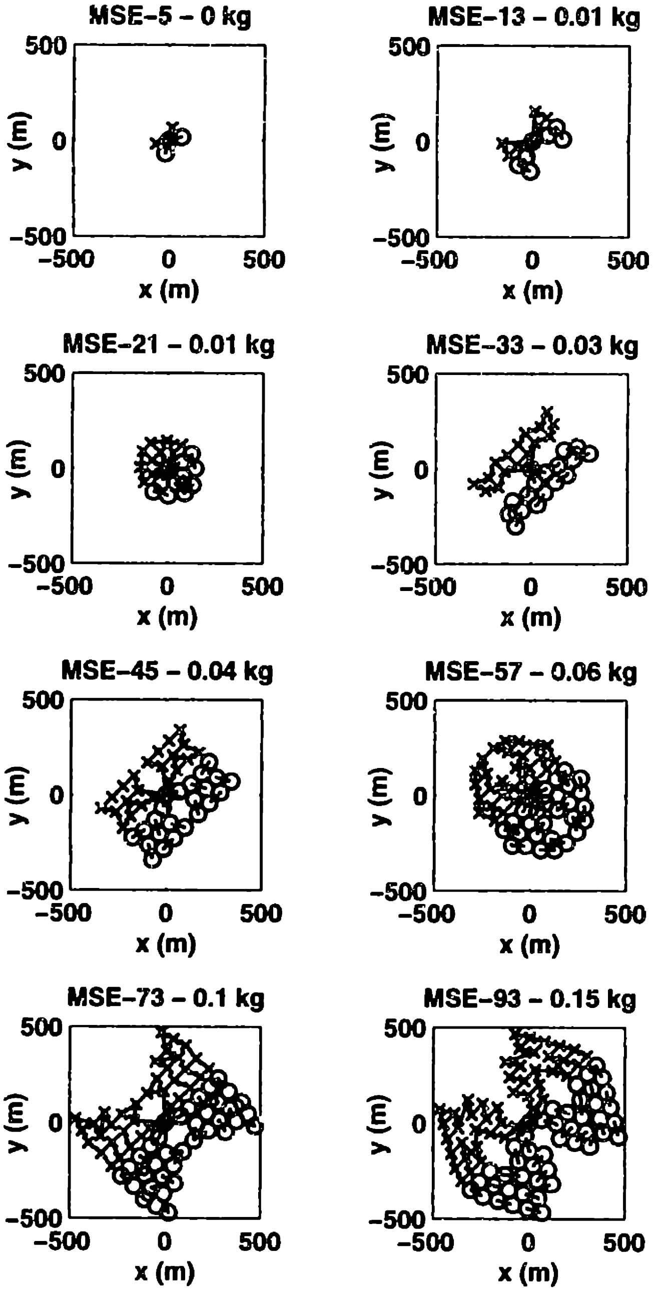

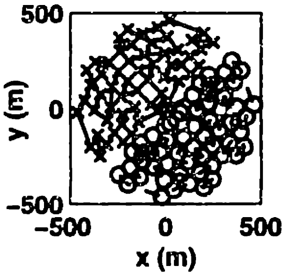

MSE-113 - 0.22 kg

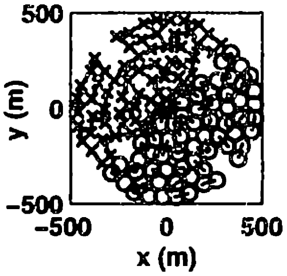

MSE-133 - 0.28 kg

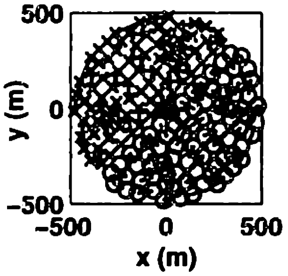

MSE-161 - 0.39 kg

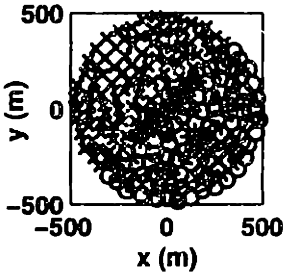

MSE-201 - 0.54 kg

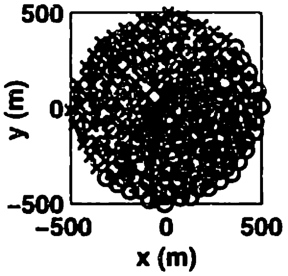

MSE-241 - 0.73 kg

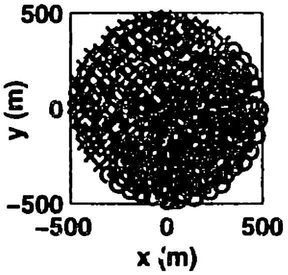

MSE-281 - 0.9 kg

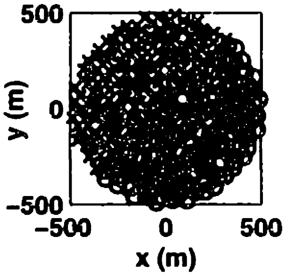

MSE-321 - 1.15 kg

Optimized MSE Locations - Optimal Time Trajectories

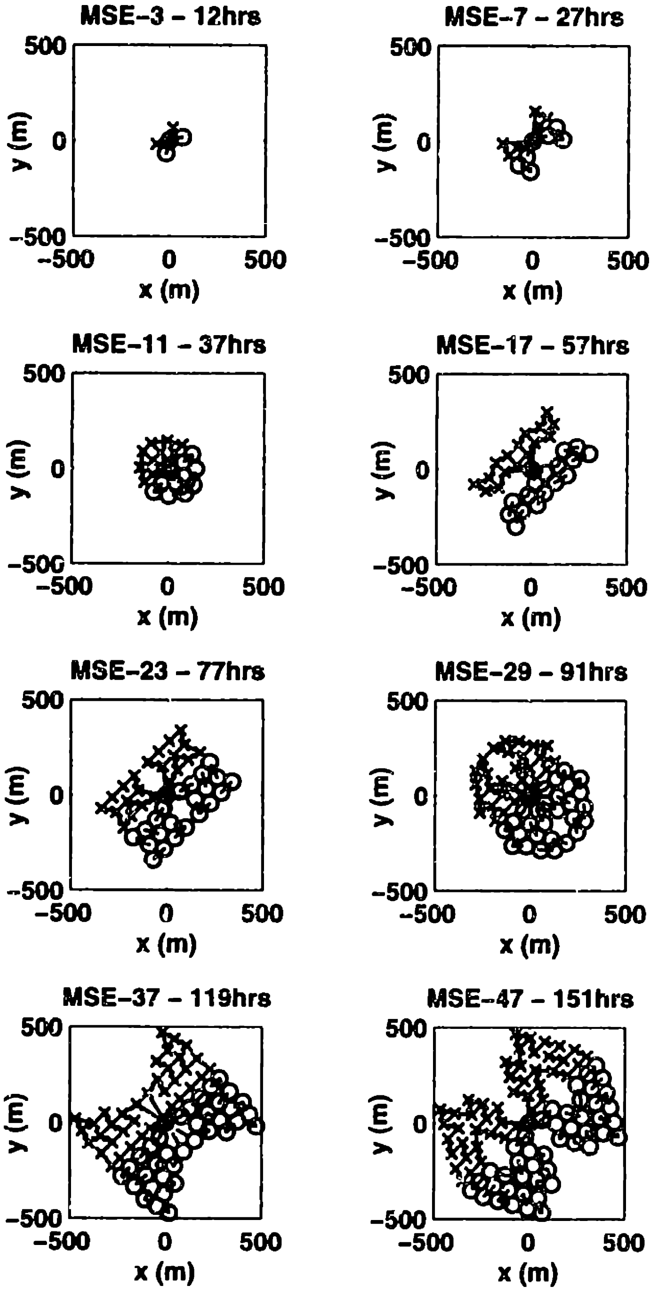

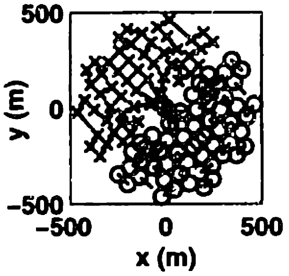
MSE-113 - 178hrs

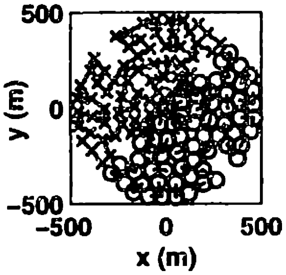
MSE-133 - 207hrs

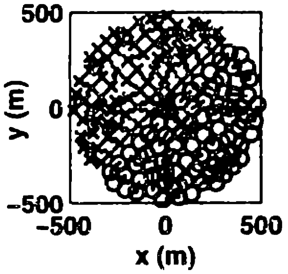
MSE-161 - 238hrs

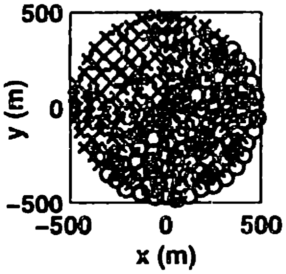
MSE-201 - 283hrs

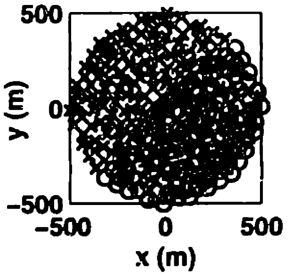
MSE-241 - 320hrs

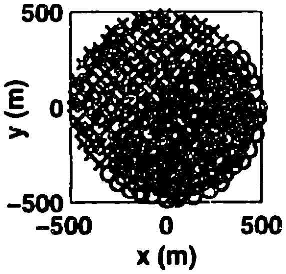
MSE-281 - 351hrs

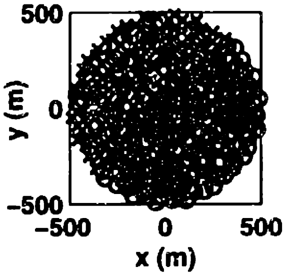
MSE-321 - 384hrs